

**AFRL-RV-PS-
TR-2013-0160**

**AFRL-RV-PS-
TR-2013-0160**

SPACECRAFT CHARGING MODELING – NASCAP-2K 2013 Annual Report

V. A. Davis and M. J. Mandell

**Leidos
10260 Campus Point Drive, Mailstop C4
San Diego, CA 92121**

20 September 2013

Technical Report

APPROVED FOR PUBLIC RELEASE; DISTRIBUTION IS UNLIMITED.



**AIR FORCE RESEARCH LABORATORY
Space Vehicles Directorate
3550 Aberdeen Ave SE
AIR FORCE MATERIEL COMMAND
KIRTLAND AIR FORCE BASE, NM 87117-5776**

DTIC COPY

NOTICE AND SIGNATURE PAGE

Using Government drawings, specifications, or other data included in this document for any purpose other than Government procurement does not in any way obligate the U.S. Government. The fact that the Government formulated or supplied the drawings, specifications, or other data does not license the holder or any other person or corporation; or convey any rights or permission to manufacture, use, or sell any patented invention that may relate to them.

This report was cleared for public release by the 377 ABW Public Affairs Office and is available to the general public, including foreign nationals. Copies may be obtained from the Defense Technical Information Center (DTIC) (<http://www.dtic.mil>).

AFRL-RV-PS-TR-2013-0160 HAS BEEN REVIEWED AND IS APPROVED FOR
PUBLICATION IN ACCORDANCE WITH ASSIGNED DISTRIBUTION STATEMENT.

//SIGNED//

//SIGNED//

Adrian Wheelock
Program Manager/ AFRL/RVBXR

Edward J. Masterson, Colonel, USAF
Chief, Battlespace Environment Division

This report is published in the interest of scientific and technical information exchange, and its publication does not constitute the Government's approval or disapproval of its ideas or findings.

REPORT DOCUMENTATION PAGE

*Form Approved
OMB No. 0704-0188*

Public reporting burden for this collection of information is estimated to average 1 hour per response, including the time for reviewing instructions, searching existing data sources, gathering and maintaining the data needed, and completing and reviewing this collection of information. Send comments regarding this burden estimate or any other aspect of this collection of information, including suggestions for reducing this burden to Department of Defense, Washington Headquarters Services, Directorate for Information Operations and Reports (0704-0188), 1215 Jefferson Davis Highway, Suite 1204, Arlington, VA 22202-4302. Respondents should be aware that notwithstanding any other provision of law, no person shall be subject to any penalty for failing to comply with a collection of information if it does not display a currently valid OMB control number. **PLEASE DO NOT RETURN YOUR FORM TO THE ABOVE ADDRESS.**

1. REPORT DATE (DD-MM-YYYY) 20-09-2013	2. REPORT TYPE Annual Report	3. DATES COVERED (From - To) 22 Sep 2012 to 20 Sep 2013 4. TITLE AND SUBTITLE SPACECRAFT CHARGING MODELING – NASCAP-2k 2013 Annual Report 6. AUTHOR(S) V. A. Davis and M. J. Mandell 7. PERFORMING ORGANIZATION NAME(S) AND ADDRESS(ES) Leidos 10260 Campus Point Drive, Mailstop C4 San Diego, CA 92121 9. SPONSORING / MONITORING AGENCY NAME(S) AND ADDRESS(ES) Air Force Research Laboratory Space Vehicles Directorate 3550 Aberdeen Avenue SE Kirtland AFB, NM 87117-5776		
			5a. CONTRACT NUMBER FA9453-11-C-0262	5b. GRANT NUMBER 5c. PROGRAM ELEMENT NUMBER 62601F
			5d. PROJECT NUMBER 1010	5e. TASK NUMBER PPM00012836
			5f. WORK UNIT NUMBER EF003277	8. PERFORMING ORGANIZATION REPORT NUMBER
			10. SPONSOR/MONITOR'S ACRONYM(S) AFRL/RVBXR 11. SPONSOR/MONITOR'S REPORT NUMBER(S) AFRL-RV-PS-TR-2013-0160	
12. DISTRIBUTION / AVAILABILITY STATEMENT Approved for public release; distribution is unlimited. (377ABW-2013-1049 dtd 12 Dec 2013)				
13. SUPPLEMENTARY NOTES				
14. ABSTRACT In support of the larger goal to provide a plasma engineering capability to the spacecraft community, the objective of the Spacecraft Charging Modeling—Nascap-2k contract is to develop, incorporate, test, and validate new algorithms for the three-dimensional plasma-environment spacecraft interactions computational tool, Nascap-2k. Nascap-2k is being modified to extend the range of plasma physics phenomena that the code can simulate, make the advanced code capabilities more accessible to users, and improve and maintain both the graphical and non-graphical interfaces to the code. The upgraded code is being used to simulate problems of interest to AFRL. During the second year, Nascap-2k 4.1 was modified to automatically create macroparticles at surfaces and optionally use them to computer currents to surfaces using the reverse trajectory technique. Tools were developed to write a script for a rotating spacecraft and to read a COLISEUM plume file. The upgraded code was used to support the DSX (Demonstration and Science eXperiments) and AEHF-2 (Advanced Extremely High Frequency) spacecraft programs and the AFRL project to develop a differential charging index.				
15. SUBJECT TERMS Nascap-2k, Potentials, Space Environment, Spacecraft, Spacecraft Charging, DSX				
16. SECURITY CLASSIFICATION OF:			17. LIMITATION OF ABSTRACT Unlimited	18. NUMBER OF PAGES 82
a. REPORT Unclassified	b. ABSTRACT Unclassified	c. THIS PAGE Unclassified	19a. NAME OF RESPONSIBLE PERSON Adrian T. Wheelock	
			19b. TELEPHONE NUMBER (include area code)	

This page is intentionally left blank.

Table of Contents

	Page
List of Figures	iii
List of Tables.....	viii
1. Introduction.....	1
1.1. Second Year Progress.....	1
1.1.1. Interoperability of <i>Nascap-2k</i> with Other Codes	1
1.1.2. Enhanced Plasma Simulation.....	2
1.1.3. Maintenance and Support	2
1.1.4. Apply <i>Nascap-2k</i> to DSX	3
1.1.5. Advanced EHF Analysis	4
1.1.6. Charging Index.....	4
1.2. Reports and Meetings	5
1.3. Scientific Reports and Journal Articles.....	5
1.4. Personnel.....	6
2. Calculations of Volume Electron Currents about the DSX Spacecraft during Transmission	7
2.1. Model Refinements.....	7
2.2. Convergence Status.....	7
2.3. Validation Calculations	8
2.4. DSX Calculations.....	10
3. Electron Energization in the Near Field of the DSX Antenna	13
3.1. Preliminary Results.....	14
3.2. Discussion.....	17
3.2.1. Comparision with Vacuum Radiated Power	17
3.2.2. Comparison with Ion Energization	18
3.2.3. Comparison with Ohmic Heating in the Antenna	18
3.2.4. Power Components	18
4. Electron Currents	19
4.1. Calculated Currents Compared with Thermal Current	21
4.2. Simple Estimates for Peak Current	21
4.3. Comparison with Antenna Current	22
4.4. Dynamics of Electron Current to Contracting Sheath	23
5. Vector Potential About DSX during Transmission	25

6.	Advanced EHF-2 Analysis.....	29
6.1.	Spacecraft and Sensor Tower <i>Object ToolKit</i> models.....	29
6.2.	Thruster Charge Exchange Plume	30
6.3.	Tower Sensors	33
6.3.1.	Space Weather Diagnostics	33
6.3.2.	Plume Diagnostics	34
6.3.3.	Ion Steering.....	35
7.	Review of September 2001 LANL MPA Data.....	38
7.1.	2002 Study using LANL Data	38
7.1.1.	Data.....	38
7.1.2.	Potential Computation	39
7.1.3.	Alternative Predictors	41
7.1.4.	Functional Form.....	43
7.1.5.	Sunlit Periods	45
7.2.	Spectra.....	45
7.3.	Temperature	46
7.4.	Incident Electron Flux.....	50
7.5.	Estimated Barrier	56
7.6.	Correlations.....	58
7.7.	Time Dependence	59
7.8.	Conclusions.....	68
	References	69

List of Figures

	Page
Figure 1. Volume current density near a positively charged sphere for magnetic field in Z. The left hand figures show the current density in the Z (top) and Y (bottom) directions. The pseudopotential is shown in the top right and the actual potential is shown in the bottom right.....	9
Figure 2. Volume current density for magnetic field along (0, 1, 1). The figures show (clockwise from the top left) the current density in Z, the current density in Y, the pseudopotential, and the current density in X (Hall current).....	10
Figure 3. Volume electron currents for magnetic field in the Z direction (normal to the long boom, pointing lefward) in the X=0 plane. The left panel shows the currents before the upwind correction is applied, and the right panel is the result of applying the upwind correction.	11
Figure 4. Volume electron currents in the Y=20 m plane (center of upper antenna element, Z upward, X leftward) corresponding to the configuration of Figure 3, showing that current is indeed flowing along the magnetic field (left panel), and not across the magnetic field (right panel). Some Hall currents can be seen in the right panel.	11
Figure 5. Volume electron currents (X=0 plane, Z pointing leftward) for a magnetic field 15° from Y (15° from the long boom). Left panel is before upwind refinement, and right panel after upwind refinement.	12
Figure 6. Pseudopotentials in the X=0 plane for the magnetic field normal to the antenna (left, corresponding to Figure 3) and for the magnetic field 15° from the antenna (right, corresponding to Figure 5).....	13
Figure 7. Detailed electron energization results for the case of zero magnetic field.....	15
Figure 8. Detailed electron energization results for the magnetic field normal to the antenna.	16
Figure 9. Detailed electron energization results for the magnetic field 15° from the antenna.	16
Figure 10. Detailed electron energization results for the magnetic field along the antenna.....	17
Figure 11. Current patterns near energization peaks with magnetic field parallel to antenna. Left panel is first peak (step 3024). Right panel is second peak (step 3029). Center panel is intermediate dip (step 3026). Note different color scales for the three panels.	20
Figure 12. Current density magnitude for the B=0 case when the sheaths are nearly equal in size. The upper sheath is expanding and the lower sheath is contracting.....	22

Figure 13. Potential at various times (expressed as fractions of the rise time) in a contracting 15 m sheath, assuming both ions and electrons remain stationary.	24
Figure 14. Electric field at sheath with no motion (straight line); Position of outermost particle to reach sheath (upper curve); Electric field seen by said particle (lower curve).	25
Figure 15. Component along the antenna of the vector potential (V) and rate of change of the vector potential (V/s).	26
Figure 16. Magnetic field (V/m) normal to the antenna.	26
Figure 17. X component of the Poynting Vector (W/m/F).	27
Figure 18. Contribution of volume electron currents to the vector potential, its rate of change and the magnetic field.	27
Figure 19. Contribution of transverse surface currents to the vector potential and the magnetic field.	28
Figure 20. Contribution of the volume ion currents to the vector potential and the magnetic field.	28
Figure 21. Artist rendition of spacecraft in orbit (left) and photograph during assembly (right). The thrusters are circled in red and the AFRL Sensor Tower is circled in blue.	29
Figure 22. <i>Object ToolKit</i> model of Advanced EHF-2 spacecraft viewed from two directions. The minimal resolution AFRL Sensor Tower model is the white triangular shape near the top edge of the spacecraft in the center of the right hand figure.	29
Figure 23. <i>Object Toolkit</i> model of AFRL Sensor Tower showing assigned materials.	30
Figure 24. COLISEUM plume ion and neutral densities shown in <i>Nascap-2k</i>	31
Figure 25. Charge exchange ion density and volume potential as computed by <i>Nascap-2k</i> from the plume ion and neutral densities shown in Figure 24.	32
Figure 26. Plume ion and neutral densities for four thrusters operating.	32
Figure 27. Charge exchange ion density and volume potentials as computed by <i>Nascap-2k</i> from the plume ion and neutral densities shown in Figure 26.	33
Figure 28. Potentials in a plane through a Planar Electron Langmuir Probe in a 10^{13} m^{-3} , 4 eV plasma with 100 V on the probe.	34
Figure 29. Potentials in a plane through the Sensor Tower with +100 V on the Planar Electron Langmuir Probes.	35
Figure 30. Potentials on a plane through the AFRL Sensor Tower, annotated.	36

Figure 31. Sample trajectories (blue lines) in potentials shown in previous two figures. The right hand figure also shows the same potentials on a reversed linear scale.....	36
Figure 32. Relative integrated flux as a function of energy as computed by <i>Nascap-2k</i> compared with the analytic solution in the absence of potentials.....	37
Figure 33. Measured chassis potential versus net flux during the eclipse periods, using SAIC computed low energy cutoff and Graphite material properties.	40
Figure 34. Measured chassis potential versus net flux during the eclipse periods, using SAIC computed low energy cutoff, Graphite material properties, and assuming that 19% of the secondary electrons return to the spacecraft.....	40
Figure 35. For eclipse periods, measured chassis potential versus potential computed from minimum in the net flux with measured fluxes adjusted for the proposed potential. Lines are a factor of 1.5 above and below the diagonal. Bars in the right hand graph show the number of measurements for which no solution was found.	41
Figure 36. Measured chassis potential versus potential computed from Equation 2 for the eclipse periods. Lines are a factor of 1.5 above and below the diagonal. Triangles represent plasma with a lower energy density. (See Davis, et al, 2003.) ⁵	42
Figure 37. Measured chassis potential versus potential computed using Equation 3 for the eclipse periods. Lines are a factor of 1.5 above and below the diagonal.....	43
Figure 38. Measured chassis potential versus potential computed from the minimum in the net flux, where the fluxes are computed from a Kappa fit to the measured electron spectrum and a Maxwellian fit to the measured ion spectrum for the eclipse periods.	44
Figure 39. Measured chassis potential versus potential computed from the minimum in the net flux, when the spacecraft is in sunlight assuming 81% of the secondary electrons escape, and including an estimate of the photoemission. There are two measurements for which no solution was found.	45
Figure 40. Differential electron spectra between 22.2 and 1.8 local time on day 255. The right hand graph augments the legend by indicating the measured or inferred chassis potential and the eclipse period during this time.	46
Figure 41. Relationship between the electron temperature moment and the average temperature. Data includes points with both measured and inferred chassis potentials.....	47
Figure 42. Measured chassis potential versus potential computed from Equation 2, with the electron temperature moment used instead of the average temperature for the eclipse periods. Lines are a factor of 1.5 above and below the diagonal.....	48
Figure 43. Relationship between the temperature parameter of a Maxwellian fit (using a linear fit to the logarithm of the flux versus the energy) and the temperature moment.....	49

Figure 44. Relationship between the temperature parameter of a Maxwellian fit (using linear least square fitting) and the temperature moment.....	49
Figure 45. Relationship between the temperature parameter of a Maxwellian fit (using linear least square fittings) and the average temperature.....	49
Figure 46. Measured chassis potential versus the average temperature and the temperature parameter of the fit.....	50
Figure 47. Measured chassis potential versus incident integral electron flux above the barrier energy on linear and logarithmic scales for the eclipse periods.....	51
Figure 48. Measured chassis potential versus incident integral electron flux on linear and logarithmic scales when the spacecraft is in sunlight	51
Figure 49. Measured chassis potential versus incident electron flux over 9 keV during the eclipse periods (left) and when the spacecraft is in sunlight (right).	52
Figure 50. Temperature moment versus high energy electron flux (> 9 keV) during the eclipse periods (left) and when the spacecraft is in sunlight (right).	53
Figure 51. Figure 4 from Reference 3 showing measured chassis potential versus simultaneously observed electron fluxes in different energy channels.....	54
Figure 52. Measured chassis potential versus differential electron flux in two energy channels, without (left) and with (right) the reduction in flux due to the chassis potential.....	54
Figure 53. Measured chassis potential versus the differential electron flux in each energy channel, including the reduction in flux due to the chassis potential.	55
Figure 54. Chassis potential versus differential electron flux to the 10.5 keV energy channel, including the reduction in flux due to the chassis potential. Measurements made during the eclipse periods on days 252 and 255 are identified.	55
Figure 55. Differential electron flux spectra in the ambient plasma during the eclipse periods when the chassis potential is near -948 V (left) and near -317 (right). The different symbols correspond to measurements made at different times.....	56
Figure 56. Differential electron flux spectra in the ambient plasma when the spacecraft is in sunlight and the chassis potential is near -948 V (left) and -317 V (right). The different symbols correspond to measurements made at different times and are labeled by the measured barrier heights.	56
Figure 57. Estimated barrier versus chassis potential when the spacecraft is in sunlight.	57
Figure 58. Estimated barrier versus the average temperature (left) and the electron temperature moment (right) when the spacecraft is in sunlight.....	57

Figure 59. Estimated barrier versus the electron integral flux when the spacecraft is in sunlight. The flux over the maximum of 30 eV and the barrier estimate is shown on the left and the flux over 9 keV is shown on the right.....	58
Figure 60. Time dependence of various parameters for day 271 of 2001, including explanatory annotations.	60
Figure 61. Time dependence of various parameters for day 266 of 2001.....	61
Figure 62. Time dependence of various parameters for day 272 of 2001.....	62
Figure 63. Time dependence of various parameters for day 245 of 2001.....	63
Figure 64. Time dependence of various parameters for day 246 of 2001.....	64
Figure 65. Time dependence of various parameters for day 248 of 2001.....	65
Figure 66. Time dependence of various parameters for day 253 of 2001.....	66
Figure 67. Time dependence of various parameters for day 258 of 2001.....	66
Figure 68. Time dependence of various parameters for day 259 of 2001.....	67
Figure 69. Time dependence of various parameters for day 273 of 2001.....	67

List of Tables

	Page
Table 1. Parameters and calculated average electron energization for four magnetic field orientations.....	14
Table 2. Comparison of time-averaged power deposited in charged particle motion and resulting fields.....	19
Table 3. Maximum current during switch for various magnetic field directions compared with plasma electron thermal current.....	21
Table 4. Estimated currents to fill or empty the sheath in 2×10^{-5} s.	21
Table 5. Parameters for contracting spherical sheath model.....	23
Table 6. Typical geosynchronous currents compared with instrument sensitivities.	34
Table 7. Pearson product-moment correlation coefficients. Blue values indicate the most nearly predictive correlations.....	58

1. Introduction

In support of the larger goal to provide a plasma engineering capability to the spacecraft community, the objective of the *Spacecraft Charging Modeling—Nascap-2k* contract is to develop, incorporate, test, and validate new algorithms for the three-dimensional plasma-environment spacecraft interactions computational tool, *Nascap-2k*. *Nascap-2k* is being modified to extend the range of plasma physics phenomena that the code can simulate, make the advanced code capabilities more accessible to users, and improve and maintain both the graphical and non-graphical interfaces to the code. The upgraded code is being used to simulate problems of interest to AFRL, including support of the DSX (Demonstration and Science eXperiments) spacecraft and program.

1.1. Second Year Progress

Details on progress during the period from September 22, 2012 through September 20, 2013 are given in the following sections. Key accomplishments are the following:

- Prepared and sent *Nascap-2k* 4.2 alpha 4, for Win-32, Win-64, and LINUX, to AFRL for testing.
- Wrote a stand-alone Java program to convert a COLISEUM plume file into an XML plume description file for *Nascap-2k*.
- Modified *Nascap-2k* to be able to automatically create macroparticles at surfaces and optionally use them to compute currents to surfaces using the reverse trajectory technique.
- Used *Nascap-2k* to model DSX electron currents and electron energization.
- Used *Nascap-2k* to model Advanced EHF-2 and the AFRL Sensor Tower. We calculated the effect of a 100 V bias on the planar Langmuir Electron Probe on the RPA and Flux Probe measurements.
- Reviewed the SAIC 2002 project “Characterization of Magnetospheric Spacecraft Charging Environments Using the LANL Magnetospheric Plasma Analyzer Data Set” and further examined the dataset used in that study for insight into parameters that could be used as a charging index.

1.1.1. Interoperability of *Nascap-2k* with Other Codes

The task to make *Nascap-2k* work well with other software includes four subtasks, one of which was addressed during the second year:

- Implement framework for interoperability with the AFRL/RZSS plasma thruster simulation code COLISEUM.

In support of the Advanced EHF program, we wrote a Java program that reads a file from COLISEUM (as represented in the sample format) and converts the contents to a XML plume description file for *Nascap-2k*. The input file is assumed to be a tecplot file with headers that

contain the following strings: "x (m)", "y (m)", "z (m)", "nd-ave.xe (#/m³)", "nd-ave.xe+ (#/m³)", "nd-ave.xe++ (#/m³)", "u-ave.xe+ (m/s)", "v-ave.xe+ (m/s)", "w-ave.xe+ (m/s)", "u-ave.xe++ (m/s)", "v-ave.xe++ (m/s)", "w-ave.xe++ (m/s)". Other headers are ignored. The COLISEUM plume is azimuthally averaged to give an R-Theta plume for the R and Theta values in the provided file Template.xml. The single and double ion densities and velocities are combined to give the correct currents. The code was delivered to AFRL.

1.1.2. Enhanced Plasma Simulation

The task to enhance *Nascap-2k*'s plasma simulation capabilities includes five subtasks, one of which was addressed during the second year:

In support of the Advanced EHF program, we added a generalized particle injection capability to *Nascap-2k*. Macroparticles can be created at surfaces and these macroparticles can be used to compute currents to surfaces using the reverse trajectory technique. *Nascap-2k* now has the following capabilities:

- Users can define emitters and detectors in *Object Toolkit* and view them on the *Nascap-2k Results3D* tab.
- Users can specify the distribution of initial particle positions and velocities within *Object Toolkit*, within the *Nascap-2k* user interface, or in the text input files.
- The code generates macroparticles at surfaces.
- The code can use macroparticles generated at surfaces to compute currents to the initial surface.

1.1.3. Maintenance and Support

Maintenance and support activities during this period included the following:

Software

- Updated MacOS X and LINUX ports of *Nascap-2k*, including standard test cases. The LINUX port was largely funded by the PETTT program as part of the effort to adapt *Nascap-2k* to a multi-threaded, distributed-memory environment.
- Built *Nascap-2k* for the 64-bit Windows environment, and ran all of the standard test cases.
- Delivered *Nascap-2k* 4.2 alpha 3 to AFRL on October 18, 2012 for testing. This version was also delivered to NASA/JPL.
- Delivered *Nascap-2k* 4.2 alpha 4 to AFRL on April 22, 2013 for testing. Delivered distributable LINUX version to AFRL on June 6, 2013.
- Built latest version of *Nascap-2k* on DoD HPCMP computer at ERDC Garnet so that the code will be available for continuing development.

- Added a discussion of shadowing to *Nascap-2k Scientific Documentation*.
- Updated the documentation to reflect all the recent code changes.

User Support

- Assisted Chris Roth of AER with calculations of the Freja floating potential by answering question regarding *Nascap-2k* timesteps and capacitance.
- Discussed appropriate techniques for calculating floating potentials in dense plasma with Dr. Dale Ferguson of AFRL.

Science

- Made minor improvements to the simple Java computer tool that can be used to determine the electron induced secondary yield material properties parameters that give the best fit to measured data. Delivered version 1.0 to AFRL.

1.1.4. Apply *Nascap-2k* to DSX

Using the pseudopotential finite element algorithm with upwind refinement, we computed the volume electron current about DSX for three orientations of the magnetic field using existing potential and ion density calculations as input. The present algorithm provides only a poorly converged solution when the magnetic field is in the Y direction (parallel to the antenna), but is able to converge with the magnetic field 15° from Y. Further details on the algorithm, the validation calculations, and the DSX calculations are in Section 2.

The results of the pseudopotential electron volume current calculations were used to compute the energization of the electrons. Further details are in Section 3. The electron currents are much larger than thermal currents when the antenna elements switch polarity. Their magnitude is consistent with sheath dynamics and small presheath fields are sufficient to move electrons into the contracting sheath. Further discussion is in Section 4.

We added the ability to specify the injection element for the computation of transverse surface currents in *Object Toolkit*. Previously, it was necessary to add the specification to the object definition file using a text editor.

We repeated earlier calculations of self-consistent space potentials and ion densities for a 1 kV square wave applied to the DSX emitting antenna at 10 kHz (10^8 m^{-3}), 2 kHz (10^9 m^{-3}), and 12 kHz (10^9 m^{-3}) using the most up-to-date code. The results show no obvious differences from those obtained previously. The code is more stable and there was less need for code restarts.

We computed the vector potential, its time derivative, and the magnetic field generated by charged particle currents for the 10 kV, 10^8 m^{-3} , 1 eV simulation. The results are shown in Section 5. At this plasma density, the propagating electromagnetic field is mostly due to the transverse surface currents with a significant contribution from the volume electron currents. At higher densities, the volume current contribution would be much larger.

1.1.5. Advanced EHF Analysis

During this period, we continued our analysis of how each environment sensor of the AFRL sensor tower will respond to the various environments.

We built a high resolution *Object Toolkit* model of the AFRL Sensor Tower.

We wrote a Java program to import an HET plume model from COLISEUM and export it in a format that can be read by *Nascap-2k*. Using this plume, we self-consistently computed the space potentials and the densities of the charge exchange ions. This computation also gives the fluxes of charge exchange ions to surfaces.

We reviewed the available information on the AFRL Sensor Tower instruments and estimated their likely response to the geosynchronous plasma environment. Using reverse trajectory calculations, we calculated the effect of a 100 V bias on the planar Langmuir Electron Probe on the RPA and Flux Probe measurements.

Details of our analysis in support of the Advanced EHF program during the first two years of this project appear in Section 6.

1.1.6. Charging Index

We supported AFRL's Geosynchronous Daytime Charging Index Project in the following ways:

- Reviewed Ferguson and Wimberly, The Best GEO Daytime Spacecraft Charging Index, AIAA 2013-0810, its references, and related material.
- Reviewed the SAIC 2002 project "Characterization of Magnetospheric Spacecraft Charging Environments Using the LANL Magnetospheric Plasma Analyzer Data Set".
- Further examined the dataset used in the 2002 study. A full discussion of our analysis and conclusions appears in Section 7.
- Reviewed the LANL MPA data available on the web and used provided tools to examine it. We determined that programmatically accessing data in cdf files is straightforward. Full spectral information is only available for some days.
- Located and provided *Object Toolkit* models of the DSCS spacecraft, both the full and mini models.
- Built an *Object Toolkit* model of the SCATHA spacecraft appropriate for *Nascap-2k* calculations. The model was built using descriptions of the spacecraft and the NASCAP/GEO 4-grid model of SCATHA. The material properties and the proportions of the surface materials on the body were taken from the NASCAP/GEO model. Details were taken from the following documents:
 - J.R. Stevens and A.L. Vampola, *Description of the Space Test Program P78-2 Spacecraft and Payloads*, SAMSO TR-78-24, 1978,
 - J.F. Fennell, *Description of P78-2 (SCATHA) Satellite and Experiments*,
 - R.C. Olsen, C.W. Norwood, Spacecraft-Generated Ions, *JGR*, 96, p. 15951, 1991,

- R.C. Olsen, D.R. Lowery, J.L. Roeder, Plasma Wave Observations During Electron Beam Experiments at High Altitudes, *JGR*, 94, p. 17267, 1989,
- P.D. Craven, R.C. Olsen, J. Fennell, D. Croley, T. Aggson, Potential Modulation on the SCATHA Spacecraft, *J Spacecraft & Rockets*, 24, p. 150, 1986,
- V.A. Davis and L.W. Duncan, *Spacecraft Surface Charging Handbook*, PL-TR-92-2232, 1992,
- N.A. Saflekos, M.F. Tautz, A.G. Rubin, D.A. Hardy, P.F. Mizera, J. Feynman, Three-Dimensional Analysis of Charging Events on Days 87 and 114, 1979 From SCATHA, *Spacecraft Charging Technology*, 1980, NASA CP 2182, AFGL-TR-81-0270, 1981,
- P.R. Stannard, I. Katz, M.J. Mandell, J. J. Cassidy, D.E. Parks, M. Rotenberg, P.G. Steen, *Analysis of the Charging of the SCATHA (P78-2) Satellite*, NASA CR-165348, SSS-R-81-4798.
- Adapted code previously written to generate a *Nascap-2k* script for a spinning spacecraft in a magnetic field. We added the ability to write a script when the spacecraft is also spinning with respect to the sun direction. We delivered the revised code to AFRL.

1.2. Reports and Meetings

Dr. Myron J. Mandell attended the ISO WG4 meeting in Boulder, Colorado on October 10 to 12, 2012.

Dr. Myron J. Mandell attended the workshop “Spacecraft Charging Potential Estimation in the Worst Case Environments” in Japan on January 22 and 23, 2013 as part of the ISO project to define a new standard on simulating spacecraft charging. As sponsors of the meeting, the Society of Japanese Aerospace Companies paid the travel expenses.

Dr. Victoria Davis attended the kickoff of AFRL’s Geosynchronous Daytime Charging Index Project at AFRL at Kirtland AFB on April 8, 2013.

While at AFRL for the kickoff, she also briefed AFRL staff on electron energization during DSX operations. On April 23, 2013, we presented the same material and the results of the calculations of the vector potentials and related quantities to AFRL and Dr. Greg Ginet via teleconference.

All presentations are included in the quarterly report for the relevant period.

1.3. Scientific Reports and Journal Articles

The paper

Comparison of low Earth orbit wake current collection simulations using *Nascap-2k*, SPIS, and MUSCAT computer codes, V.A. Davis, M.J. Mandell, D.C. Cooke, A. Wheelock, J.-C. Matéo-Vélez, J.-F. Roussel, D. Payan (CNES), M. Cho, K. Koga,

which was supported by this contract, will be published in an upcoming special issue of *IEEE Transactions on Plasma Science*.

1.4. Personnel

The project staffing remains as specified in the proposal. Dr. Victoria A. Davis is the project manager and Dr. Myron J. Mandell is the principal investigator. The following SAIC staff members have contributed to the work reported here.

- Dr. Victoria A. Davis
- Dr. Myron J. Mandell
- Dr. Robert A. Kuharski
- Ms. Barbara M. Gardner
- Dr. Michael Brown-Hayes

2. Calculations of Volume Electron Currents about the DSX Spacecraft during Transmission

It is desirable to have a non-PIC (particle-in-cell) method to calculate volume electron currents that satisfy the equation of continuity, other physical requirements, and are consistent with other *Nascap-2k* calculated quantities (*e.g.*, Hybrid PIC). We previously developed a pseudopotential approach to computing volume electron currents consistent with *Nascap-2k* Hybrid PIC computed potentials and ion densities. This approach and some validation calculations are documented in the first annual report for this contract¹.

The method can be used to calculate electron currents within and near the sheath about a VLF antenna or other high-voltage object at frequencies that are low compared with both the electron plasma frequency, ω_{pe} , and the electron cyclotron frequency, ω_{ce} . The currents can then be used to calculate electromagnetic radiation, ohmic heating, etc.

The details of the approach have now been further refined and additional validation calculations performed. The approach has been applied to the results of earlier Hybrid PIC calculations of the plasma about the DSX antenna.

2.1. Model Refinements

This year the implementation of the finite element approach to the model was extended to include the interface of two adjacent grids with equal resolution. Interfaces between grids are incorporated into the matrix equation by the inclusion of constraint equations. To avoid unphysical results where two subdivided grids meet a coarser grid it is necessary for the inner grid nodes that are face centers in the coarse grid to be handled first, with the constraint transformation being formally applied to assign all the matrix elements in the interface plane to outer grid nodes. Remaining matrix elements to constrained nodes can then be straightforwardly assigned to unconstrained nodes with no fudge factors.

The volume electron current density algorithm works well for most cases tried. However it has the drawback that the solution often shows small (~10%) unphysical current discontinuities at grid boundaries. We have come to believe that these discontinuities are a natural result of the finite element solution with trilinear interpolation. In order to eliminate these current discontinuities, we have developed an “upwind” technique to refine the finite element solution. In this algorithm the input current to each element is calculated, and then the magnitude of the cell current (now redefined as output current) is adjusted (after accounting for the known charge accumulation rate) to maintain charge conservation. The current direction calculated by the finite element solution is preserved. Presently, we are applying five iterations of this algorithm.

Two additional alternatives that are not being pursued at this time are (1) to try the unconditioned Conjugant Gradient algorithm for solution of the matrix equation and (2) to use higher order interpolants, as are used in the potential solution.

2.2. Convergence Status

The current algorithm converges well for the sphere test problem and for a small antenna test problem for all orientations of magnetic field. It converges for the full DSX problem for no

magnetic field and for magnetic field in the Z direction (normal to the antenna). The algorithm has difficulty converging for the full DSX problem when the magnetic field is in the Y direction (along the antenna). We have achieved reasonable convergence with the magnetic field 15° from the Y direction. Results for the magnetic field along the antenna should be used with an awareness of the poor convergence.

2.3. Validation Calculations

Solutions were computed for a sphere in a computational space with a complex grid structure with the magnetic field along the axis and diagonally. The outer grid contains two adjacent equally subdivided subgrids. Results are shown in Figure 1 and Figure 2. After implementing the refinements, the interface between the adjacent equally subdivided regions is not visible. The interface between the coarser and more refined grids can be seen in the upper left figure of Figure 1. We believe this discontinuity is an unavoidable result of the trilinear interpolation. As diagnostic for the algorithms, the ability to view the pseudopotential was added to the interface. The pseudopotential is also shown in the figures.

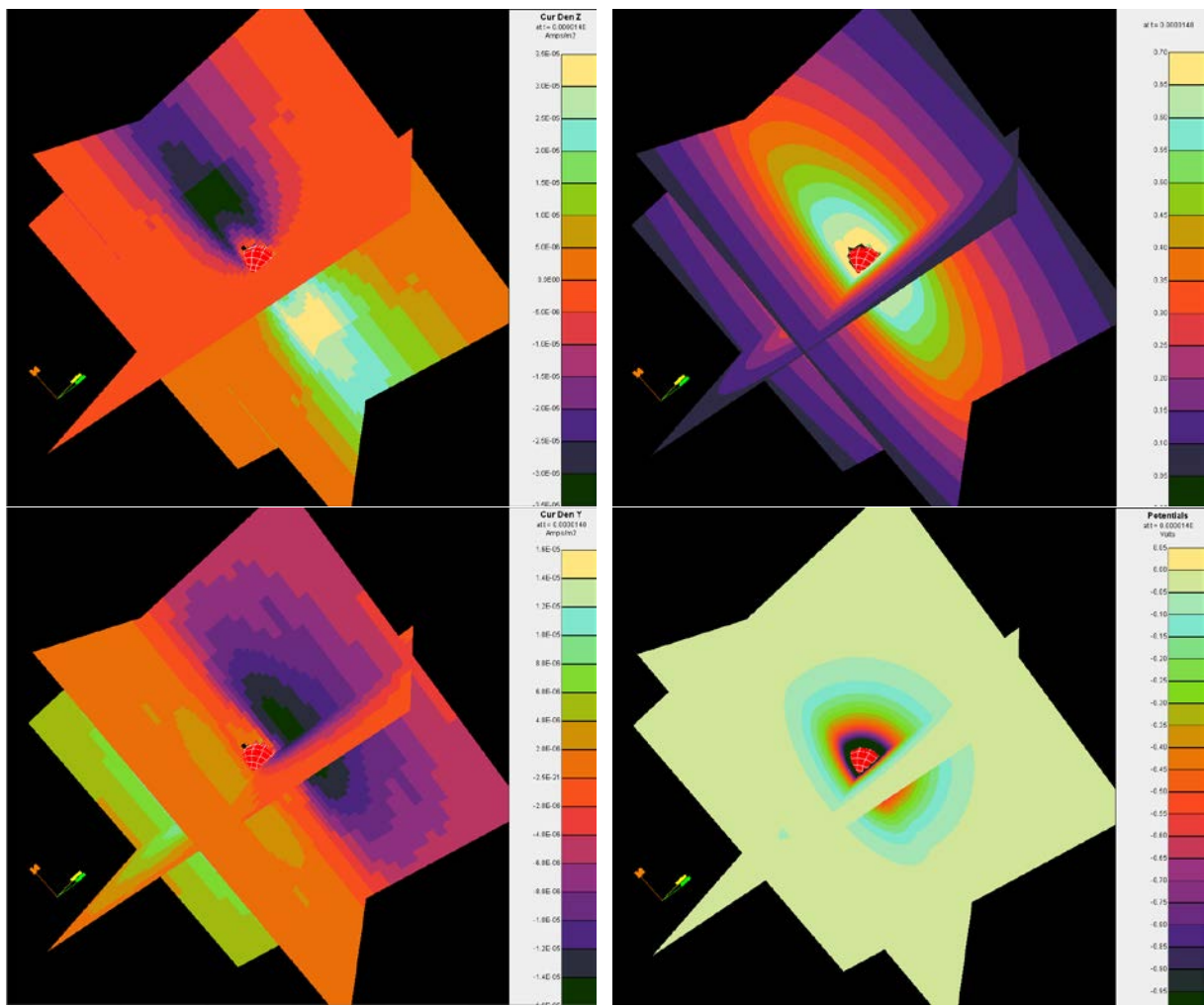


Figure 1. Volume current density near a positively charged sphere for magnetic field in Z. The left hand figures show the current density in the Z (top) and Y (bottom) directions. The pseudopotential is shown in the top right and the actual potential is shown in the bottom right.

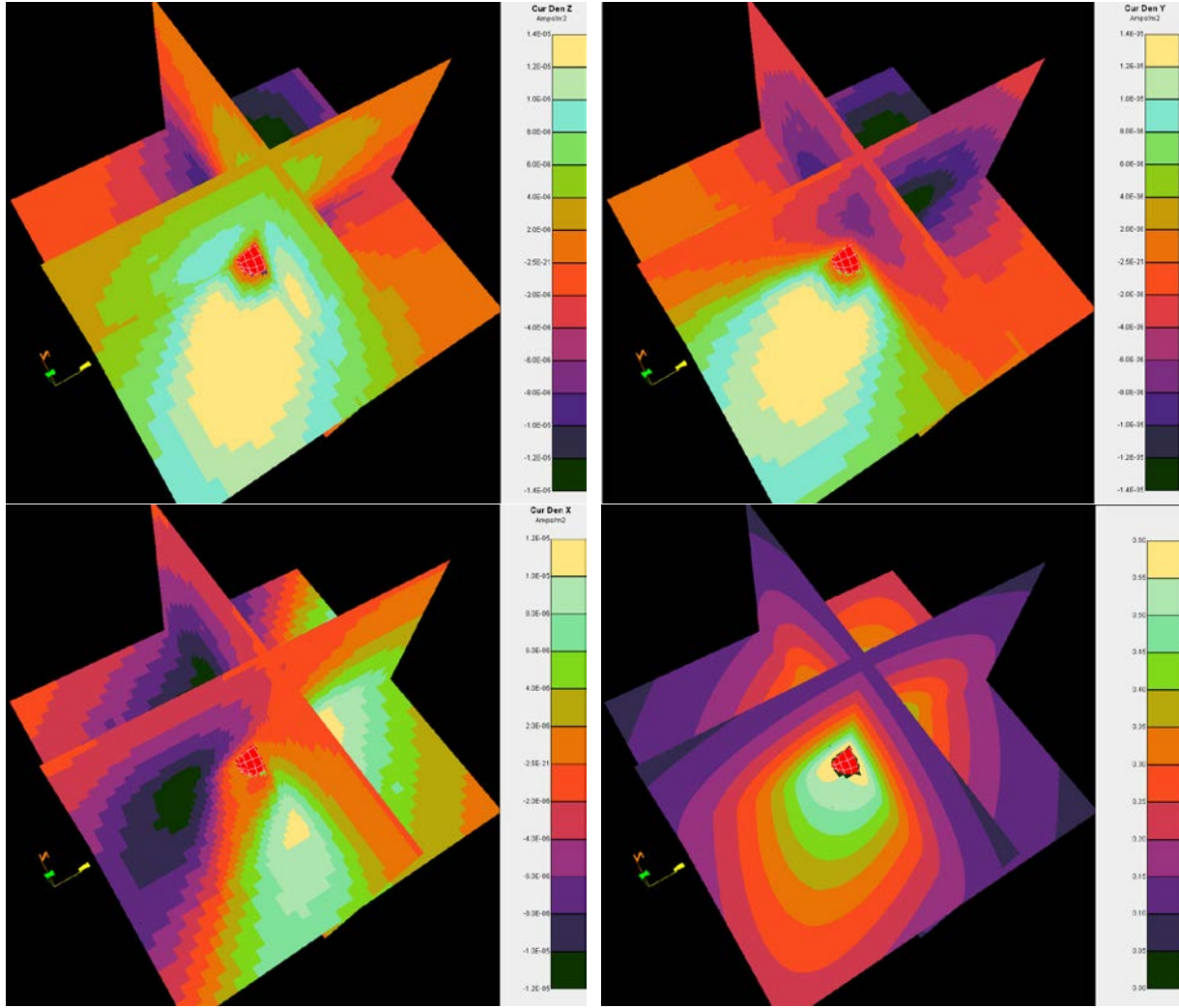


Figure 2. Volume current density for magnetic field along (0, 1, 1). The figures show (clockwise from the top left) the current density in Z, the current density in Y, the pseudopotential, and the current density in X (Hall current).

2.4. DSX Calculations

The volume electron currents were computed using potentials from the earlier Hybrid PIC 10 kHz, $1 \times 10^8 \text{ m}^{-3}$ simulations.² Figure 3 shows currents for the case of magnetic field (5×10^{-6} Tesla) normal to the antenna at the time that the antenna elements are at nearly equal potential, and the current flow in the antenna is maximum. Current is flowing outward from the upper antenna element (whose sheath is expanding), and inward toward to lower antenna element (whose sheath is contracting). These counterstreaming currents may be effective in exciting plasma modes. The difference between the left and right panels of Figure 3 shows the improvement made by applying the “upwind” refinement, which removes the current discontinuity at the grid boundary. Figure 4, showing a plane through the center of the upper antenna element, illustrates that current is indeed flowing along the magnetic field (left panel), and not normal to the magnetic field (right panel). Note, however, that the right panel shows some Hall currents induced by the Y component of the gradient of the pseudopotential.

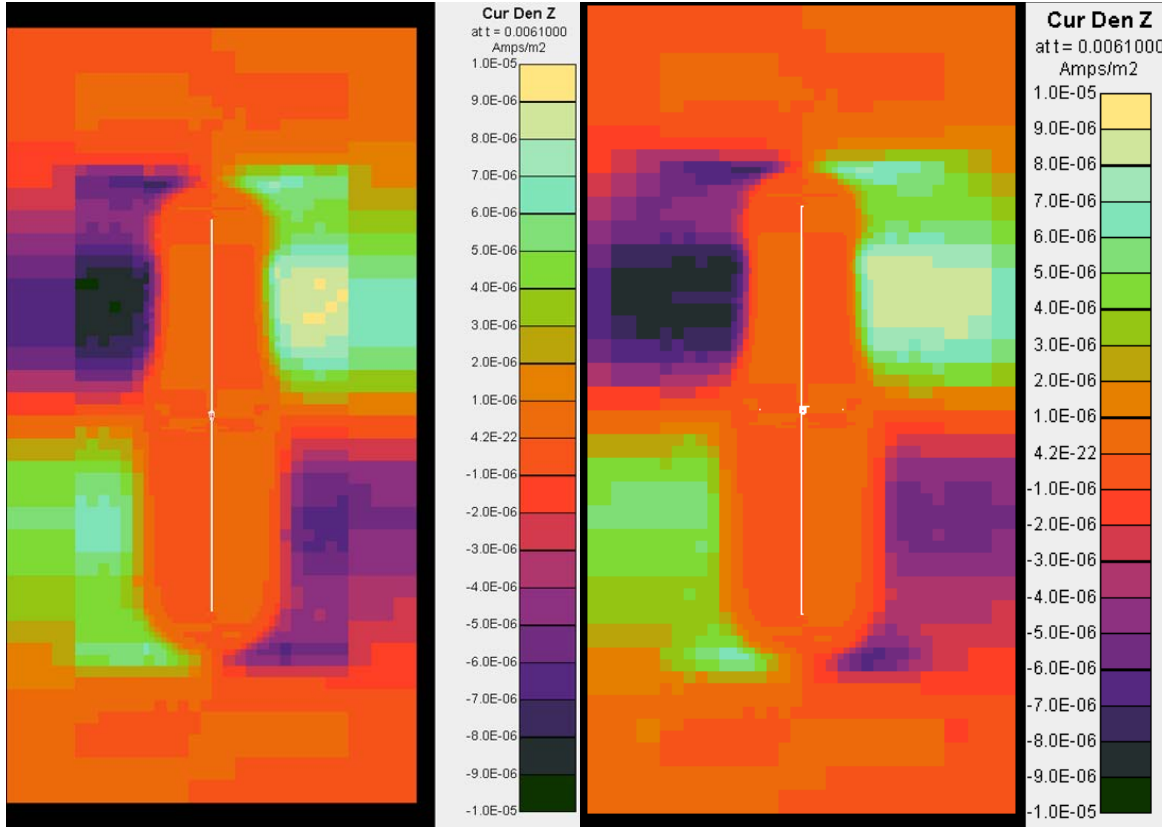


Figure 3. Volume electron currents for magnetic field in the Z direction (normal to the long boom, pointing lefward) in the X=0 plane. The left panel shows the currents before the upwind correction is applied, and the right panel is the result of applying the upwind correction.

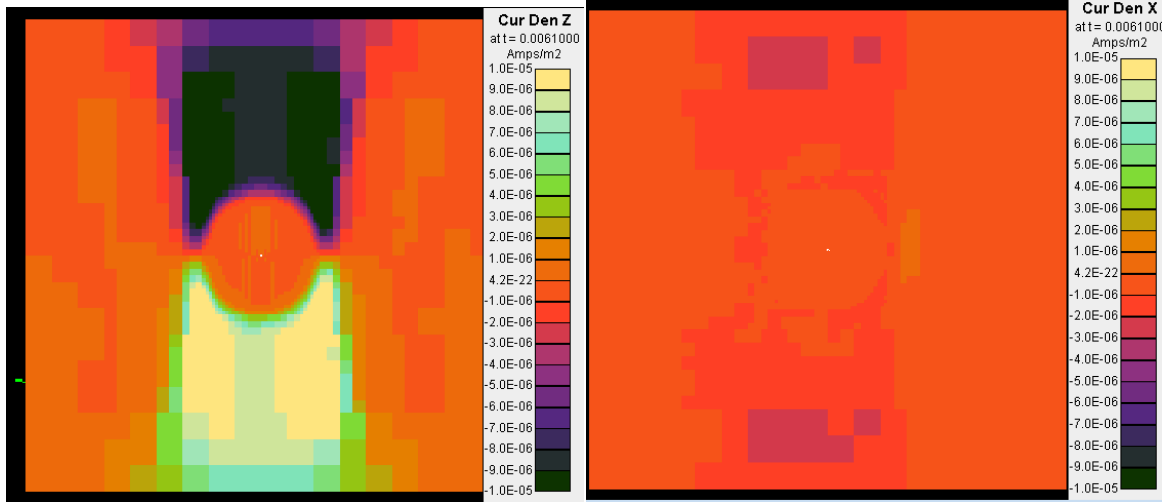


Figure 4. Volume electron currents in the Y=20 m plane (center of upper antenna element, Z upward, X lefward) corresponding to the configuration of Figure 3, showing that current is indeed flowing along the magnetic field (left panel), and not across the magnetic field (right panel). Some Hall currents can be seen in the right panel.

Figure 5 shows the electron currents for the case of the magnetic field 15° from parallel to the antenna. The expanding sheath about the upper antenna element is expelling electrons both downward to the right and upward to the left, and the contracting sheath about the lower antenna element is receiving electrons similarly. Relative to Figure 3, this configuration produces higher current intensity with higher shear in the current pattern, which may be more effective at exciting plasma modes.

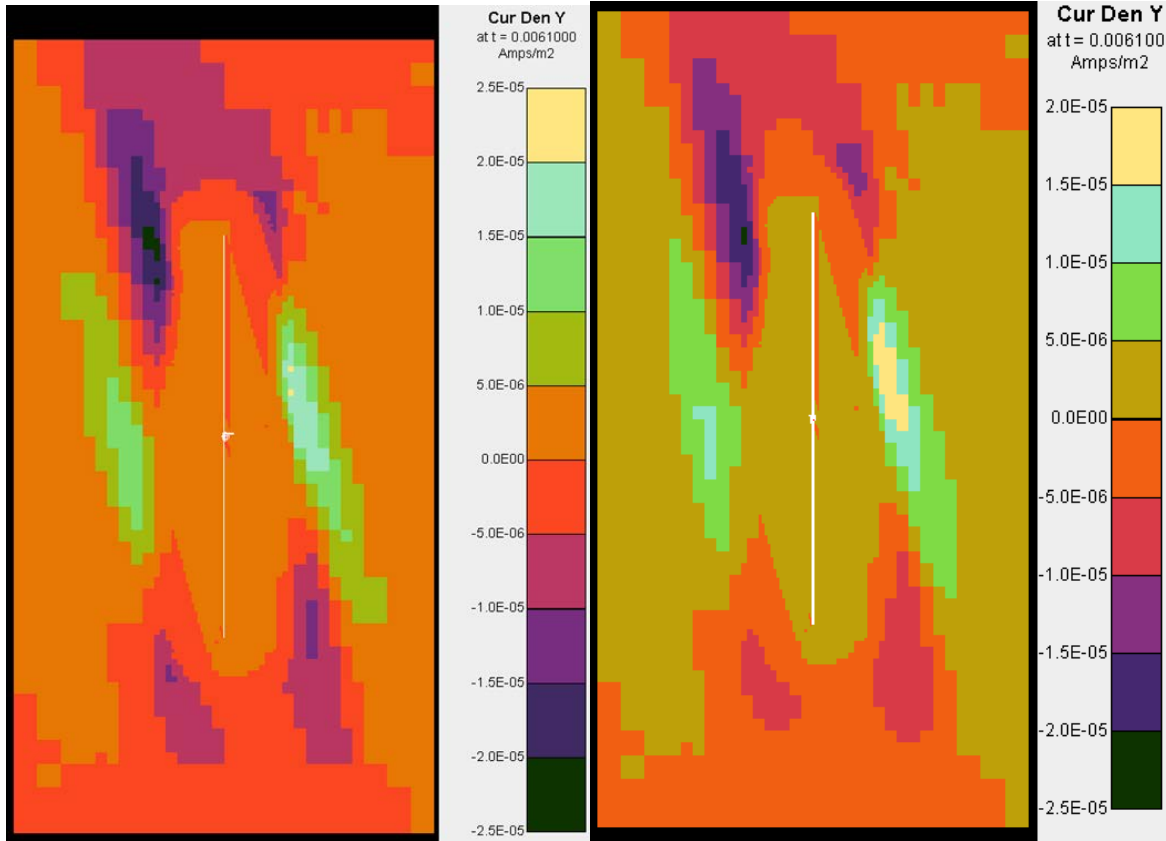


Figure 5. Volume electron currents (X=0 plane, Z pointing leftward) for a magnetic field 15° from Y (15° from the long boom). Left panel is before upwind refinement, and right panel after upwind refinement.

Figure 6 shows the pseudopotential fields corresponding to Figure 3 and Figure 5. Note that the pseudopotentials bear no particular resemblance to the actual potentials, but are simply an artifice for generating electron currents consistent with the *Nascap-2k* generated rate of change of electron density and with the magnetic field modulated plasma conductivity. Hall currents are generated in regions where the pseudopotential has a high gradient in the direction normal to the magnetic field.

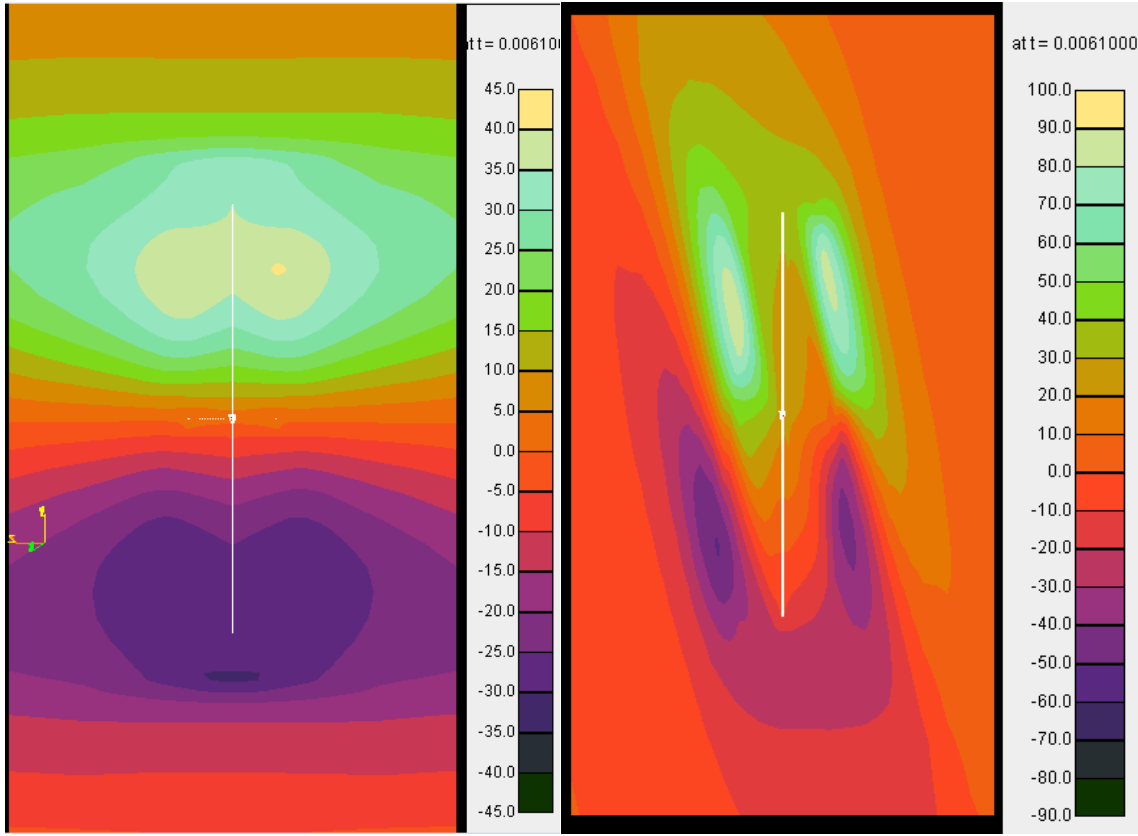


Figure 6. Pseudopotentials in the X=0 plane for the magnetic field normal to the antenna (left, corresponding to Figure 3) and for the magnetic field 15° from the antenna (right, corresponding to Figure 5).

3. ELECTRON ENERGIZATION IN THE NEAR FIELD OF THE DSX ANTENNA

We used volume electron currents consistent with time-dependent electron densities (as calculated by *Nascap-2k* dynamic sheath simulations) to calculate energization of electrons by the sheath electric fields. The energization rate is 50 to 90 mW. Most of the energy coupled to the plasma consists of shear currents of energetic electrons that are ejected from the expanding sheath while the antenna elements are switching. This energization is similar in magnitude to that previously computed for the ions.

The local rate of energy deposition into plasma electrons is $\mathbf{J} \cdot \mathbf{E}$. The electron current is outward near an expanding sheath and inward near a contracting sheath. In our calculations for the DSX sheath region, the electric field is mainly repulsive to electrons due to the negative floating potential of the spacecraft. Thus a contracting sheath would contribute a negative $\mathbf{J} \cdot \mathbf{E}$. Later in this report, we show that the current to fill a contracting sheath is driven by small, electron-attracting presheath fields, which are not included in the *Nascap-2k* simulations. We therefore ignore negative contributions to the global energy deposition.

There are two sources of positive energization terms: expulsion of electrons from an expanding sheath, and attraction of electrons toward a positive antenna element. As we shall see below, the sheath expansion is the larger contributor to plasma energization. The argument that attraction of electrons toward a positive antenna contributes to plasma energization (rather than to heating of

the antenna surface) is that, since the antenna is a tenuous structure of thin wires, angular momentum barriers prevent most of the attracted current from being collected by the antenna, so that the energized electrons are instead expelled during the subsequent sheath expansion.

Thus, the global rate, \dot{Q} , of electron energization is calculated by

$$\dot{Q} = \sum_{e \in J \cdot E > 0} V_e \mathbf{J} \cdot \mathbf{E}$$

where V_e is the volume of volume element e , \mathbf{J} is the mean local electron current (calculated using the pseudopotential method) and \mathbf{E} is the local electric field (calculated by *Nascap-2k*) and the sum is over elements in which the electric field energizes the electron current. This instantaneous rate may be averaged over a cycle to obtain a mean rate useful for comparing different cases. The electric field presently used is that derived from the advanced potentials for the timestep. The accuracy of this calculation is limited by time and spatial resolution of the currents and electric fields.

3.1. Preliminary Results

Electron energization was computed for the electron currents calculated for the *Nascap-2k* simulation of a 10 kHz near-square wave at 1 kV in plasma with ambient density 10^8 m^{-3} and temperature 1 eV in four magnetic field orientations. Parameters are shown in Table 1. The currents were calculated for the case of zero magnetic field, magnetic field normal to the antenna, magnetic field 15° from the antenna, and magnetic field parallel to the antenna.

Table 1. Parameters and calculated average electron energization for four magnetic field orientations.

N_e	T_e	Frequency	\mathbf{B}	$\langle \dot{Q} \rangle$
m^{-3}	eV	Hz	Tesla	Watts
10^8	1	10^4	(0,0,0)	0.0524
10^8	1	10^4	(0,0,5×10 ⁻⁶)	0.0629
10^8	1	10^4	(0,4.8×10 ⁻⁶ ,1.3×10 ⁻⁶)	0.0912
10^8	1	10^4	(0,5×10 ⁻⁶ ,0)	0.0815

The total energization as a function of time is shown in Figure 7 for the zero magnetic field case, Figure 8 for the magnetic field normal to the antenna, Figure 9 for the magnetic field nearly parallel to the antenna, and Figure 10 for the magnetic field parallel to the antenna. (Electron currents for the parallel case may not be well-converged.) For all four magnetic field orientations, the variation with time is similar. Peak energization occurs near the time the antenna elements are switching, with subsidiary peaks near the times that one element is positive. The mean energization rate increases as the magnetic field is applied, and increases further as the magnetic field is rotated toward the antenna direction. There is a dip in the energization rate for the case of magnetic field along the antenna, which may (despite poor convergence) be

attributable to electrons from the expanding sheath flowing directly to the contracting sheath, rather than flowing along oblique field lines to the ambient plasma.

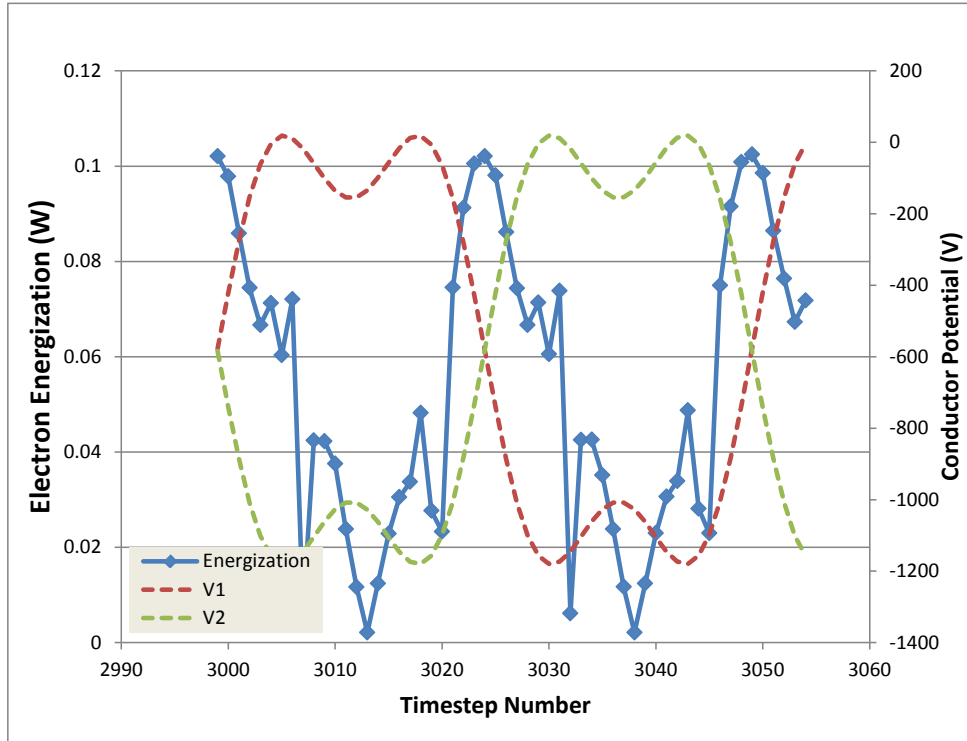


Figure 7. Detailed electron energization results for the case of zero magnetic field.

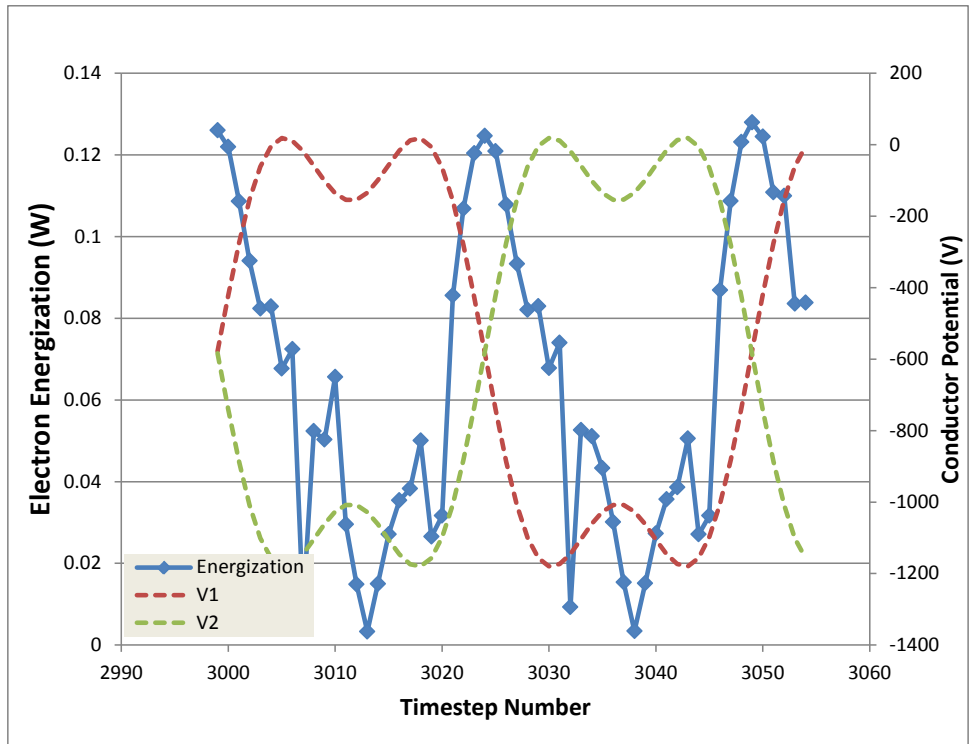


Figure 8. Detailed electron energization results for the magnetic field normal to the antenna.

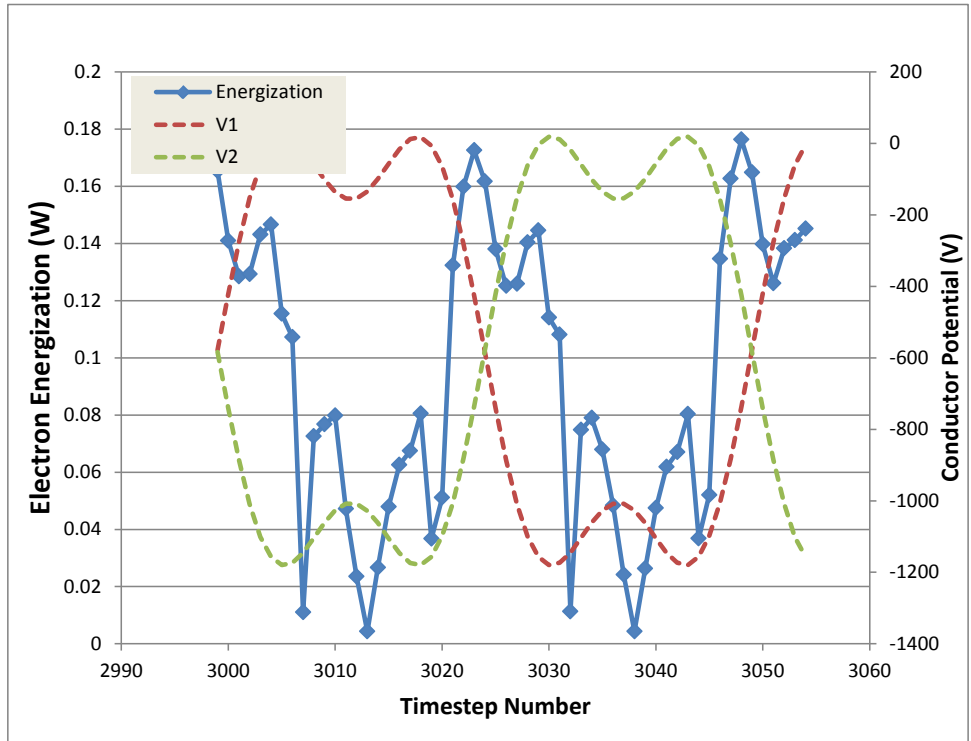


Figure 9. Detailed electron energization results for the magnetic field 15° from the antenna.

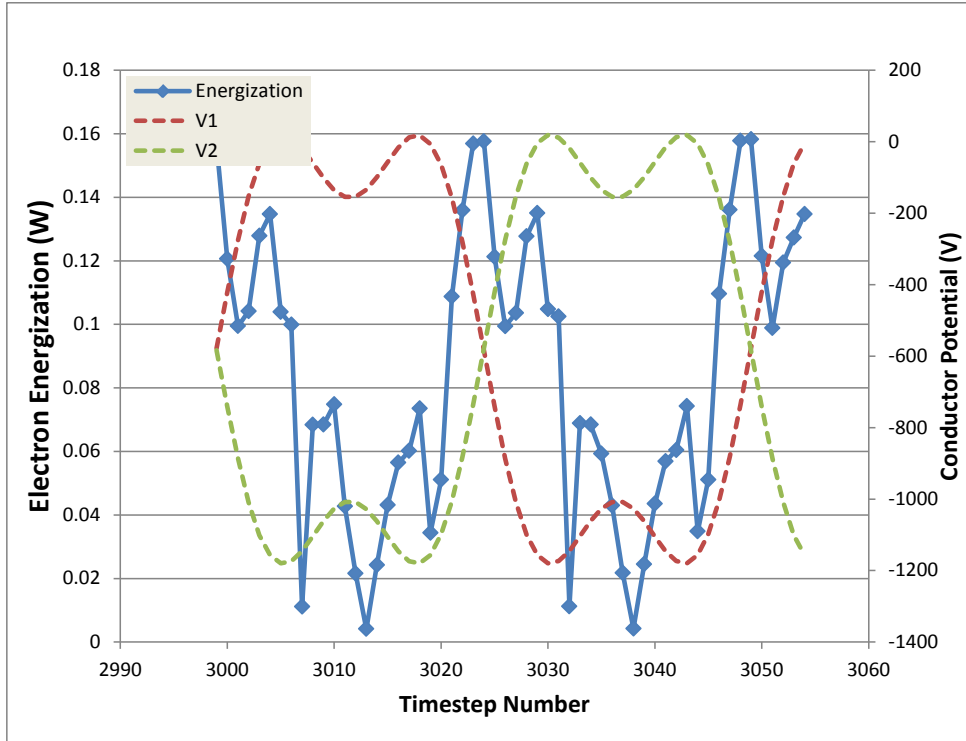


Figure 10. Detailed electron energization results for the magnetic field along the antenna.

3.2. Discussion

The calculated energization rates, shown in Table 1, range from 0.05 to 0.1 watts.

The first question that arises is whether these energization rates are large or small compared with the heat capacity of the plasma. The plasma electron energy density is given by

$\frac{3}{2} N_e e T_e = \frac{3}{2} 10^8 \times 1.6 \times 10^{-19} \times 1 = 2.4 \times 10^{-11} J m^{-3}$. The electron energy created per cycle is greater than $5 \times 10^{-6} J$, corresponding to $2 \times 10^5 m^3$ of plasma. This volume is fairly large compared with the volume of the entire DSX sheath, and certainly much larger than the volume in which energization is occurring. This observation suggests that the effect of driving electron currents through the plasma is to create modulated electron beams of tens or even hundreds of eV along the field lines from the expanding sheath.

Consequently, the results suggest that most of the energy coupled to the plasma consists of shear currents of energetic electrons that are ejected from the expanding sheath while the antenna elements are switching. Presence of magnetic field increases the energy and the shear, which is further increased by rotating the magnetic field from the normal direction toward the parallel direction. The highest energization rate found was with the magnetic field 15° from the antenna.

3.2.1. Comparison with Vacuum Radiated Power

We previously computed the radiated power for the vacuum case to be $0.18 \mu W$ per frequency component.¹ This is much less than the electron energization of 0.05 to 0.1 W calculated in this work.

3.2.2. Comparison with Ion Energization

The power that goes into ion energization is given by calculating the phase shift between the applied voltage and the antenna current in the sheath dynamics calculation and applying $P = \frac{1}{2}VI\cos\delta$. This was done in Reference 1. For this system, the voltage and current in the fundamental frequency are 637 V and 0.0173 A respectively, and the phase shift is 1.565 radians, for a power loss of 32 mW. This energization includes the energy of ions expelled from a repulsive sheath and those that strike the antenna.

The power deposited in the antenna by an incident ion macroparticle can also be computed from the ion current times the potential drop of the incident ions. The calculated average ion current to each antenna element while in the on state is 0.054 mA.² If we use, as an upper limit, 1 keV per deposited ion, then the deposited energy is 54 mW. This suggests that for this plasma density, little of the energy is deposited in escaping ions.

3.2.3. Comparison with Ohmic Heating in the Antenna

Ohmic heating is a loss to the system. Because the actual antenna is a tenuous, multiply-connected structure its resistance is hard to know. As a (probably high) estimate we take the resistance of 22 AWG (1 mm diameter) aluminum wire, which is 26.5 ohms/1000 ft, or

$0.087 \Omega \text{ m}^{-1}$. The ohmic power loss per element is given by $P = \frac{1}{2}\rho \int_0^L I_0^2 \left(1 - \frac{x}{L}\right)^2 dx = \rho I_0^2 L / 6$. As

noted above, I_0 , the current at the antenna root, is 35 mA, so that the ohmic power loss per element is 0.7 mW, for a total ohmic power loss of 1.4 mW. This suggests that the ohmic power loss is small.

3.2.4. Power Components

Table 2 compares the time-averaged power deposited in charged particle motions and electromagnetic fields for this case. The power is deposited primarily in electron motion, which results in modulated electron beams following the magnetic field lines, and ions that are deposited on the antenna, generating heat. At higher and lower plasma densities the results might be very different.

The power level of 50 to 90 mW deposited into electron motion can be compared to an extreme upper limit for this frequency, plasma density, and magnetic field. The entire plasma electron energy density ($2.4 \times 10^{-11} \text{ J m}^{-3}$) moving at the whistler group velocity of $2.5 \times 10^8 \text{ ms}^{-1}$ would create an energy flux of 6 mW m^{-2} through some surface. For an area of 1000 m^2 , this would give an energy flux of 6 W.

Table 2. Comparison of time-averaged power deposited in charged particle motion and resulting fields.

Power deposited in volume electron currents	50-90 mW
Radiated power in vacuum	0.4 μ W
Ohmic heating in antenna	1.4 mW
Power deposited in antenna by incident ions	\leq 54 mW
Power to ions computed from phase shift	32 mW

4. ELECTRON CURRENTS

The *Nascap-2k* sheath dynamics calculations track the detailed ion dynamics but assume the electrons instantaneously adjust to steady-state densities consistent with the calculated potential and ion density. Magnetic field plays no role in the sheath dynamics calculations. The pseudopotential algorithm, which includes anisotropic electron mobility due to the magnetic field, is then used to determine the electron current needed to achieve the calculated time-dependent electron densities.

Figure 3 and Figure 5 of the previous section show the current patterns during switching for the magnetic field normal to the antenna and nearly parallel. The current is largely constrained to move along the field lines, and no current flows within the sheath (as electrons are excluded). For the magnetic field toward antenna-parallel, the broad current regions are constricted, corresponding to smaller projection of the sheath area normal to the magnetic field. This results in higher current densities as well as higher gradients of current between the incoming and outgoing streams.

Figure 11 shows the current patterns during switching for the case of the magnetic field parallel to the antenna. In all three panels electrons are generally moving downward near the tips (light colors) and upward at the center (dark colors) from the expanding (lower) sheath to the contracting (upper) sheath. In the left panel (corresponding to the high peak at the center of Figure 10) the dominant current consists of electrons expelled from the expanding sheath and exiting the bottom of the frame. In the center panel (corresponding to dip between the two high peaks at the center of Figure 10) electrons move upward from the lower (expanding) sheath to the upper (contracting) sheath, which is an easy path since the sheaths are roughly equal in size and the filling and emptying regions are directly connected by magnetic field lines. In the right panel (corresponding to the second peak at the center of Figure 10) the highest current is electrons entering from the top of the frame to fill the contracting sheath, while electrons continue to be expelled from the bottom of the sheath at low current but over a large area.

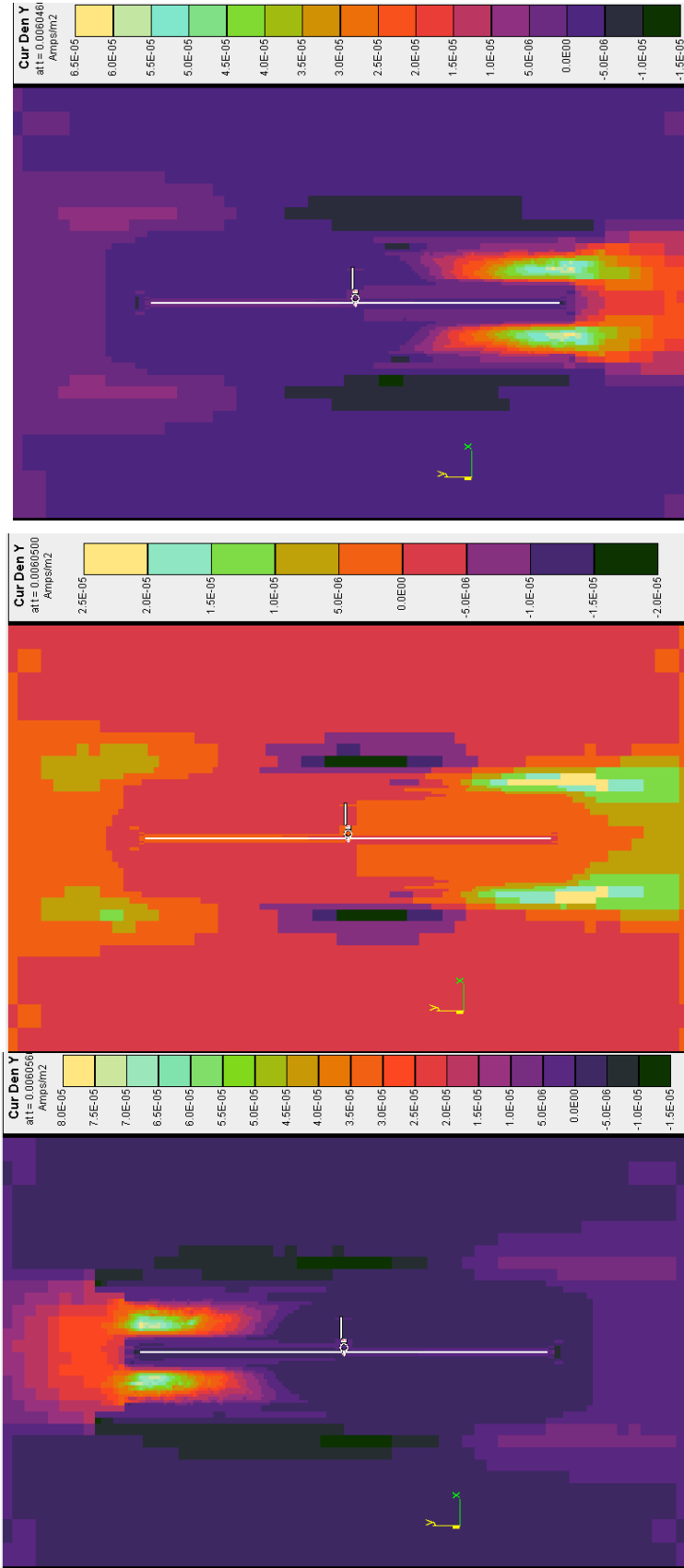


Figure 11. Current patterns near energization peaks with magnetic field parallel to antenna. Left panel is first peak (step 3024). Right panel is second peak (step 3029). Center panel is intermediate dip (step 3026). Note different color scales for the three panels.

4.1. Calculated Currents Compared with Thermal Current

The peak calculated currents in Figure 3, Figure 5, and Figure 11 are considerably in excess of the plasma thermal electron current. Table 3 shows the peak currents from the calculations compared with the electron plasma thermal current. The currents are approximately symmetric between the expanding and contracting sheaths. The peak calculated current is nearly three times the thermal current in the absence of magnetic field. As the magnetic field is applied and rotated from normal to the antenna toward parallel to the antenna the current path becomes constricted and the peak current increases, exceeding the thermal current by an order of magnitude or more.

Table 3. Maximum current during switch for various magnetic field directions compared with plasma electron thermal current.

Magnetic Field (T)	Maximum Current (Am^{-2})
Thermal Current	0.268×10^{-5}
B=(0,0,0)	0.7×10^{-5}
B=(0,0,5×10⁻⁶)	1×10^{-5}
B=(0.4.8×10⁻⁶,1.3×10⁻⁶)	2×10^{-5}
B=(0,5×10⁻⁶,0)	6×10^{-5}

4.2. Simple Estimates for Peak Current

The peak currents can be estimated as the charge that flows into or out of the sheath divided by the time it takes for the antenna elements to switch polarities, which is about 2×10^{-5} s. We approximate the sheath as a cylinder with diameter 30 m and length 50 m. At ambient density, the sheath volume contains 5.65×10^{-7} coulombs of electron charge. The effective area through which the sheath fills or empties is taken as the projection of the cylinder normal to the magnetic field. The currents thus calculated are shown in Table 4. The estimates show the same order as, and similar magnitude to, the calculations. The discrepancy in the B-parallel case results from the current in the simulation being confined to a small volume near the sheath edge (see left panel of Figure 11), so that only a small part of the end cap is effective in collecting or emitting current. The agreement between the estimates and the calculations supports the idea that the high currents are the result of the original assumptions of the sheath dynamics calculations, but does not imply whether or not those assumptions are reasonable.

Table 4. Estimated currents to fill or empty the sheath in 2×10^{-5} s.

Magnetic Field (T)	Estimated Current (Am^{-2})
Thermal Current	2.68×10^{-6}
B=(0,0,0)	4.6×10^{-6}
B=(0,0,5×10⁻⁶)	9.4×10^{-6}
B=(0.4.8×10⁻⁶,1.3×10⁻⁶)	1.6×10^{-5}
B=(0,5×10⁻⁶,0)	2×10^{-5}

4.3. Comparison with Antenna Current

The electrons flow into the contracting sheath and flow out of the expanding sheath, with similar current flowing in the antenna to maintain the charge neutrality of each sheath. Figure 12 shows the near-maximum currents for the case of zero magnetic field. The total electron current leaving the upper sheath is estimated as $6 \times 10^{-6} \text{ Am}^{-2}$ through a cylinder of length 40 m and diameter 29 m, plus $3 \times 10^{-6} \text{ Am}^{-2}$ through a hemispherical end cap, giving 0.026 A. The total electron current entering the lower sheath is estimated as $5 \times 10^{-6} \text{ Am}^{-2}$ through a cylinder of length 40 m and diameter 40 m, plus $3 \times 10^{-6} \text{ Am}^{-2}$ through a hemispherical end cap, giving 0.033 A. From Reference 1, the peak average current density on the antenna is 0.055 A/m. The total current at the antenna root is found by doubling this and multiplying by the circumference of the 0.1 m diameter antenna to get 0.035 A.

Within the accuracy of this estimate, the current leaving the upper sheath, the current at the antenna root, and the current entering the lower sheath are consistent. In addition to the roughness of the sheath current estimate, it should be noted that the electron currents of Figure 12 are not quite at the maximum and that ion motion also contributes to the time dependence of sheath total charge.

Comparison of electron currents with magnetic field normal to the antenna gives similar results.

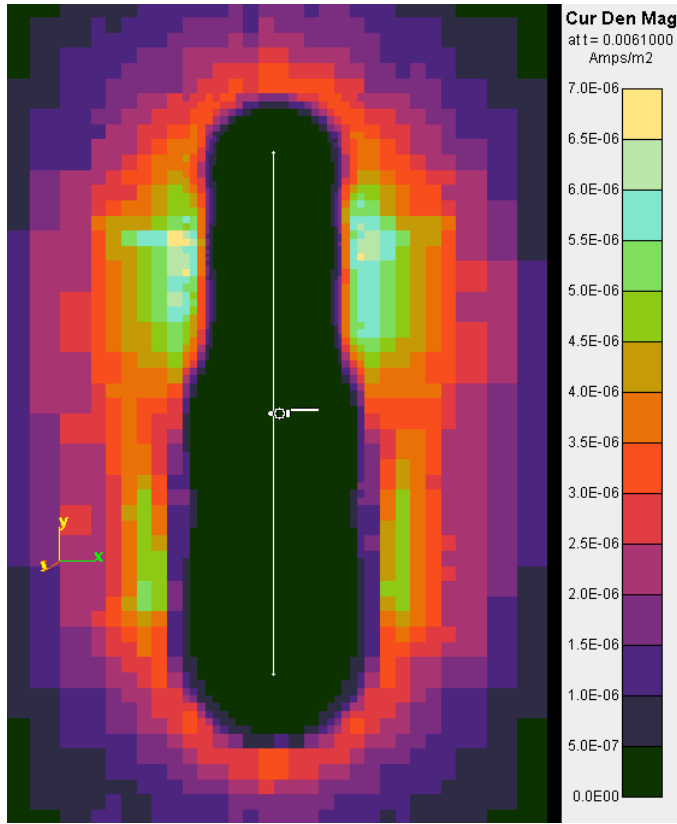


Figure 12. Current density magnitude for the B=0 case when the sheaths are nearly equal in size. The upper sheath is expanding and the lower sheath is contracting.

4.4. Dynamics of Electron Current to Contracting Sheath

In order for electrons to fill the contracting sheath, the contracting sheath must leave positive potentials at its edge to draw electrons from the plasma. This effect is not included in our dynamic sheath simulations, which treat the electrons as massless. The dynamics of the current flow to the contracting sheath is discussed in this section.

High current from the expanding sheath seems reasonable, as the high fields within the sheath serve to accelerate and expel the electrons. However, the contracting sheath is conceptually more difficult, as the high electron currents must be drawn from what was assumed to be quiescent plasma. The contracting sheath (the velocity of the edge of which is comparable to the electron thermal speed) leaves behind an ion-rich region at positive potential that accelerates electrons from deep in the plasma and traps them. A simple simulation of a spherical contracting sheath illustrates this process.

Consider a spherical probe at the center of a spherical sheath with parameters given in Table 5. We consider the sheath initially filled with ions at ambient density and void of electrons, with neutral plasma beyond the sheath radius. Along with Gauss's Law and spherical symmetry, the condition that the potential and electric field both vanish at the sheath radius is sufficient to define the potential within the sheath, which is given by

$$\phi(r) = \frac{Ne}{\epsilon_0} \left(-\frac{R^3}{3r} - \frac{r^2}{6} + \frac{R^2}{2} \right).$$

This equation determines the potential at the probe radius, which is given in the table. Changing the probe potential (by changing the charge on the probe) with no particle motion changes only the inverse radius term of the potential. Further assuming the probe potential rises linearly to zero in the specified rise time gives the set of potential curves shown in Figure 13. The potential at the nominal sheath edge (15 m) rises to 115 V with an electric field of 7.68 Vm^{-1} . This electric field is several times the natural field fluctuations, and sufficient to cause substantial inward electron motion.

Table 5. Parameters for contracting spherical sheath model.

Sheath Radius, R (m)	15
Probe Radius, a (m)	1.5
Ion Density, N (m^{-3})	1×10^8
Probe Initial Potential (V)	-1152.7
Probe Rise Time (s)	2×10^{-5}

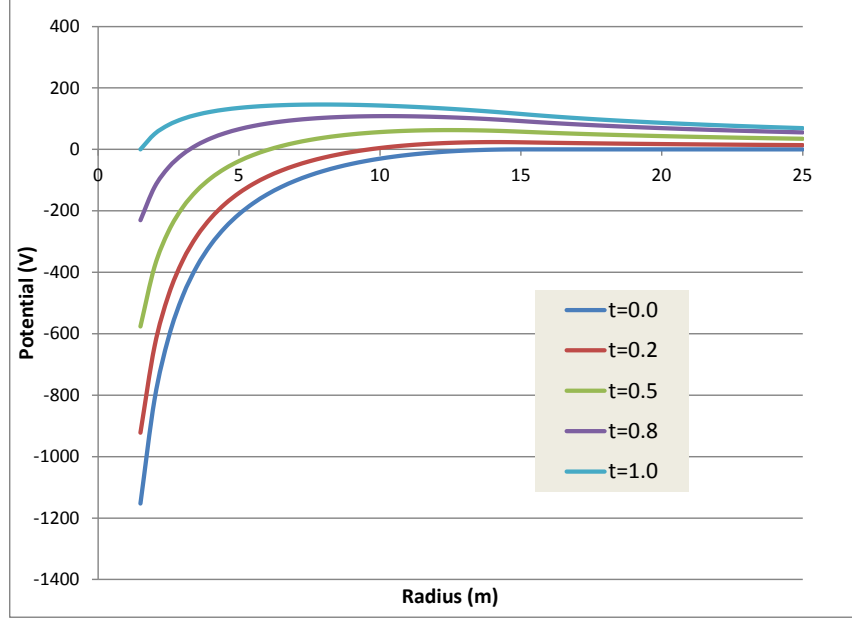


Figure 13. Potential at various times (expressed as fractions of the rise time) in a contracting 15 m sheath, assuming both ions and electrons remain stationary.

Next, we include the inward motion of electrons in the presheath region. An electron that has moved inward from r_0 to r sees a field that is reduced (relative to those shown in Figure 13) by the field due to all the electron charge originally located between r_0 and r , which is now located within r . Thus, the field seen by that particle is

$$E(r(t)) = \frac{Ne}{3\epsilon_0 r^2} \left(\frac{t}{\tau} (R^3 - a^3) - (r_0^3 - r^3) \right)$$

where the charge on the probe (with radius a) goes linearly to zero over a risetime τ , and ion motion continues to be ignored. For the charge in the sheath to equal that on the probe, electrons out to a radius given by $r_0^3 = 2R^3 - a^3$ must enter the sheath. The motion and electric field of an electron starting at this radius is shown in Figure 14. This calculation shows that electric fields no greater than about 0.5 Vm^{-1} at the disturbed region boundary (much less than the 7.68 Vm^{-1} calculated without electron motion) are sufficient to accelerate electrons into the contracting sheath and fill it. The field seen by the test particle oscillates at the electron plasma frequency of just under 10^5 Hz . This demonstrates that the filling of a spherical contracting sheath can be accomplished with only modest disturbances to the surrounding plasma. Because, unlike the case of the expanding sheath, electrons are excluded from the high field region and see only weak presheath electric fields, it appears likely that, even though currents in excess of the plasma thermal current are required, the contracting sheath can be filled with only minor disturbance of the ambient plasma.

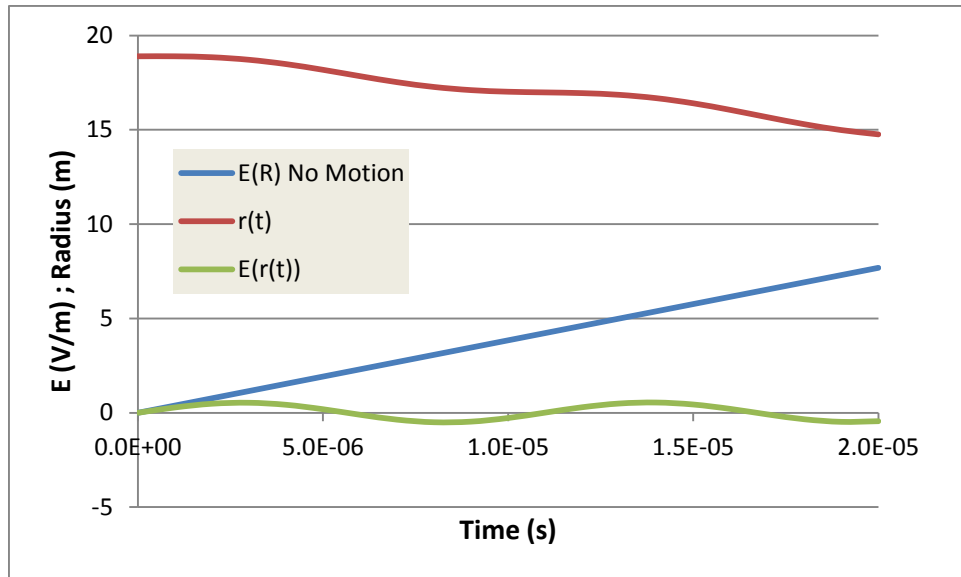


Figure 14. Electric field at sheath with no motion (straight line); Position of outermost particle to reach sheath (upper curve); Electric field seen by said particle (lower curve).

When electron motion is constrained by a weak magnetic field, the presheath electric fields needed to fill the contracting sheath will be somewhat greater than those calculated in this spherical example and the local current densities will be significantly higher. Also, the volume from which electrons must be drawn to fill the sheath will be of greater extent. As the electron paths will be longer, electron scattering by plasma waves may be a significant loss mechanism. Sheath filling in the presence of magnetic field is worthy of further study.

5. VECTOR POTENTIAL ABOUT DSX DURING TRANSMISSION

We computed the vector potential, its time derivative, and the magnetic field generated by charged particle currents, along with the resulting Poynting vector, for the 10 kV, 10^8 m^{-3} , 1 eV simulation with the magnetic field normal to the antenna (0, 0, 5×10^{-6} T). The vector potential, magnetic field, and Poynting vector result from the transverse surface currents, volume ion currents, and volume electron currents. Figure 15 through Figure 20 are for the point in time during the cycle when both booms have a potential near -580 V, and all show values on the Z = 0 plane. Figure 15 through Figure 17 show the total from all three sources of current, followed by Figure 18 through Figure 20 showing the contributions of the individual sources of current.

At this plasma density, the propagating electromagnetic field is mostly due to the transverse surface currents with a significant contribution from the volume electron currents. At higher densities, the volume current contribution would be much larger.

Similarly, at this low plasma density there is little energy in the propagating electromagnetic field. However, at higher densities the energy transmitted may be higher.

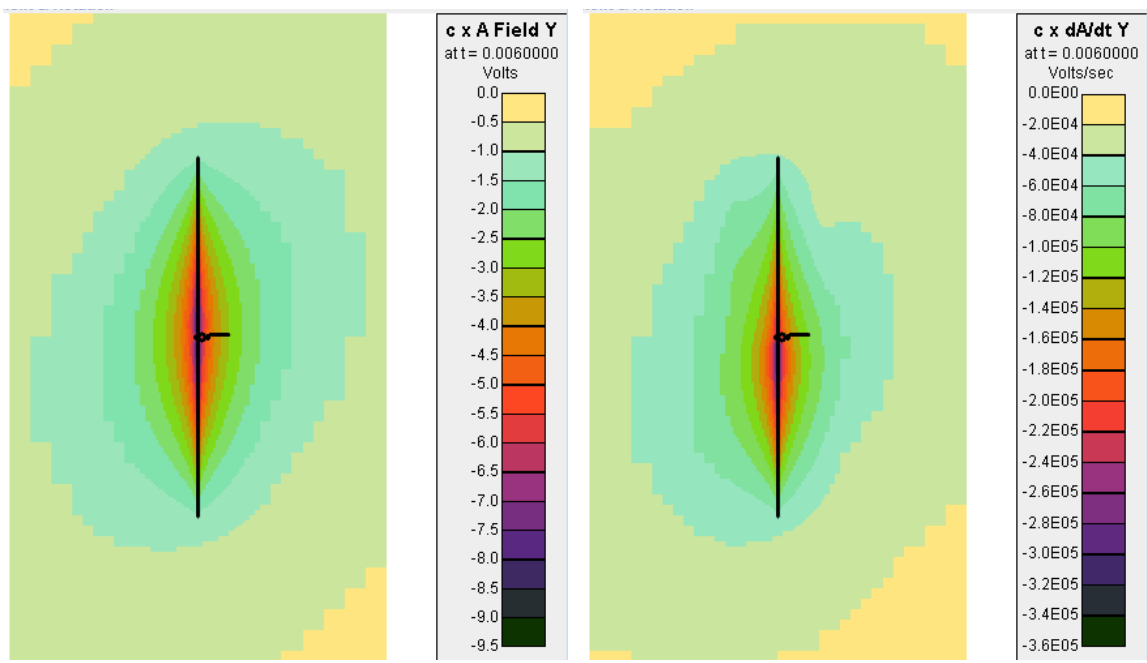


Figure 15. Component along the antenna of the vector potential (V) and rate of change of the vector potential (V/s).

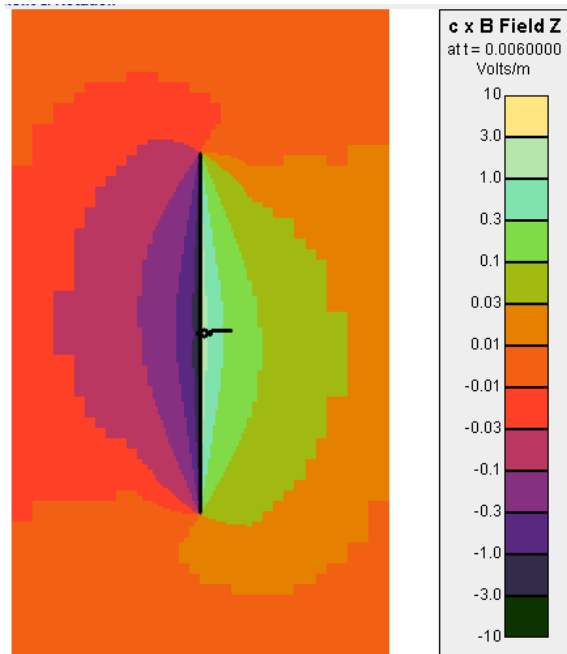


Figure 16. Magnetic field (V/m) normal to the antenna.

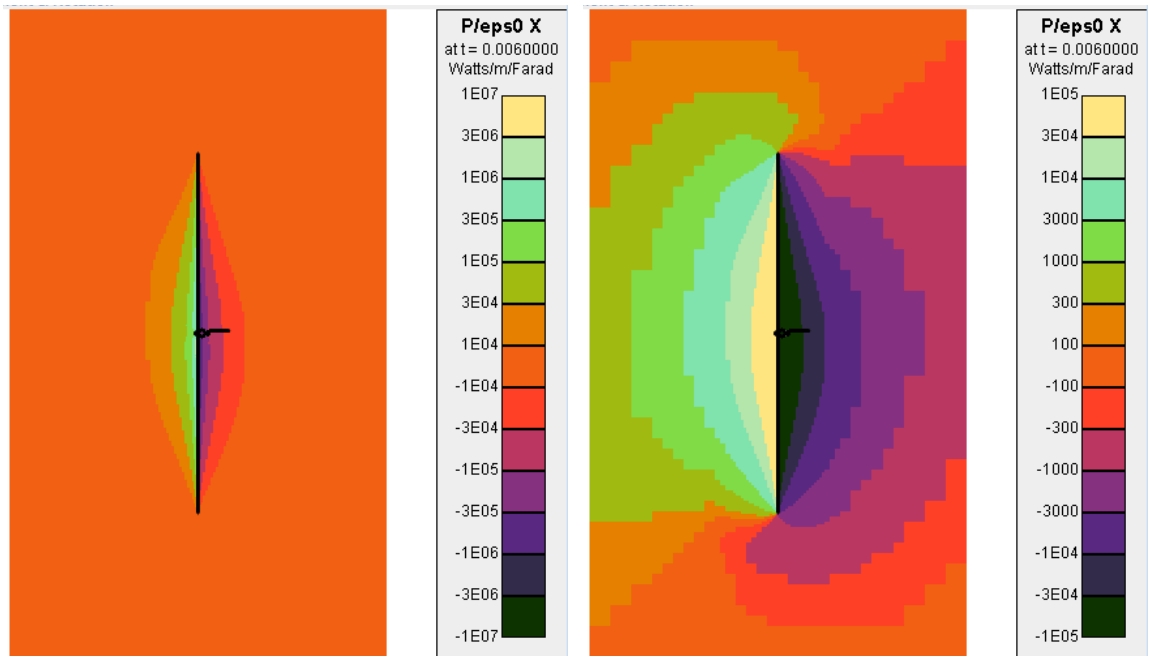


Figure 17. X component of the Poynting Vector (W/m/F).

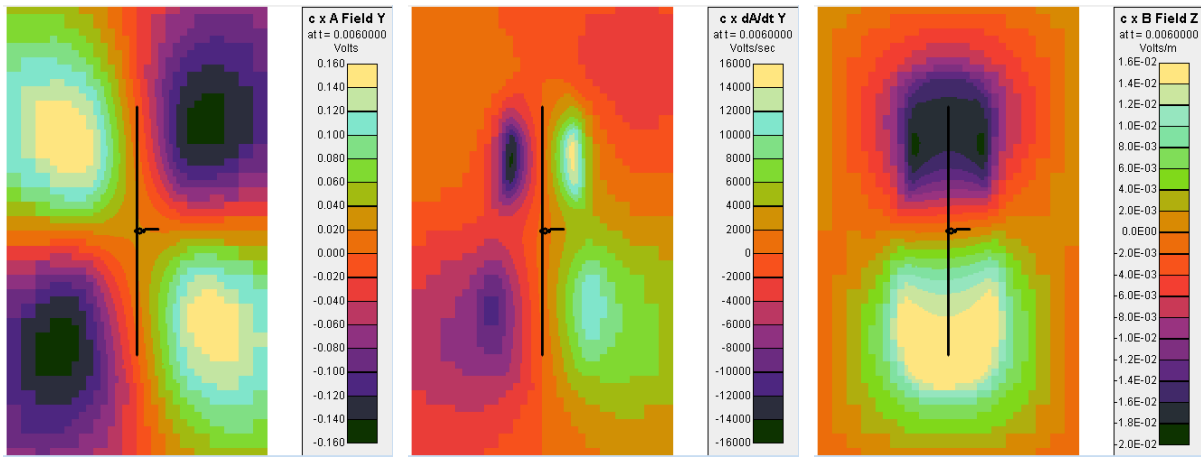


Figure 18. Contribution of volume electron currents to the vector potential, its rate of change and the magnetic field.

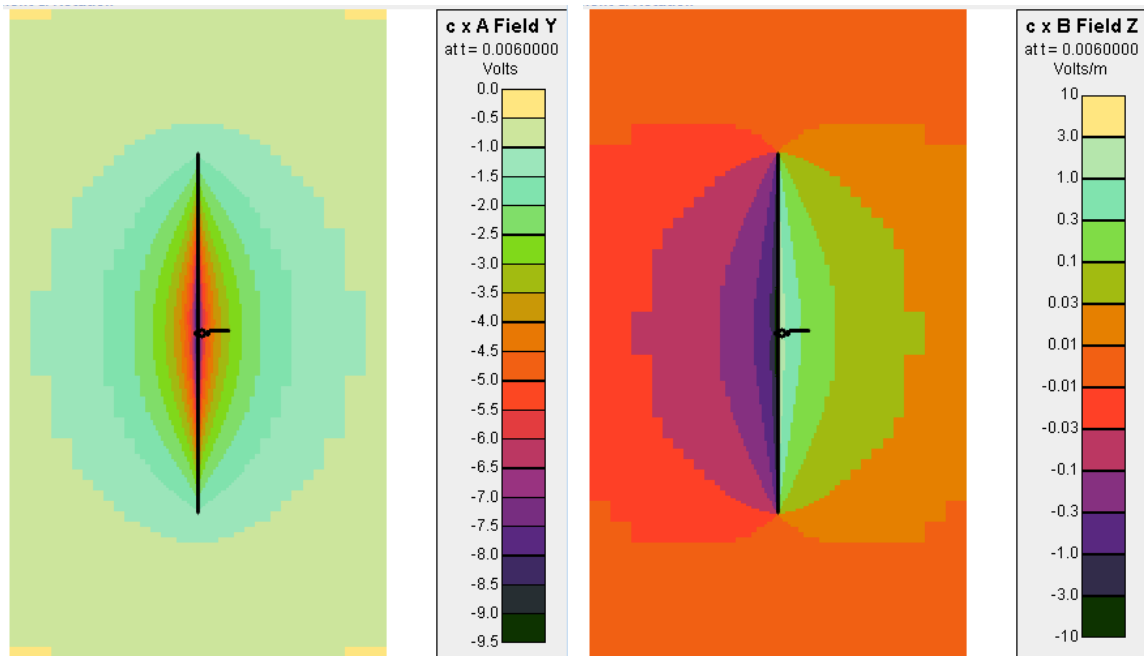


Figure 19. Contribution of transverse surface currents to the vector potential and the magnetic field.

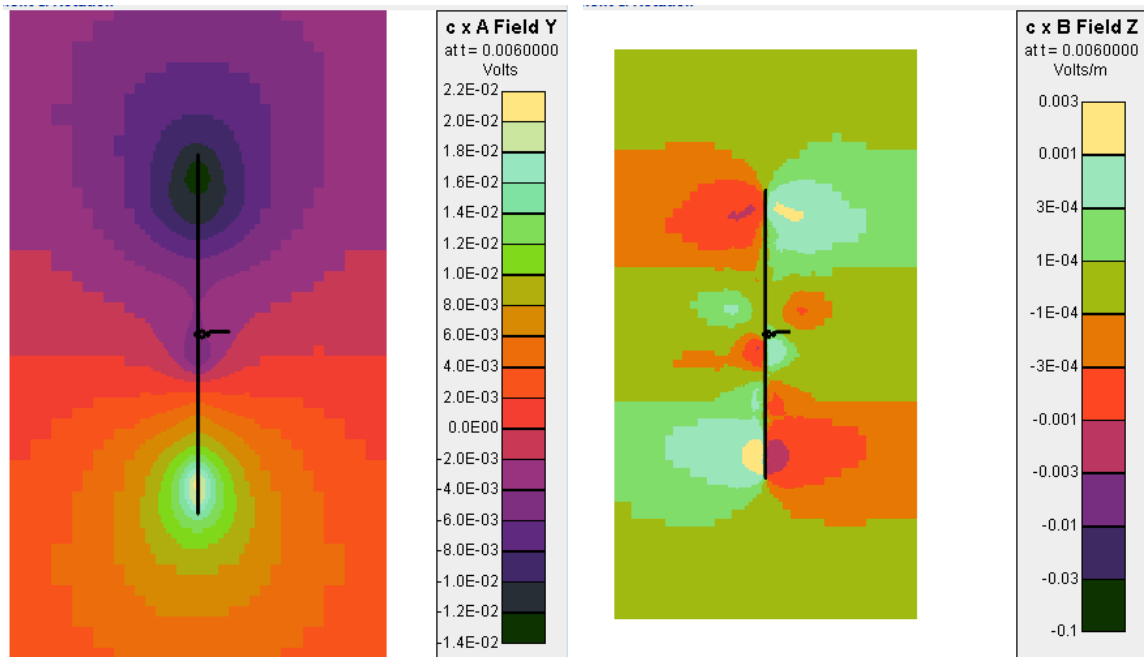


Figure 20. Contribution of the volume ion currents to the vector potential and the magnetic field.

6. ADVANCED EHF-2 ANALYSIS

6.1. Spacecraft and Sensor Tower *Object ToolKit* models

Advanced EHF-2 is a geosynchronous, three-axis stabilized spacecraft. The spacecraft is shown in Figure 21. The *Object ToolKit* model constructed is shown in Figure 22.

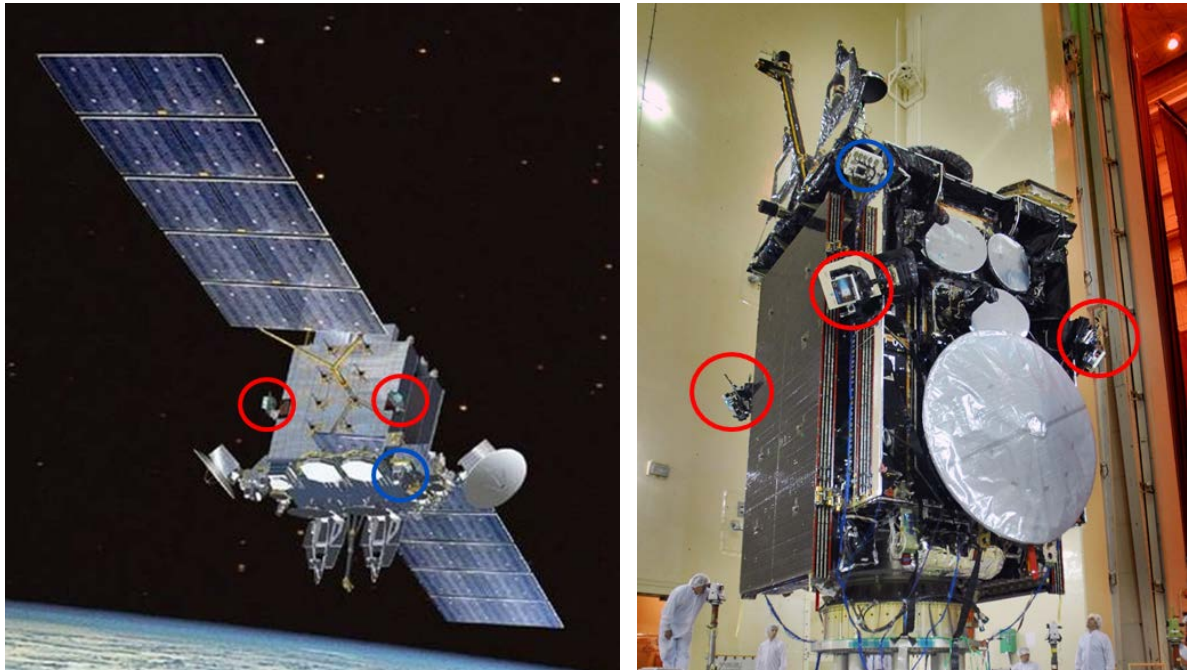


Figure 21. Artist rendition of spacecraft in orbit (left) and photograph during assembly (right). The thrusters are circled in red and the AFRL Sensor Tower is circled in blue.

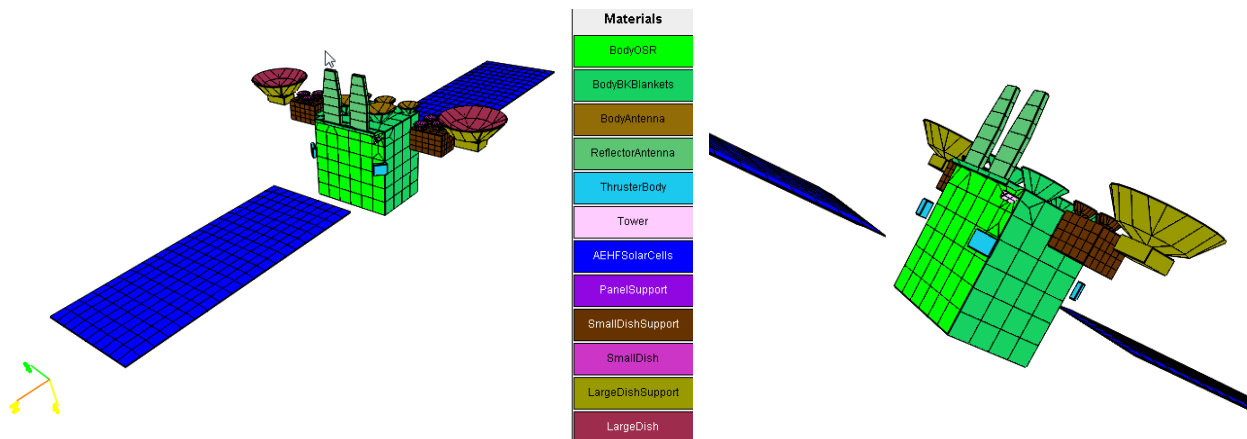


Figure 22. *Object ToolKit* model of Advanced EHF-2 spacecraft viewed from two directions. The minimal resolution AFRL Sensor Tower model is the white triangular shape near the top edge of the spacecraft in the center of the right hand figure.

The instruments of interest on the AFRL Sensor Tower are the two RPAs, the three Flux Probes, the two Planar Langmuir Electron Probes, and the two Charge Sensors. The detailed *Object Toolkit* model is shown in Figure 23. Each RPA, Flux Probe, and Planar Electron Langmuir Probe is assigned its own conductor number to simplify assigning surface potentials and recording the current to each sensor. Each RPA and Flux Probe is also defined as a detector, so that *Nascap-2k* can be used to compute the collected current using the reverse trajectory technique.

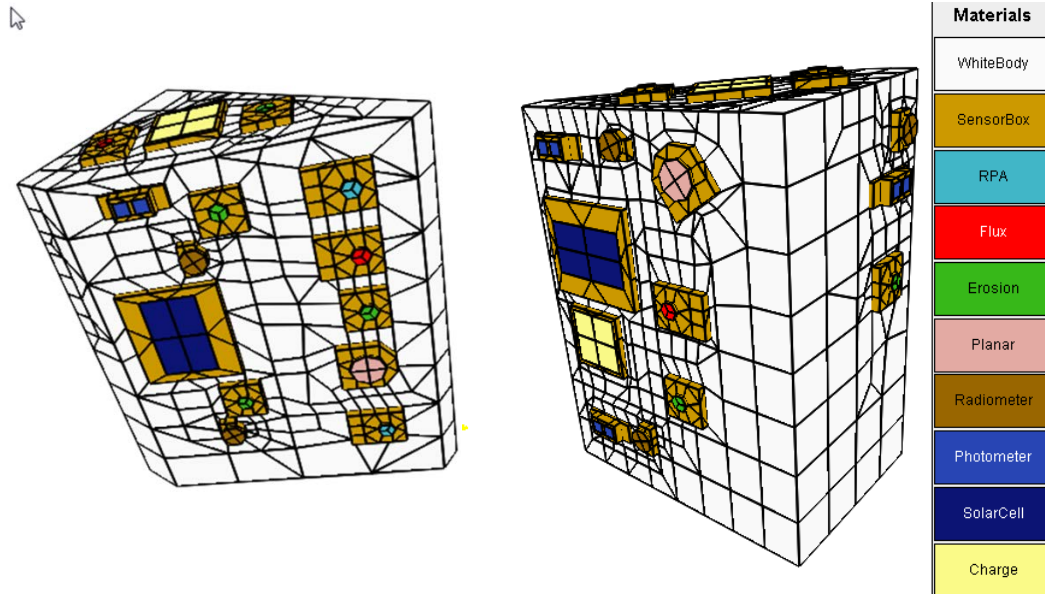


Figure 23. *Object Toolkit* model of AFRL Sensor Tower showing assigned materials.

6.2. Thruster Charge Exchange Plume

The COLISEUM plume definition file that AFRL provided to SAIC is a 1.6 GB file in Tecplot format. Space is divided into 64 zones, each composed of a rectangular $51 \times 51 \times 61$ grid. The plume model covers the volume of space extending 0.5m from the plume axis in the X and Y directions and from 0.2 m behind the exit plane to 1 m in front of the exit plane in the Z direction.

A Java program was written to read the relevant data and construct an XML file in the *PlumeTool* format. Specifically the Java program:

- Read the neutral, single ion, and double ion densities and the single and double ion velocities from the files,
- Placed the data into a $201 \times 201 \times 241$ rectangular grid,
- Combined the single and double ion values at each grid point into a single density and velocity pair with the correct current,
- Azimuthally averaged the data at points (R,θ) to obtain an axisymmetric plume,
- Inserted the data into an XML file in the *PlumeTool* format.

The azimuthal average was done with all available points. The R of $R-\Theta$ is the distance from the center of the thruster orifice. The density associated with points outside the COLISEUM grid was taken to vary as $1/R^2$, and the velocity was taken to be constant with R ($R-\Theta$). Behind the thruster exit plane, the primary beam flux is taken to be zero. The *PlumeTool* formatted file was then read and used by *Nascap-2k*.

The plume ion and neutral densities are shown in Figure 24. The center of the left face of the 0.15 meter box is at $(0, 0, 0)$ in the coordinate system of the original COLISEUM file. The neutral density is un-ionized Xenon. In the following *Nascap-2k* calculations of charge exchange ion densities and fluxes, the plume from COLISEUM is assumed to consist of only primary beam and scattered ions. For present purposes this is believed to be adequate, as the charge exchange rate is proportional to the flux and the primary beam contributes most of the flux. Figure 25 shows the charge exchange ion density and volume potential computed self-consistently from the ion and neutral densities shown in Figure 24. In this calculation, the charge exchange ion temperature is taken to be 2 eV, and the reference plasma density is taken to be 10^{12} m^{-3} .

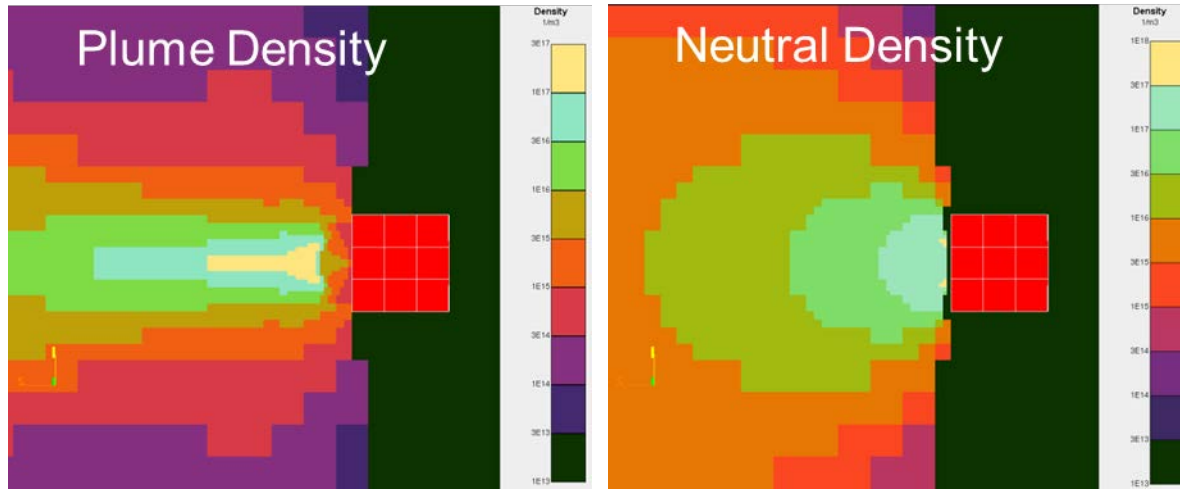


Figure 24. COLISEUM plume ion and neutral densities shown in *Nascap-2k*.

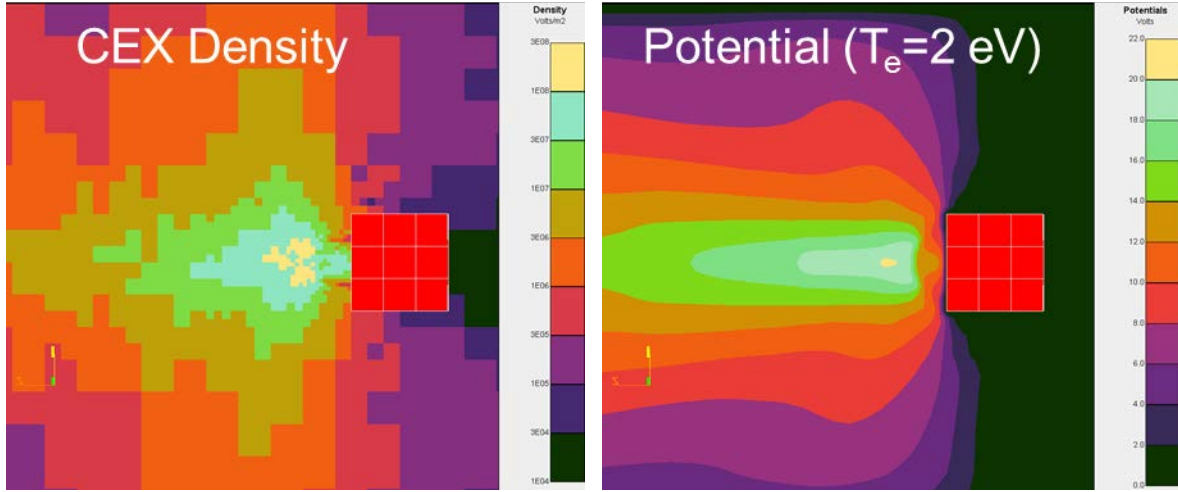


Figure 25. Charge exchange ion density and volume potential as computed by *Nascap-2k* from the plume ion and neutral densities shown in Figure 24.

The thrusters are located on the corners of the Advanced EHF-2 spacecraft as shown in Figure 21. At the beginning of the mission they were used for final orbit raising and positioning and will be used for north-south station keeping during the rest of the mission. Figure 26 shows the plume main beam ion and neutral densities from four thrusters on the spacecraft computed using the COLISEUM-derived plume. *Nascap-2k* allows the user to specify the location and orientation of each thruster. Once placed, each thruster can be specified as either on or off. Figure 26 shows the ion and neutral densities with four thrusters operating.

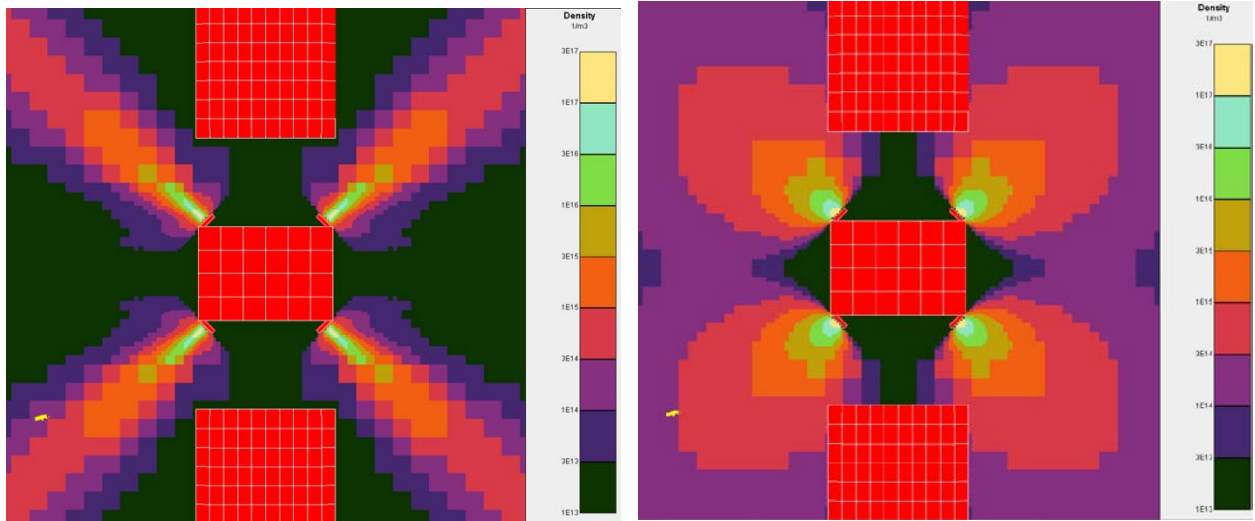


Figure 26. Plume ion and neutral densities for four thrusters operating.

Figure 27 shows the *Nascap-2k* computed self-consistent charge exchange densities and volume potentials. With four thrusters operating, 0.94 A of charge exchange ions are generated. The reference plasma density of 10^{12} m^{-3} was set to be consistent with the COLISEUM computed peak charge exchange ion energies near 40 eV. The low energy ion temperature was set to 4 eV as observed in Reference 3. Of the charge exchange ions, 0.15 A return to the thruster plates,

0.19 A reach other spacecraft surfaces, 0.7 mA reach the AFRL Sensor Tower, and 0.6 A leave the computational space. The density near the spacecraft is of the order 10^{13} m^{-3} .

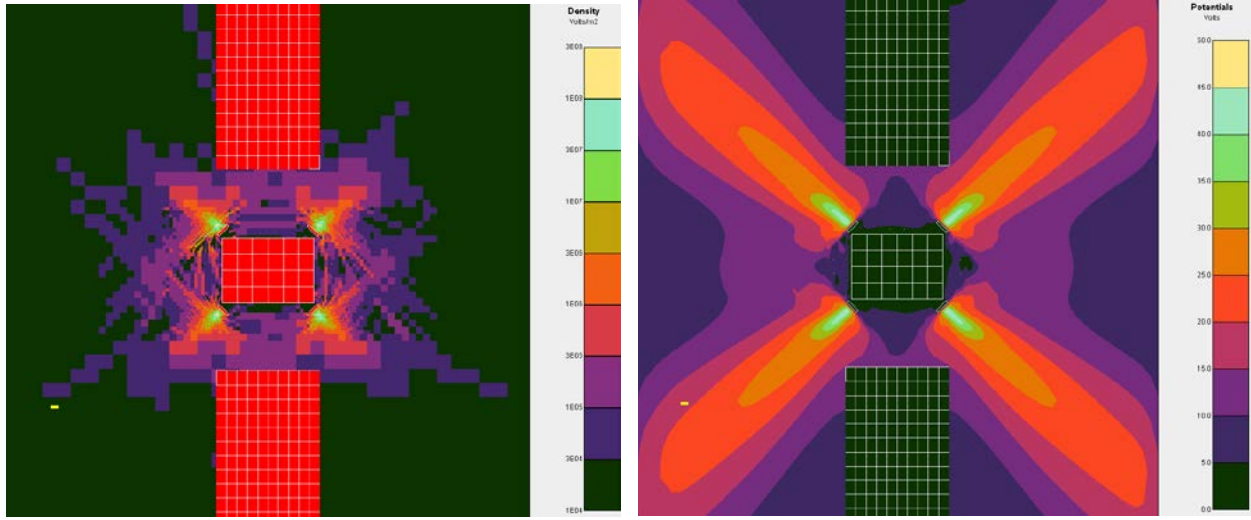


Figure 27. Charge exchange ion density and volume potentials as computed by *Nascap-2k* from the plume ion and neutral densities shown in Figure 26.

As part of this effort, it was necessary to add to *Nascap-2k* the ability to read the neutral density as a function of position from the *PlumeTool* formatted file using the same grid as for the high energy ions.

6.3. Tower Sensors

6.3.1. Space Weather Diagnostics

The sensitivities of the instruments of the AFRL Sensor Tower were determined and compared with the quiescent and disturbed geosynchronous environment currents. As the instruments were included primarily to measure properties of charge exchange ions of the thruster plume, their sensitivity is not optimized for the geosynchronous environment. The highest retarding potential is +300 V on the RPAs, thus the kilovolt electrons and ions of disturbed environments cannot be distinguished from each other. However, their contribution will be included in the total current measurements. To gain a sense of the feasibility of using the AFRL Sensor Tower as a geosynchronous environment diagnostic tool, Table 6 compares the range of typical environment currents with the instrument sensitivities. None of these instruments are likely to respond to the environmental ion flux. It is possible that the RPAs and Flux Probes might be able to make routine measurements of total electron fluxes. As this is not their primary mission, additional calibration and adjustments to the data interpretation algorithms might be needed.

Table 6. Typical geosynchronous currents compared with instrument sensitivities.

	GEO Electron Current	GEO Ion Current	Sensitivity
RPA	1 pA – 0.1 nA	0.03-3 pA	$\pm 100 \text{ nA} \pm 3 \text{ pA}$
Flux Probe	6 pA to 0.6 nA	0.14 pA to 14 pA	$\pm 100 \text{ nA} \pm 3 \text{ pA}$
Planar Electron Langmuir Probe	0.05 nA to 5 nA	1.3 pA to 130 pA	$\pm 1 \text{ mA} \pm 31 \text{ nA}$

As the Charge Sensor was designed to measure magnetospheric electrons, it might provide useful environmental diagnostics. When interpreting the data, it is important to include the effects of the internal instrument capacitance. On longer time scales, the internal circuit acts as a resistive current divider and, therefore, the measured voltage corresponds to the surface potential. On shorter time scales, the internal circuit acts as a capacitive divider, and therefore, the rate of change of the measured voltage corresponds to the plasma current.

6.3.2. Plume Diagnostics

Figure 28 shows the sheath about a biased Planar Electron Langmuir Probe with a thruster operating. The sheath is a few times the probe area, so the current will be enhanced. The current is well within the range of the instrument's sensitivity.

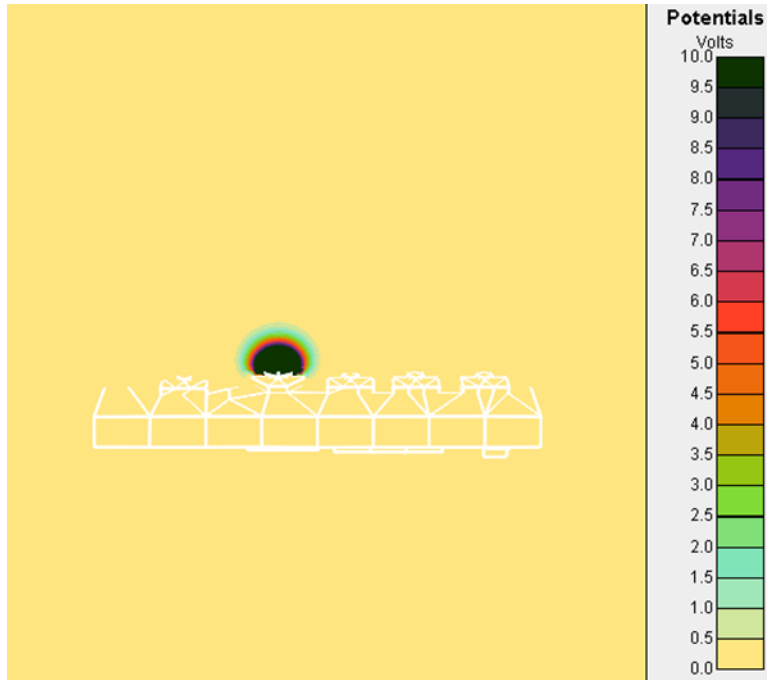


Figure 28. Potentials in a plane through a Planar Electron Langmuir Probe in a 10^{13} m^{-3} , 4 eV plasma with 100 V on the probe.

6.3.3. Ion Steering

The feasibility of testing the viability of shielding sensors from the low energy component of a plasma by biasing nearby surfaces using the AFRL Sensor Tower was explored. A series of calculations was performed to assess the relevant currents.

Figure 29 and Figure 30 show the potentials on a plane through the AFRL Sensor Tower with +100 V on the Planar Electron Langmuir Probes and 0 V on all the other surfaces. The potentials were computed assuming no screening (Laplacian potentials) and a zero potential boundary condition. These potentials provide an upper bound to the extent of the plasma disturbance. The probe potentials shield the nearby RPAs and Flux Probes from low energy ions. Figure 31 shows sample trajectories of low energy ions that reach the RPA nearest the Planar Electron Langmuir Probe in the figure. It is only the lowest energy ions whose trajectories are disturbed.

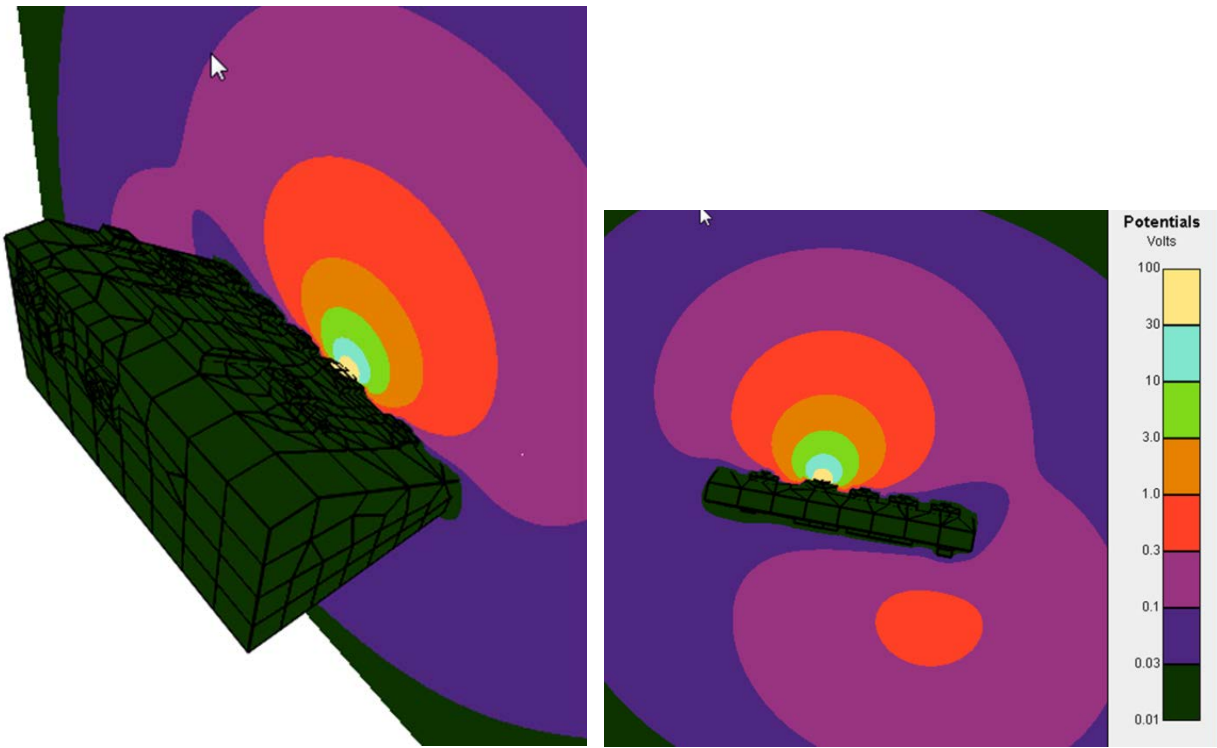


Figure 29. Potentials in a plane through the Sensor Tower with +100 V on the Planar Electron Langmuir Probes.

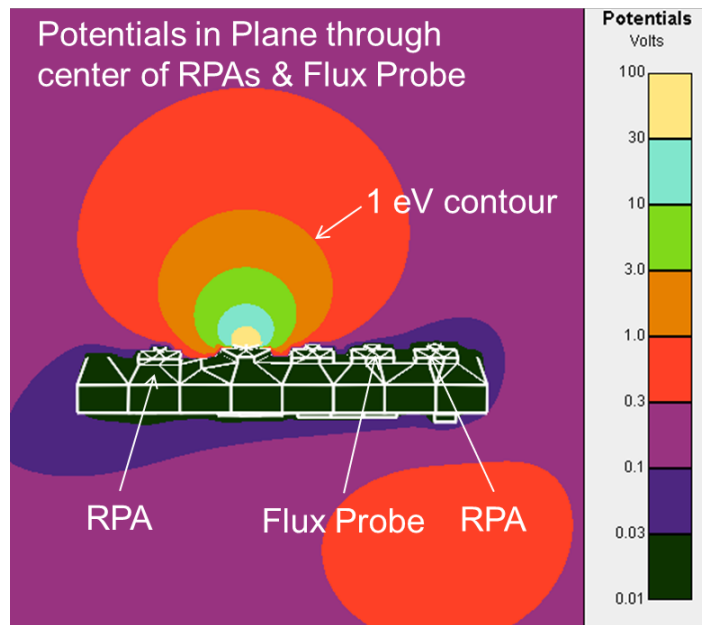


Figure 30. Potentials on a plane through the AFRL Sensor Tower, annotated.

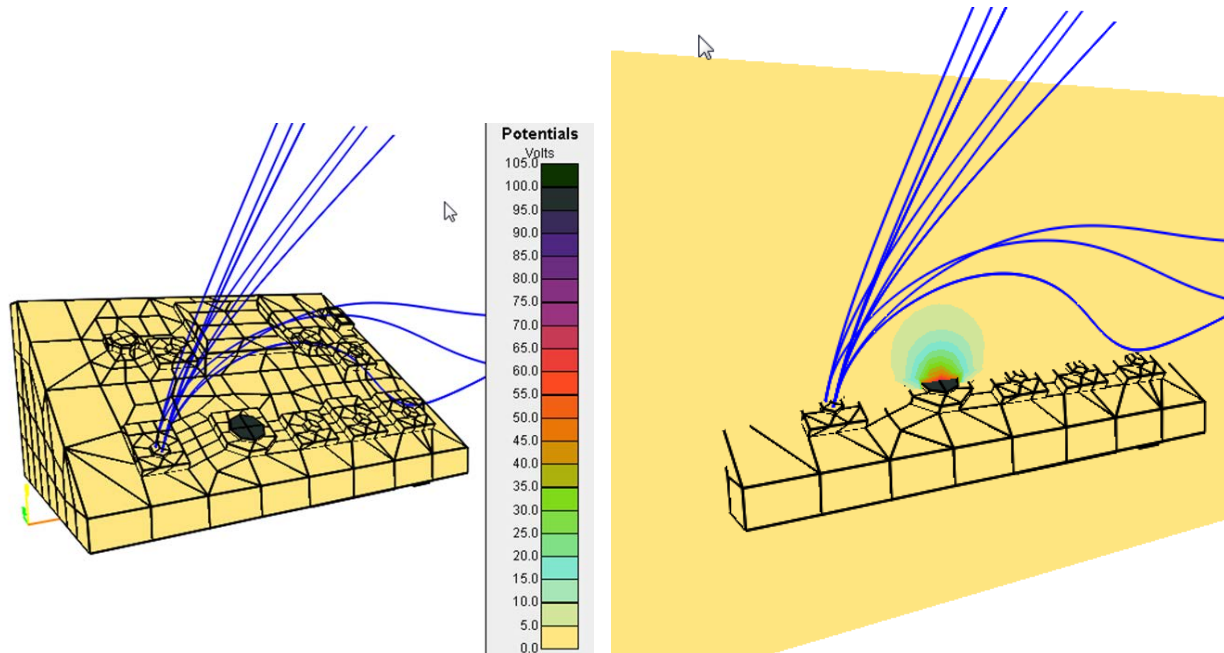


Figure 31. Sample trajectories (blue lines) in potentials shown in previous two figures. The right hand figure also shows the same potentials on a reversed linear scale.

The reverse trajectory technique was used to compute currents to the RPAs and Flux Probes with ± 100 V on the Planar Electron Langmuir Probes and 0 V on all the other surfaces. The goal is to determine to what extent low energy ions are steered away from the detectors. The computed flux of the attracted species to the RPAs and Flux Probes is the same (within 1%) as computed

for 0 V on all surfaces. A reduction of up to 2% in the flux of the repelled species was computed depending on the distance from the nearest biased Planar Electron Langmuir Probe.

Figure 32 shows the relative integrated flux as a function of energy as computed by *Nascap-2k* compared with the analytic solution in the absence of potentials. It is only for ion energies below 1 eV that the computed flux deviates from the analytic result. Thus the only trajectories that are disturbed enough by the Planar Electron Langmuir Probe potential that the particles don't reach the detector are those of charged particles with energy below 1 eV.

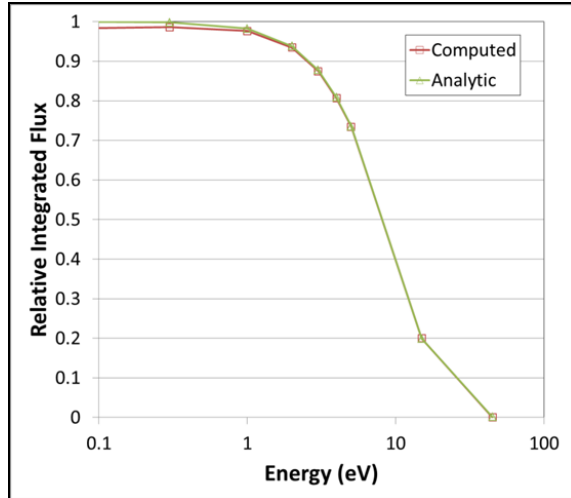


Figure 32. Relative integrated flux as a function of energy as computed by *Nascap-2k* compared with the analytic solution in the absence of potentials.

7. REVIEW OF SEPTEMBER 2001 LANL MPA DATA

As part of the project to determine a set of environment parameters that predict under what environment conditions and by how much surfaces on a spacecraft differentially charge, we reviewed the SAIC 2002 project “Characterization of Magnetospheric Spacecraft Charging Environments Using the LANL Magnetospheric Plasma Analyzer Data Set” as well as the data set used in that study. We used that data set to further examine how temperature and electron flux are correlated with chassis potential and barrier height, which may be a proxy for differential potential. We examined the different ways in which temperature can be defined. We also took a preliminary look at the time dependence of the relevant parameters.

7.1. 2002 Study using LANL Data

In 2002 SAIC was funded by NASA to identify a relatively simple characterization of the full particle distribution that yields as accurate a prediction of the observed charging as the full distribution under a wide variety of conditions. This study is documented in References ⁴ and ⁵. The measurements used in the study were taken by the LANL (Los Alamos National Laboratory) MPA (Magnetospheric Plasma Analyzer). The bulk of that investigation, and all of the recent work, used data taken on the satellite 1994-084 in September 2001 between 22:00 and 2:00 local time. This time period includes the full eclipse period as well as sunlight periods before and after eclipse. The two primary conclusions of the study are the following:

- A simple current balance calculation of chassis potential during the eclipse period using measured spectra, material properties of graphite, and assuming 81% of the secondary electrons escape gives a result within a factor of three of the measured potential 87% of the time.
- Similar results were obtained using a Kappa distribution for the electrons and a Maxwellian for the ions. Other choices of spectral shape give less accurate estimates.

At that time it was noted that adding intelligence to the fitting procedure would be likely to improve the results as poor fits were often obtained when significant low energy plasma is present. Attempts to compute the chassis potential during sunlit periods were much less successful.

7.1.1. Data

The MPA measures electron and ion fluxes in 40 energy channels logarithmically distributed between 1 eV and 47 keV. A three-dimensional distribution is obtained every 86 seconds. The data sets used include the following measured and derived parameters:

- Date and time of measurement.
- Geocentric satellite position, used to determine if the satellite is in sunlight or eclipse.
- Chassis potential and flag to indicate if potential is derived from an ion line or inferred from the electron spectrum.
- Estimated barrier height, used as the lower limit in the electron moment integrals.
- Low energy (up to 124 eV) ion density moment.
- High energy (over 124 eV) ion density moment.

- High energy (over 124 eV) ion perpendicular and parallel temperature moments.
- High energy (over 30 eV) electron density moment.
- High energy (over 30 eV) electron perpendicular and parallel temperature moments.
- Spin averaged ion flux to each of the 40 energy channels.
- Spin averaged electron flux to each of the 40 energy channels.
- Other parameters not used for this calculation.

The method used to derive the estimated barrier height, the moments, and the inferred chassis potential used when it cannot be determined from the ion spectrum are discussed in the sections that follow. Other than where specifically noted, only measurements with a chassis potential determined from an ion line are used in this report.

7.1.2. Potential Computation

In eclipse, the measured fluxes and assumed average material properties can be used to determine the net flux to the spacecraft—which if the measurements and computations are ideal would be zero. Figure 33 shows the measured chassis potential versus the net ion flux, the net electron flux, and their sum. The net ion flux is the sum over all energy channels of the spin averaged ion flux plus the flux of secondary electrons that would be generated by the incident ions at the energy of the energy channel center using the default material properties of Graphite from the *Nascap-2k* computer code. The net electron flux is the sum over all energy channels above an SAIC computed low energy cutoff of the negative of the spin averaged electron flux plus the flux of secondary and backscattered electrons that would be generated by the incident electrons at the energy of the energy channel center. In this figure, the low energy cutoff is the lower of half the chassis potential and the LANL computed barrier height. Figure 34 illustrates the result of using the conjecture of the 2002 study that 19% of the low energy secondary electrons are trapped by spacecharge barriers and return to spacecraft surface.

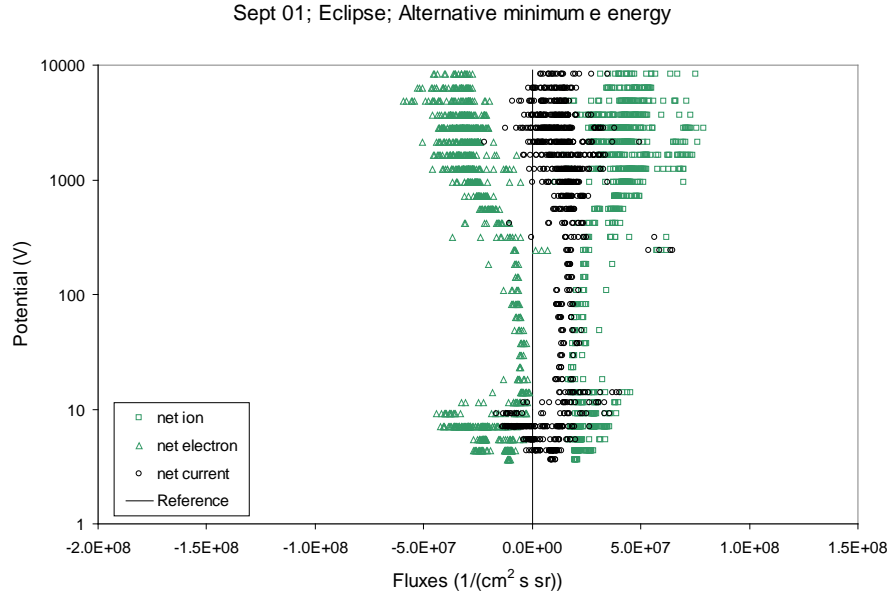


Figure 33. Measured chassis potential versus net flux during the eclipse periods, using SAIC computed low energy cutoff and Graphite material properties.

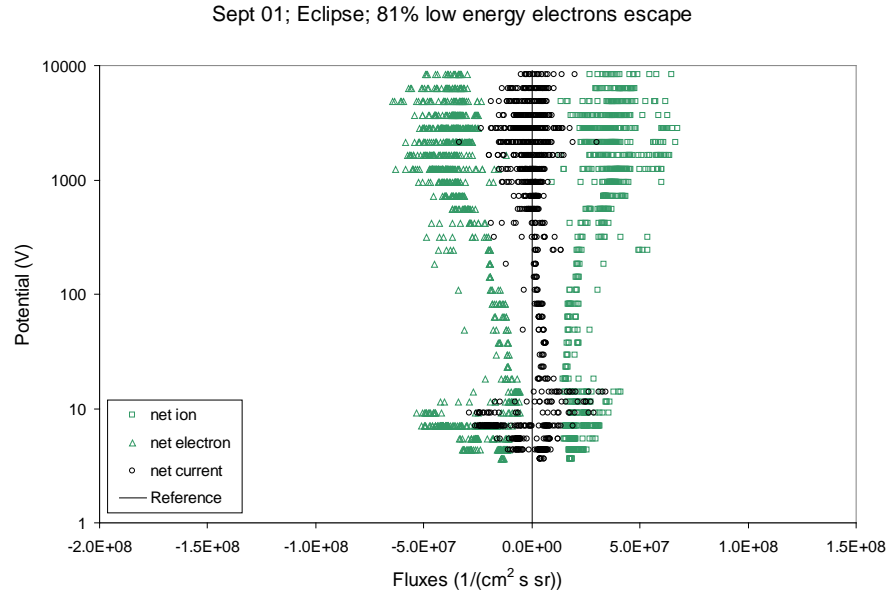


Figure 34. Measured chassis potential versus net flux during the eclipse periods, using SAIC computed low energy cutoff, Graphite material properties, and assuming that 19% of the secondary electrons return to the spacecraft.

The measured fluxes were then used (directly, with no attempt to fit them to a functional form) to compute the potential using the following procedure.

- Given the measured potential, compute the ion and electron spectra at infinity.

2. Using the computed ion and electron spectra at infinity, determine the net current (incident, secondaries, backscattered, and photo) to the spacecraft for a proposed chassis potential.
3. Search for a unique chassis potential at which the net current is zero. If there is no such potential, search for the chassis potential at which the net current has the minimum value. This is the computed chassis potential.

The measured potential versus the computed potential is shown in Figure 35. 65% of the points have a solution within a factor of 1.5, 87% of the points have a solution within a factor of 3, and for 8% a solution could not be found. Almost all of the points for which no solution can be found have a potential below 30 V.

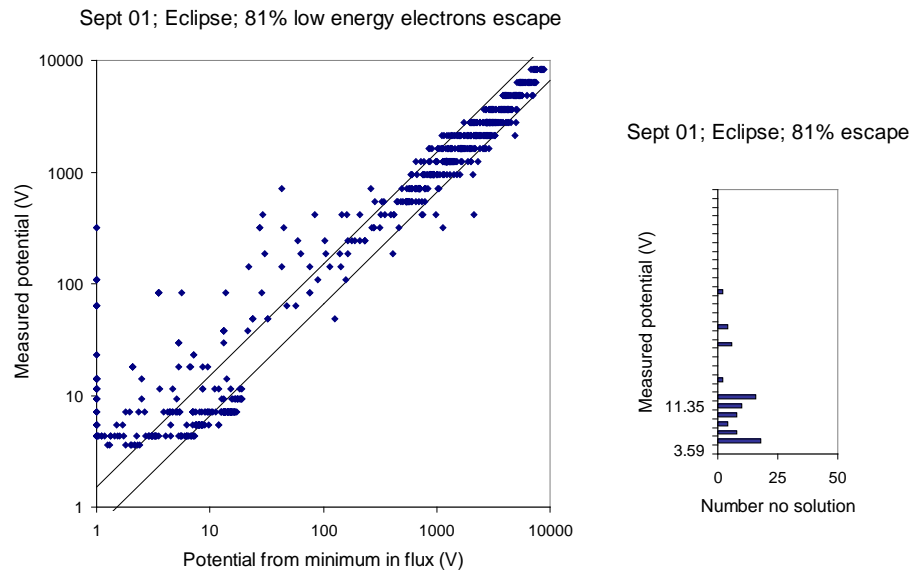


Figure 35. For eclipse periods, measured chassis potential versus potential computed from minimum in the net flux with measured fluxes adjusted for the proposed potential. Lines are a factor of 1.5 above and below the diagonal. Bars in the right hand graph show the number of measurements for which no solution was found.

7.1.3. Alternative Predictors

In evaluating our ability to predict potential from the measured spectra, we compared the above current balance approach with some alternatives.

M.F. Thomsen⁶ has observed a power law relationship between the “average electron temperature” and the chassis potential. For this relationship, a term to account for the cold electron population is added to the electron temperature moment. The electron temperature moment of the spectrum below 30 eV is assumed to be approximately 5 eV and the cold electron density is represented by the cold ion density.

$$\langle \theta \rangle = \frac{n_e \times \theta_e + n_{lp} \times 5 \text{ eV}}{n_e + n_{lp}} \quad (1)$$

where n_e and θ_e are electron density and temperature moments for energies above the maximum of 30 eV and the barrier estimate, and n_{lp} is the ion density moment for energies below 124 eV. Separate power law fits were developed for eclipse and sunlit conditions and for each satellite. For 1994-084 in eclipse

$$\phi = 1.74 \times 10^{-5} \langle \theta \rangle^{2.26} \quad (2)$$

Figure 36 shows this relationship for this dataset.

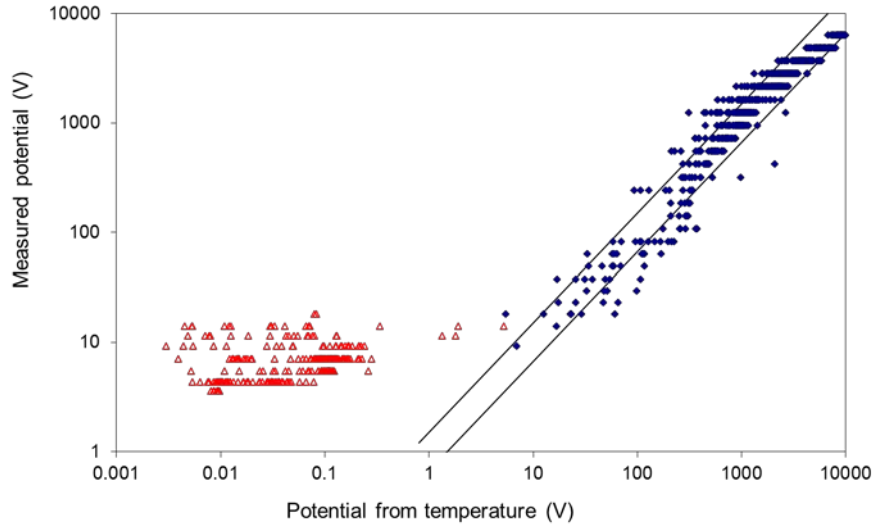
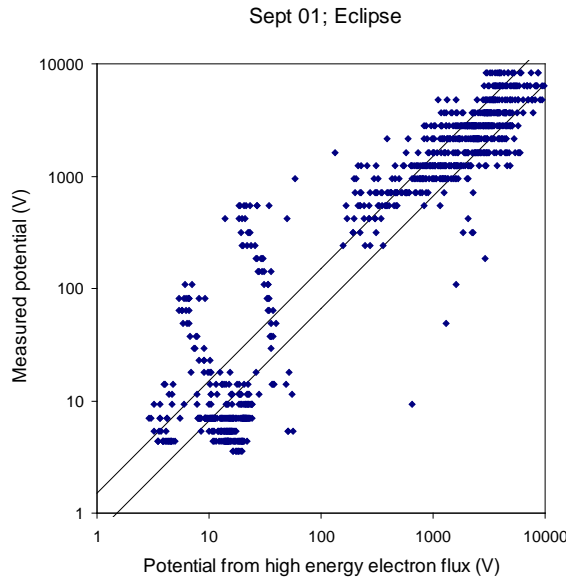


Figure 36. Measured chassis potential versus potential computed from Equation 2 for the eclipse periods. Lines are a factor of 1.5 above and below the diagonal. Triangles represent plasma with a lower energy density. (See Davis, et al, 2003.)⁵

We also examined the incident electron flux in the higher energy channels as possible predictors of the potential. The best predictor for the September 2001, eclipse dataset is the sum of the energy channels from 9123 V and above using the following relation

$$\phi_{\text{estimated}} = 1.359 \times 10^{-12} \left(\sum_{E>9123} (\text{measured flux} \times \text{bin width}) \right)^{2.03} \quad (3)$$



**Figure 37. Measured chassis potential versus potential computed using Equation 3 for the eclipse periods.
Lines are a factor of 1.5 above and below the diagonal.**

All approaches give accurate values for high potentials. The average temperature gives the best predictions in the mid-range and current balance gives the best results at low potentials.

7.1.4. Functional Form

The choice of spectral shapes that gives the most accurate chassis potential estimates is a Kappa distribution for the electrons and a Maxwellian for the ions. Figure 38 shows the measured potential versus the potential from the minimum in the total flux using fluxes from automated fits to these spectral shapes. The reason for the cluster of points in the center bottom of the graph is that the automated fitting of the low temperature ion spectrum often gives a high temperature Maxwellian, thus underestimating the low energy ion current that quenches any negative potential. Adding intelligence to the fitting procedure might improve the results.

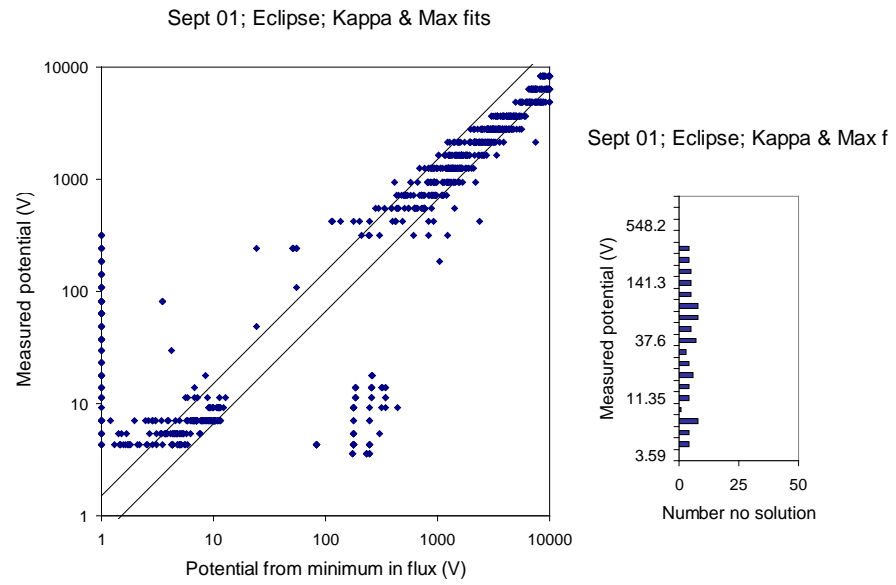


Figure 38. Measured chassis potential versus potential computed from the minimum in the net flux, where the fluxes are computed from a Kappa fit to the measured electron spectrum and a Maxwellian fit to the measured ion spectrum for the eclipse periods.

7.1.5. Sunlit Periods

The current balance potential estimate algorithm was also applied to the measurements when the spacecraft was in sunlight, with less success. A graph of the best results is shown in Figure 39. The difficulty of estimating photoemission and the importance of the prior state make this simplistic potential estimate less accurate when the spacecraft is in sunlight.

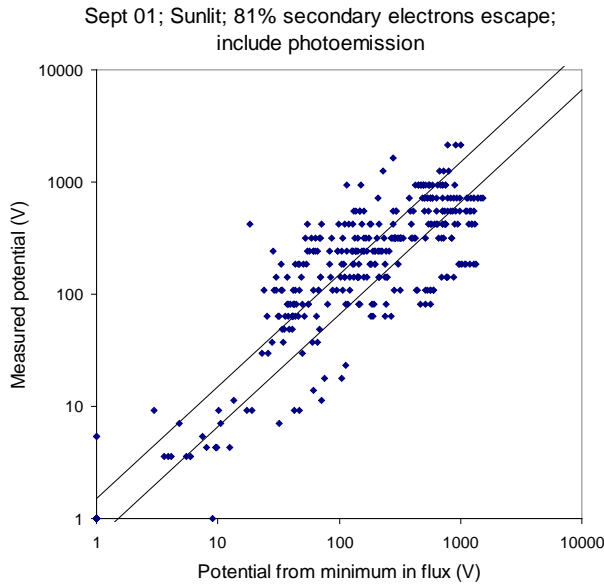


Figure 39. Measured chassis potential versus potential computed from the minimum in the net flux, when the spacecraft is in sunlight assuming 81% of the secondary electrons escape, and including an estimate of the photoemission. There are two measurements for which no solution was found.

7.2. Spectra

We reexamined the dataset used in the 2002 study in light of the goal of developing a differential charging index. Figure 40 shows every tenth electron spectrum measured between 22.2 and 1.8 local time on day 255. These include spectra for which a measured chassis potential is not available. The differential flux is graphed versus the energy channel number. The energy channels are logarithmically spaced and ordered from highest to lowest incident particle energy, so the low energy channels are on the right. The line graph on the right of the figure shows the chassis potential during this period. The earliest five spectra are from before eclipse, when the chassis is between -100 V and -300 V. The next five shown were taken during the eclipse period when the chassis is between -550 V and -30 V. The final set of spectra was taken after the eclipse period, when the spacecraft was essentially uncharged with a chassis potential between 0 and -30 V. All the spectra have elevated count rates in the low energy channels. This is due to spacecraft generated photo and secondary electrons that are trapped by the differential potential. The enhancement is most dramatic in the sunlit spectra. If the low energy count rate exceeds a threshold, the energy at the geometric center of the energy channel between 30 eV and 400 eV with the minimum count rate is defined to be “the barrier.”⁶ The energy at the upper limit of the energy channel is used as the lower limit of electron density and temperature moment integrals. If there is no minimum or if the count rate of the low energy channels is below a specified rate,

the barrier is set at 34 V. In the spectra shown, Series 20 has a 78 V barrier. Each of the other spectra has a 34 V barrier, either because it doesn't have a clear minimum between 30 and 400 eV, or because the flux to the low energy channels is below the threshold.

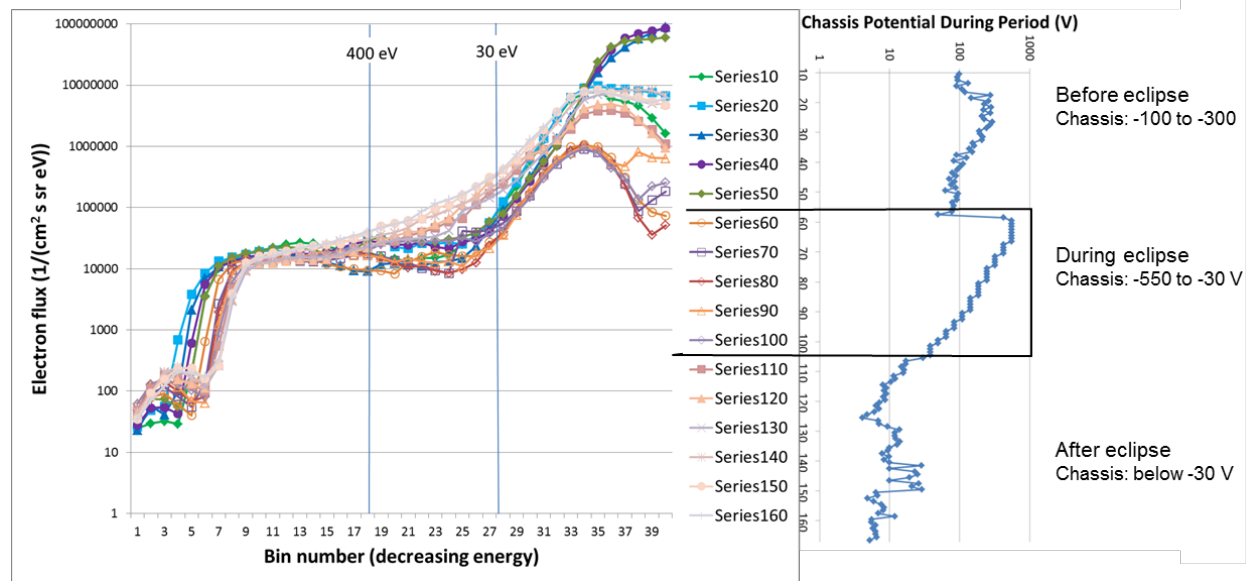


Figure 40. Differential electron spectra between 22.2 and 1.8 local time on day 255. The right hand graph augments the legend by indicating the measured or inferred chassis potential and the eclipse period during this time.

7.3. Temperature

Temperature is a well-defined quantity only for a Maxwellian plasma. At geosynchronous altitudes, the plasma is tenuous enough that it is not at equilibrium and not Maxwellian. Three definitions are discussed here:

- Temperature moment as published by LANL,
- $$T_{he} = 2\pi \frac{2}{3n} \sqrt{\frac{2m}{e}} \sum_{E > \max(30, E_{\text{barrier}})} \left(\frac{F(E)}{E} \sqrt{E \mp \phi_m}^3 \Delta E \right).$$
- Average temperature as defined by M. Thomsen⁶ and given in Equation 1.
 - Temperature parameter of a Maxwellian fit to the measured spectrum.

The temperature moment as published by LANL excludes low energy channels that may be contaminated by trapped electrons. Thus it never has a value under 100 eV, even for low energy plasma. It also loses accuracy at high temperatures and on highly charged spacecraft, as the top energy of the highest energy channel is 47 keV. Additionally, it requires an accurate measure of the chassis potential.

As discussed in Section 7.1.3, to provide a better measure of lower energy plasmas, M. Thomsen created an “average temperature.” The contribution of the lower energy range of the electron spectrum is represented by the density of ions up to 124 eV and a temperature of 5 eV. The average temperature has a high correlation with the chassis potential, as expressed by Equation 2.

The average temperature and the chassis potential are iteratively computed to self-consistency in order to provide the published inferred chassis potential and resulting density and temperature moments.

Figure 41 shows the role of the two terms of the average temperature. The red triangles are the first (high energy) term of the average temperature versus the average temperature. The blue diamonds are the temperature moment versus the average temperature. At high temperatures, the average temperature reduces to the temperature moment (T_{he}). At the other end, it is only below about 30 eV that the 5 eV low energy “temperature” contributes. Assuming a value somewhat higher or lower than 5 eV would give almost the same result.

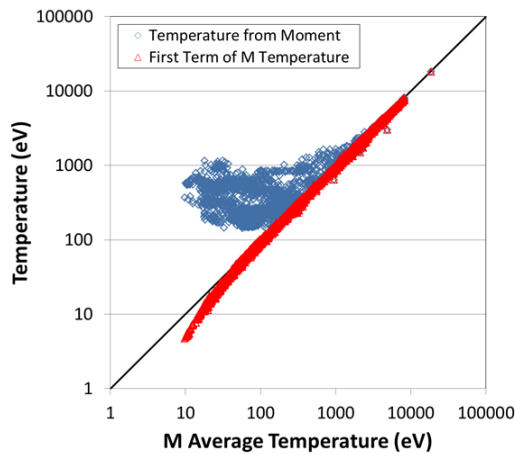


Figure 41. Relationship between the electron temperature moment and the average temperature. Data includes points with both measured and inferred chassis potentials.

Figure 36 shows the measured chassis potential versus the potential computed from the average temperature and Figure 42 shows the measured chassis potential versus the potential computed from the electron temperature moment using the same relationship. Below about 200 V, the temperature moment significantly overestimates the chassis potential, while the average temperature provides a reasonable estimate of the potential for values over 30 eV.

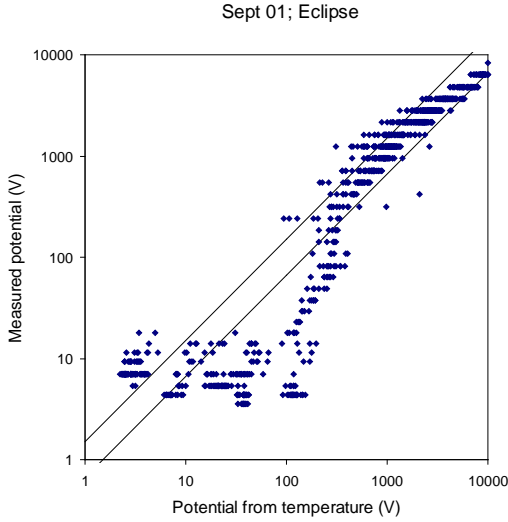


Figure 42. Measured chassis potential versus potential computed from Equation 2, with the electron temperature moment used instead of the average temperature for the eclipse periods. Lines are a factor of 1.5 above and below the diagonal.

The final useful definition of temperature is the temperature parameter of a Maxwellian fit to the measured flux spectrum. The Maxwellian fit can be determined either by taking the best fit straight line through the logarithm of the flux versus the energy or by non-linear least squares fitting of the flux versus the energy. The first procedure weights the higher energies more because the low high energy fluxes carry little weight when fit directly.

Figure 43 and Figure 44 compare the temperature fitting parameter with the electron temperature moment. The green triangles are the temperature parameter from the fit versus the temperature moment computed from the measured fluxes. At the highest temperatures, the different definitions give similar values. The temperature parameter of the linear fit to the logarithm of the flux is several times higher than the temperature moment for moments under 1000 eV. This is a reflection of the non-Maxwellian tail of the distribution function. A fitting procedure that focuses on the high energy portion of the spectrum completely misses the low energy structure. The alternative fitting procedure, which gives equal weighting to the lower energy measurements and the higher energy measurements, gives a somewhat better correspondence, although the fit temperature still differs from the moment by factors of 3 to 10 for many spectra.

The two primary contributors to the difference between the fit parameters and the moments computed directly from the measured fluxes are the method used to compute the moment and differences between the fit and the original fluxes. The blue diamonds in the figures illustrate the role of the first factor. For these points, the temperature moment is computed from the fluxes of the Maxwellian fit using the same energy channels as the moment derived from the measured fluxes. If the moment integral were perfect, the temperature moment computed in this way would give the temperature parameter of the fit. For most spectra, the temperature moment computed from the fit is greater than the fit temperature parameter as it is primarily the low energy channels that are missing. The fact that the moment is computed by summing over finite width energy channels contributes to the error.

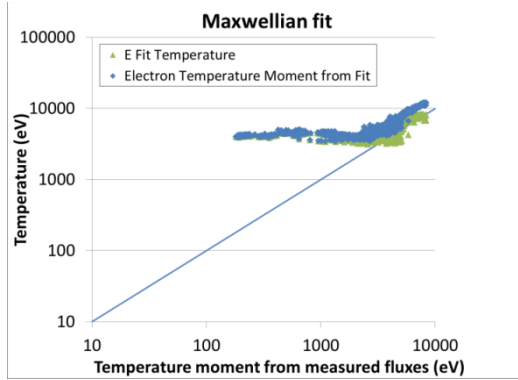


Figure 43. Relationship between the temperature parameter of a Maxwellian fit (using a linear fit to the logarithm of the flux versus the energy) and the temperature moment.

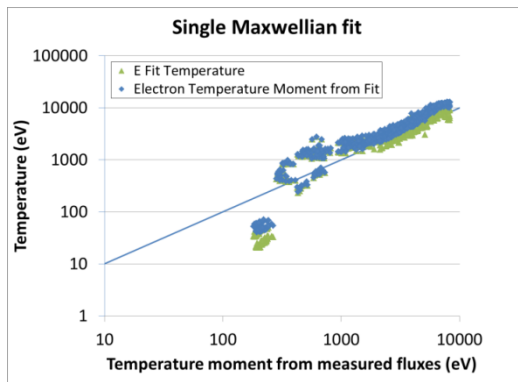


Figure 44. Relationship between the temperature parameter of a Maxwellian fit (using linear least square fitting) and the temperature moment.

As can be seen in Figure 45, the temperature parameter of the fit also does not correspond to the average temperature. Figure 46 shows that by itself the temperature parameter of the fit also does not provide a good estimate of the potential. Chassis potentials over a couple of orders of magnitude correspond to the same temperature parameter.

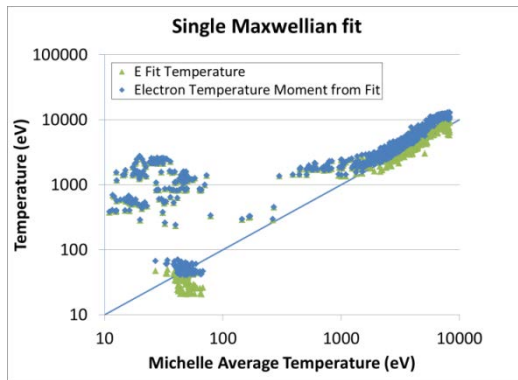


Figure 45. Relationship between the temperature parameter of a Maxwellian fit (using linear least square fittings) and the average temperature.

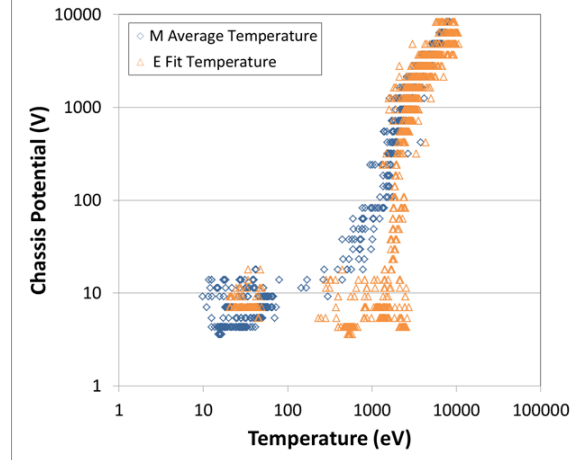


Figure 46. Measured chassis potential versus the average temperature and the temperature parameter of the fit.

It is clear from these results that there is no reason to believe that any of the temperature moment values are appropriate to use in a *Nascap-2k* calculation.

7.4. Incident Electron Flux

The other quantity that has been suggested as a predictor of spacecraft surface potentials is the incident electron flux. In the following we explore the viability of three suggested measures.

We first consider the integral electron flux above the barrier energy. The points in Figure 47 (eclipse charging) and Figure 48 (sunlight charging) show the chassis potential versus the electron integral flux in the ambient plasma. A correlation between incident integral flux and chassis potential and possibly a minimum flux needed before the chassis exceeds about 20 V can be seen. The low number of measurements with potentials in the range of 20 V to 100 V make it impossible to draw any firm conclusions about the value of the minimum flux threshold. Two significant sources of error are the inherent uncertainty in the correction for the chassis potential and the absence of the low energy channels. These figures also show that a given flux generally produces a lower potential in sunlight than does the same flux in eclipse—as the photoelectron flux reduces the potential. Figure 48 separates measurements made before the eclipse period from those made after. There is no obvious difference.

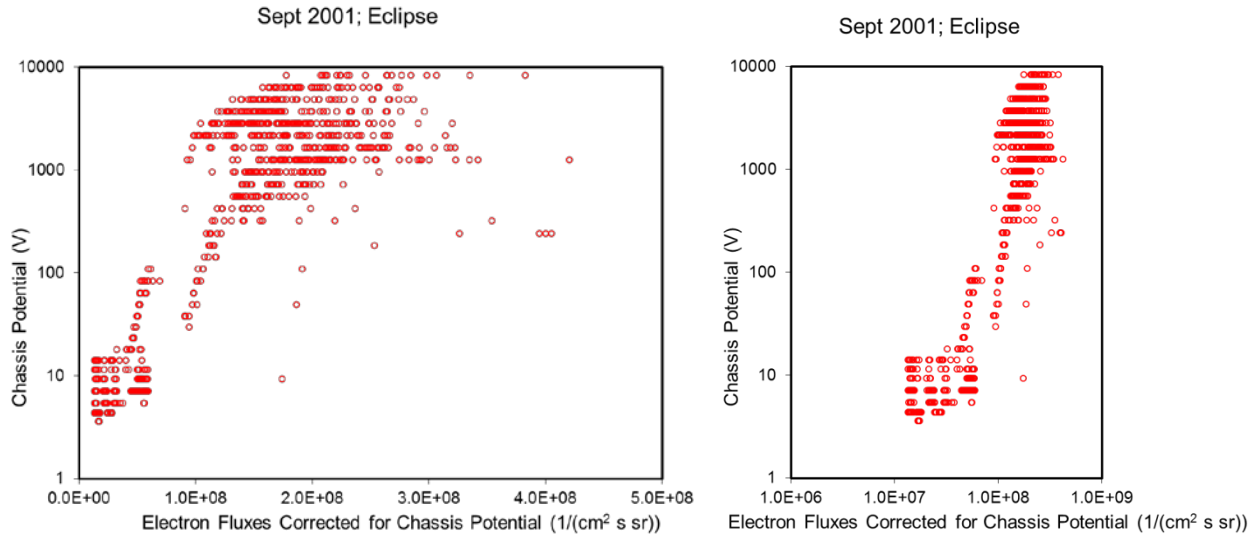


Figure 47. Measured chassis potential versus incident integral electron flux above the barrier energy on linear and logarithmic scales for the eclipse periods.

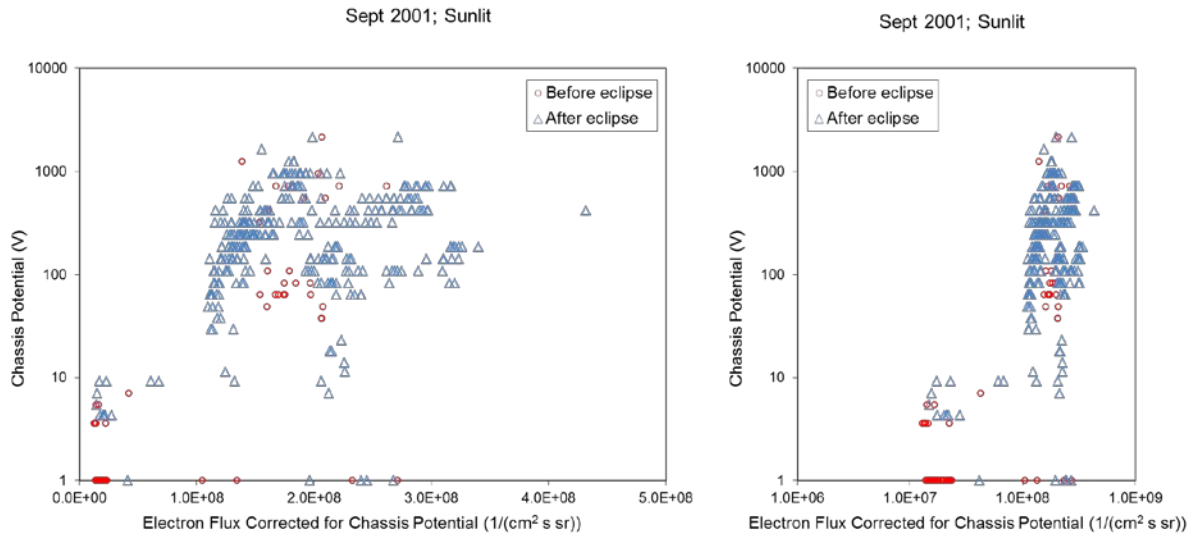


Figure 48. Measured chassis potential versus incident integral electron flux on linear and logarithmic scales when the spacecraft is in sunlight.

The next electron flux measure to consider is integral electron flux above 9 keV. Figure 49 shows a clearer correlation with the chassis potential than does the integral flux over the entire measured energy range. Although, as can be seen in Figure 37, it still provides limited predictive power. The figure also shows that high eclipse potentials are possible at fluxes less than $1 \times 10^7 / (\text{cm}^2 \text{ s sr})$, whereas no conclusions can be drawn about high sunlight potentials due to a lack of data.

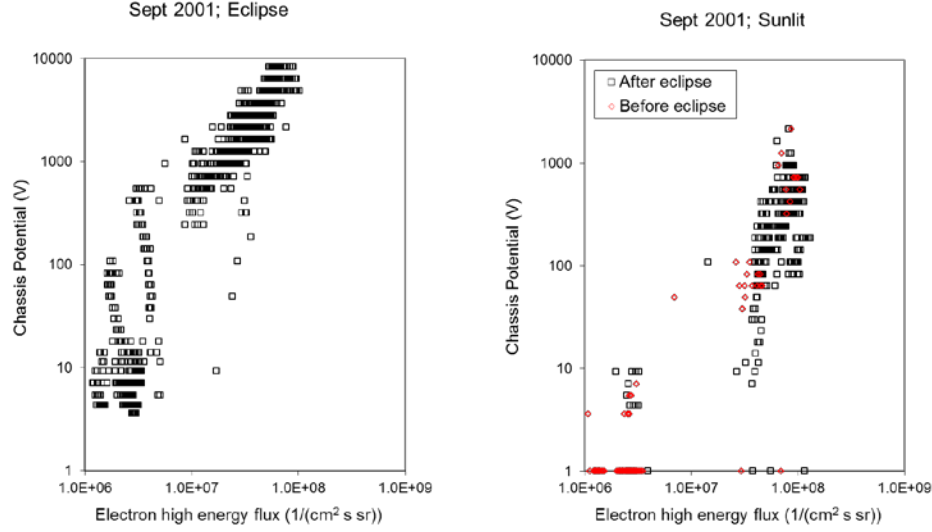


Figure 49. Measured chassis potential versus incident electron flux over 9 keV during the eclipse periods (left) and when the spacecraft is in sunlight (right).

While both the temperature and the flux are correlated with the chassis potential, neither provides good predictions of the chassis potential. Both temperature and flux are measures of the same environment and are correlated with each other, as seen in Figure 50: the high temperature plasmas are those with high fluxes in the higher energy channels.

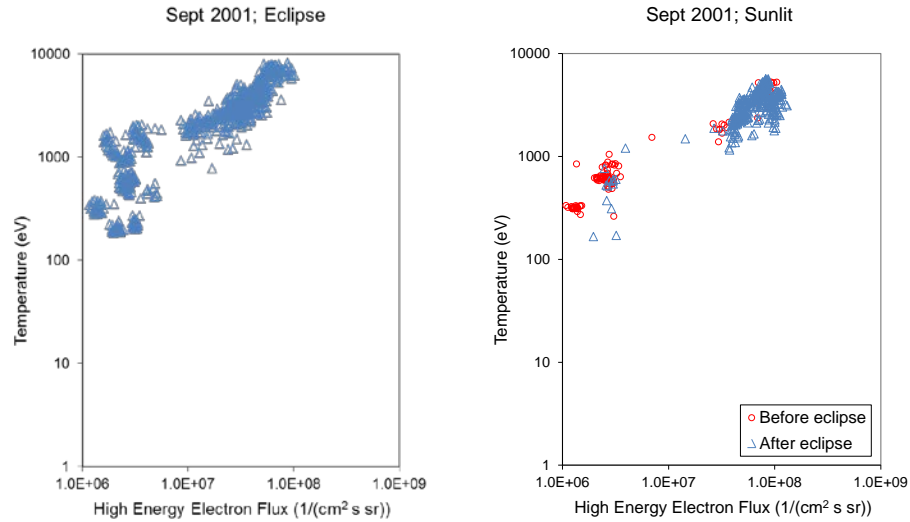


Figure 50. Temperature moment versus high energy electron flux (> 9 keV) during the eclipse periods (left) and when the spacecraft is in sunlight (right).

The final measure of incident electron flux to examine is the differential flux at specific energies. M Thomsen⁷ has observed that there is a minimum value of measured incident electron flux in the 5 to 10 keV energy channels required to produce a chassis potential over about 30 V. The distinct minimum is not seen in higher and lower energy channels. Figure 51 shows the effect. The backwards “C” shape can be understood by considering which electrons reach the detectors. When the spacecraft is at low potentials, electrons of all energies reach the detectors. As long as there is enough low energy plasma or sufficient midrange incident electrons with a secondary yield above 1 to keep the spacecraft from charging, the electron flux at all other energies can be high or low and the spacecraft still does not charge. Thus at low chassis potential the flux has a wide range of values in all energy channels. At high potentials, the electrons are slowed down by the chassis potential, reducing both the flux and the energy. Thus the flux is both reduced in magnitude and appears in a lower energy channel than it would otherwise. Figure 52 shows how the reduction in magnitude affects these graphs. The left graph of Figure 52 shows the potential versus the measured flux to two of the energy channels for the September 2001 dataset. Energy channel 12 of Figure 52 is the same energy channel as that labeled 1.6 keV in Figure 51. On the right, the fluxes are increased to account for the reduction due to the chassis potential. A distinct minimum flux during charging events is still seen, and the left edge of the graphed points is shaped more like an “L” than a “C”.

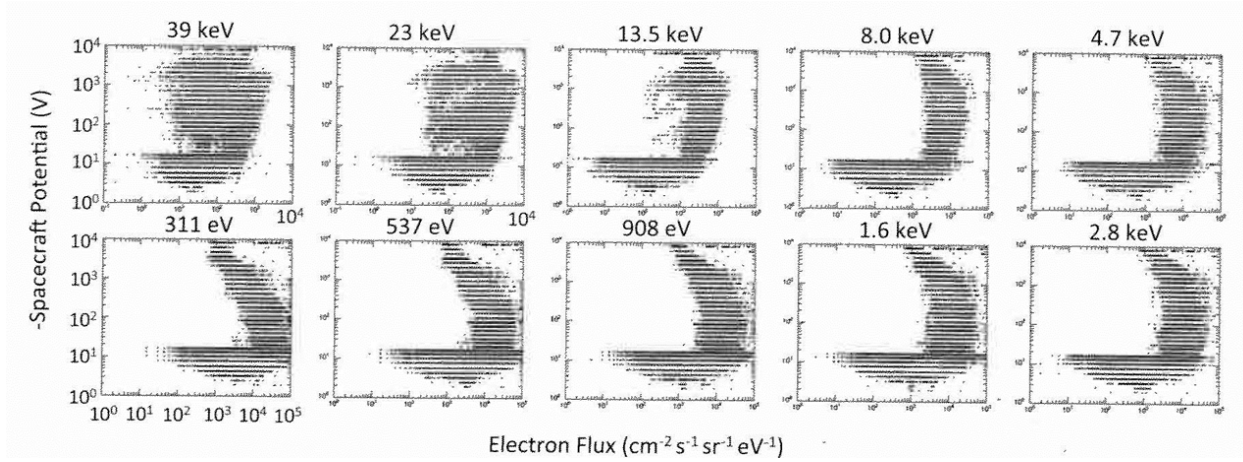


Figure 51. Figure 4 from Reference 3 showing measured chassis potential versus simultaneously observed electron fluxes in different energy channels.

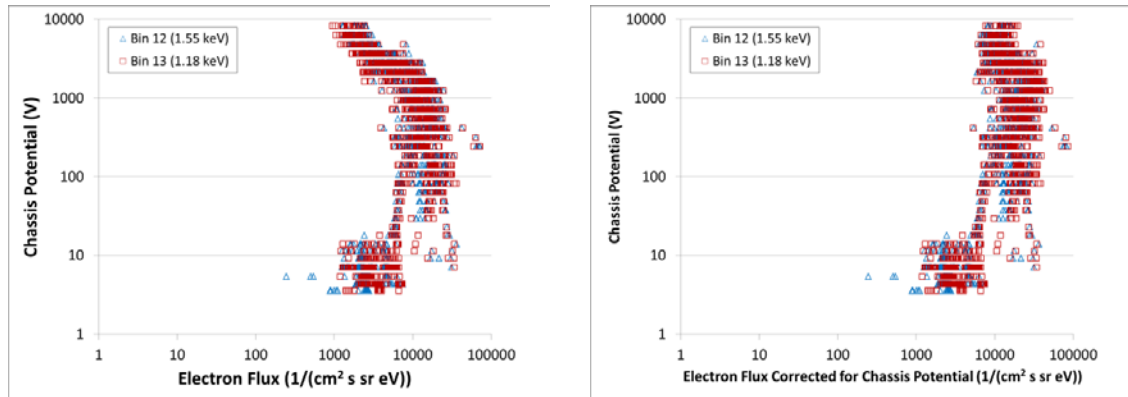


Figure 52. Measured chassis potential versus differential electron flux in two energy channels, without (left) and with (right) the reduction in flux due to the chassis potential.

Results similar to those seen in Figure 52 for the twenty highest energy channels are shown in Figure 53. The highest energy channels show no clear minimum flux for charging events, while energy channels below 8 keV do show a clear minimum. The 10 keV channel, which usually shows a clear minimum, has exceptions during eclipse charging periods on day 252 and day 255, which have high flux in the 8 keV channel but much lower flux in the 10 keV channel. Figure 54 highlights those two events.

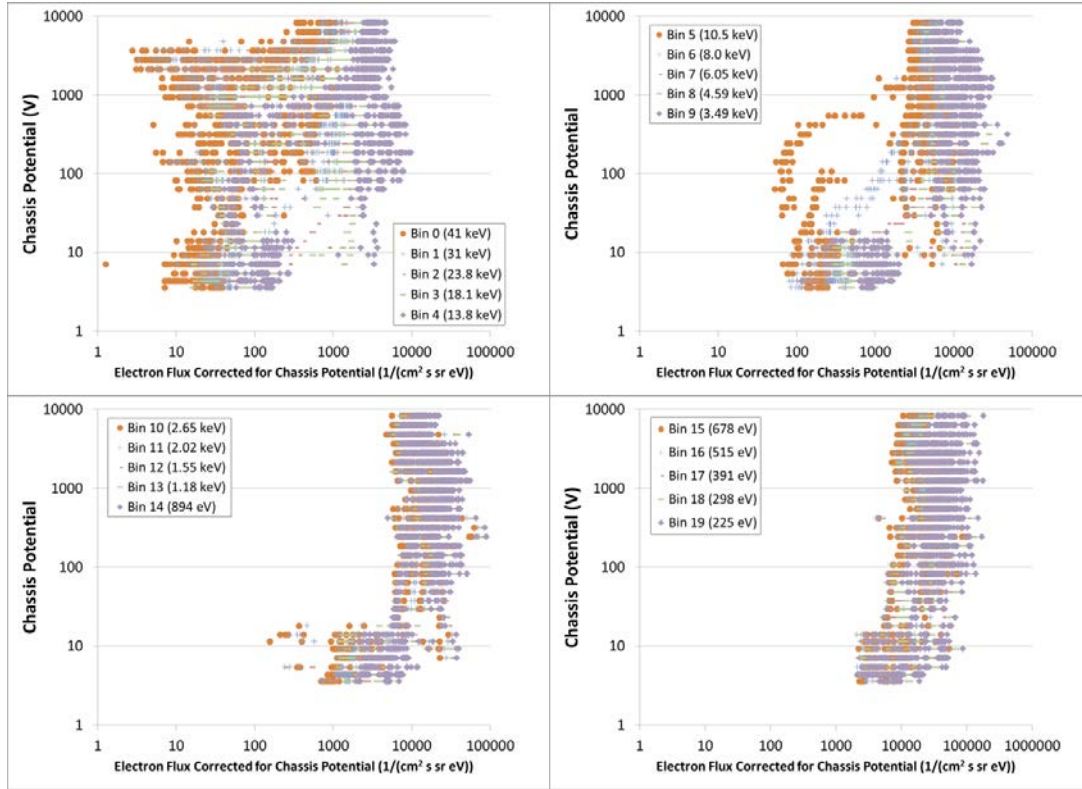


Figure 53. Measured chassis potential versus the differential electron flux in each energy channel, including the reduction in flux due to the chassis potential.

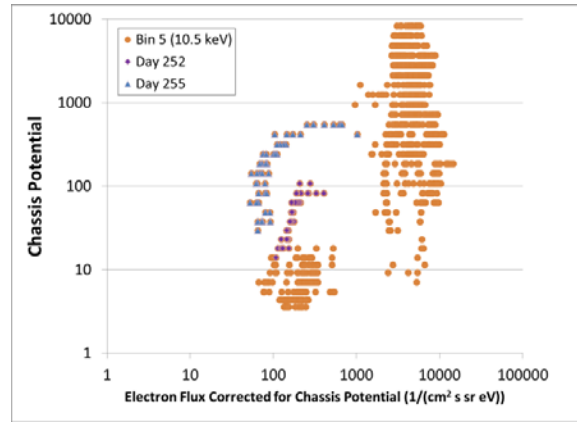


Figure 54. Chassis potential versus differential electron flux to the 10.5 keV energy channel, including the reduction in flux due to the chassis potential. Measurements made during the eclipse periods on days 252 and 255 are identified.

Figure 52 through Figure 54 do not correct for the other chassis potential effect. The measurements at higher chassis potential are of electrons which had much higher energies in the ambient plasma than the 1.6 keV indicated. For example, when the chassis is at 3 kV, electrons with energy near 4.6 keV in the ambient plasma are near 1.6 keV upon reaching the instrument.

The data for a -948 V chassis and for a -317 V chassis are graphed as spectra, flux versus energy in the ambient plasma, in Figure 55 and Figure 56. The different symbols correspond to measurements made at different times. The x-axis value is the energy at the center of the energy channel minus the potential. The sharp rise in flux at the energy that corresponds to the chassis potential (leftmost points of spectra) is due primarily to low energy trapped electrons. The sunlit and eclipse spectra that give rise to the two different charging levels all look similar. Some of the spectra have jumps, which may reflect environmental changes during the sweep.

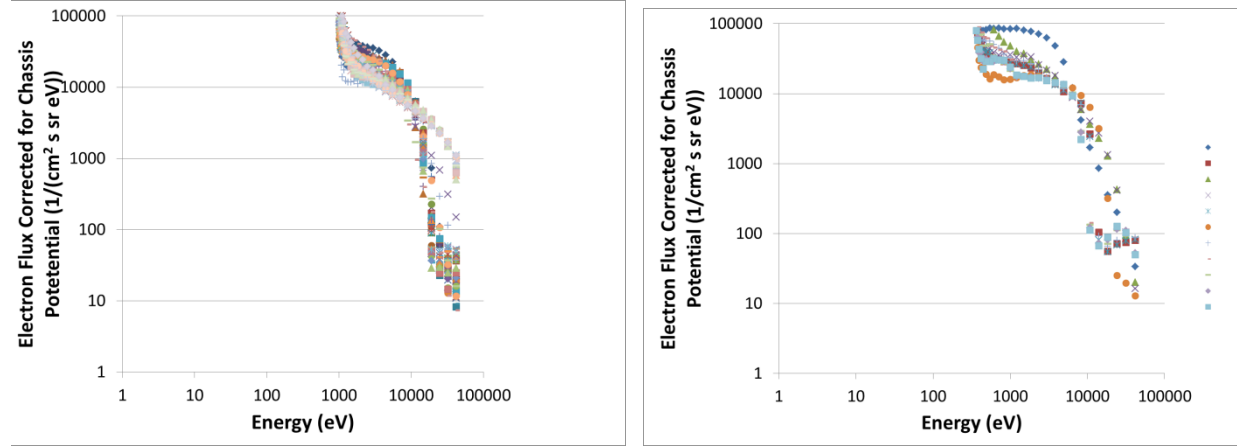


Figure 55. Differential electron flux spectra in the ambient plasma during the eclipse periods when the chassis potential is near -948 V (left) and near -317 (right). The different symbols correspond to measurements made at different times.

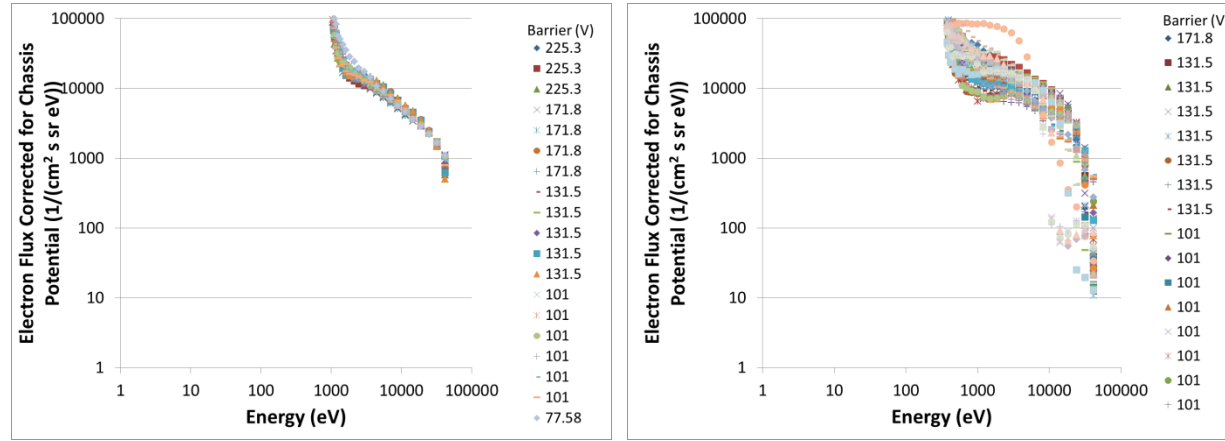


Figure 56. Differential electron flux spectra in the ambient plasma when the spacecraft is in sunlight and the chassis potential is near -948 V (left) and -317 V (right). The different symbols correspond to measurements made at different times and are labeled by the measured barrier heights.

7.5. Estimated Barrier

The estimated barrier, as well as being the lower limit of the electron moment integrals, is a possible measure of differential charging. In this dataset, during the eclipse periods, the estimated barrier is always less than the floor value of 34 V. Figure 57 through Figure 59 show the estimated barrier versus the chassis potential, the electron temperatures, and the electron

fluxes for the sunlit points of the 2001 dataset. There is a correlation with a broad scatter between the barrier estimate and the chassis potential and between the barrier estimate and the two temperature measures. There is a clear minimum flux for the barrier to be over the floor value of 34 V.

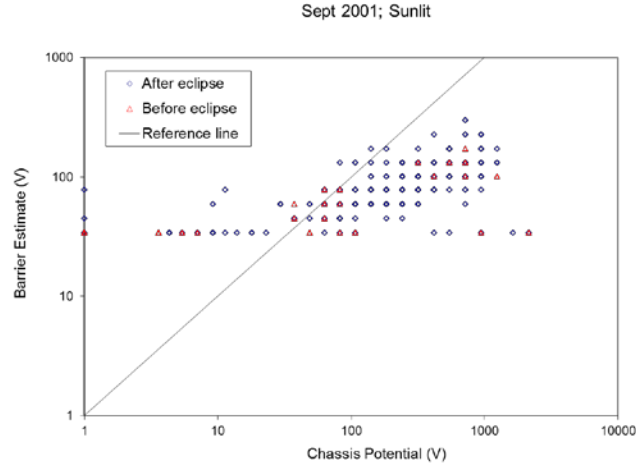


Figure 57. Estimated barrier versus chassis potential when the spacecraft is in sunlight.

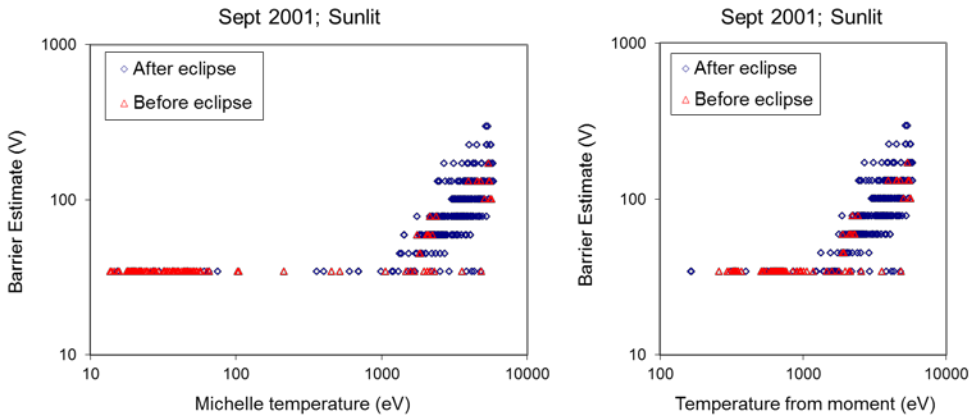


Figure 58. Estimated barrier versus the average temperature (left) and the electron temperature moment (right) when the spacecraft is in sunlight.

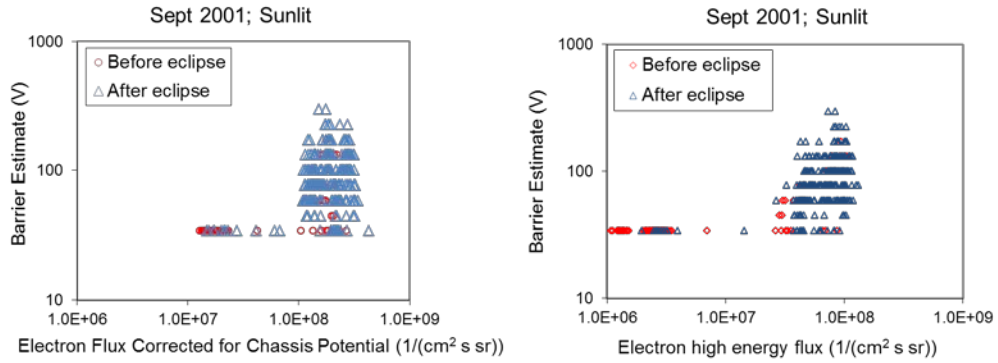


Figure 59. Estimated barrier versus the electron integral flux when the spacecraft is in sunlight. The flux over the maximum of 30 eV and the barrier estimate is shown on the left and the flux over 9 keV is shown on the right.

7.6. Correlations

The figures above show correlations between the temperatures and fluxes and resulting chassis potentials and barrier estimates. These correlations are quantified in Table 1. Correlations were computed for the entire dataset and for the eclipse and sunlit measurements separately. Before the correlations were computed, the measurements were filtered for those with chassis potentials over 10 V and those over 20 V. For the filtered measurements, both the chassis potential and the barrier estimate are most highly correlated with the temperature moment and the average temperature.

Table 7. Pearson product-moment correlation coefficients. Blue values indicate the most nearly predictive correlations.

Parameter 1	Parameter 2	Over 10 V	Over 20 V
All data			
Chassis potential	Temperature moment	0.82	0.82
Chassis potential	Ln of temperature moment	0.66	0.74
Chassis potential	Electron flux over barrier estimate	0.23	0.17
Chassis potential	High energy electron flux	0.19	0.14
Chassis potential	Average temperature	0.82	0.82
Chassis potential	Ln of average temperature	0.49	0.70
Chassis potential	Barrier estimate	-0.32	-0.35
Electron flux over barrier estimate	High energy electron flux	0.57	0.50
High energy flux	Temperature moment	0.60	0.55
High energy flux	Ln of temperature moment	0.62	0.60
Temperature moment	Average temperature	0.99	1.00
Ln of temperature moment	Ln of average temperature	0.90	0.98

Eclipse			
Chassis potential	Temperature moment	0.97	0.97
Chassis potential	Ln of temperature moment	0.82	0.91
Chassis potential	Electron flux over barrier estimate	0.41	0.32
Chassis potential	High energy electron flux	0.85	0.84
Chassis potential	Average temperature	0.96	0.97
Chassis potential	Ln of average temperature	0.62	0.86
Electron flux over barrier estimate	High energy electron flux	0.57	0.48
High energy flux	Temperature moment	0.89	0.88
High energy flux	Ln of temperature moment	0.83	0.88
Temperature moment	Average temperature	1.00	1.00
Ln of temperature moment	Ln of average temperature	0.90	0.98
Sunlit			
Chassis potential	Temperature moment	0.66	0.65
Chassis potential	Ln of temperature moment	0.64	0.64
Chassis potential	Electron flux over barrier estimate	0.14	0.14
Chassis potential	High energy electron flux	0.46	0.45
Chassis potential	Average temperature	0.70	0.69
Chassis potential	Ln of average temperature	0.65	0.66
Chassis potential	Barrier estimate	0.41	0.40
Electron flux over barrier estimate	High energy electron flux	0.66	0.67
Barrier estimate	Temperature moment	0.70	0.69
Barrier estimate	Ln of temperature moment	0.69	0.68
Barrier estimate	Electron flux over barrier estimate	0.03	0.04
Barrier estimate	High energy electron flux	0.41	0.40
Barrier estimate	Average temperature	0.67	0.66
Barrier estimate	Ln of average temperature	0.64	0.64
High energy flux	Temperature moment	0.54	0.53
High energy flux	Ln of temperature moment	0.57	0.56
Temperature moment	Average temperature	0.99	0.99
Ln of temperature moment	Ln of average temperature	0.97	0.99

7.7. Time Dependence

We looked at the time dependence of the flux, temperature, potential, and barrier for several days. Figure 60 is an annotated graph of the time variation of the various quantities for day 271 of 2001. Figure 61 through Figure 69 show the same quantities for different days. The temperature, potential, and estimated barrier are graphed on a logarithmic scale referenced to the left-hand side axis. The integral electron fluxes are on a linear scale and referenced to the right-hand side axis. The diamonds along the bottom indicate when the spacecraft was in sunlight. The chassis potential is only shown when the measurement comes from the identification of a clean ion line. When an ion line is not present, the moments are computed using an inferred potential from Equation 2.

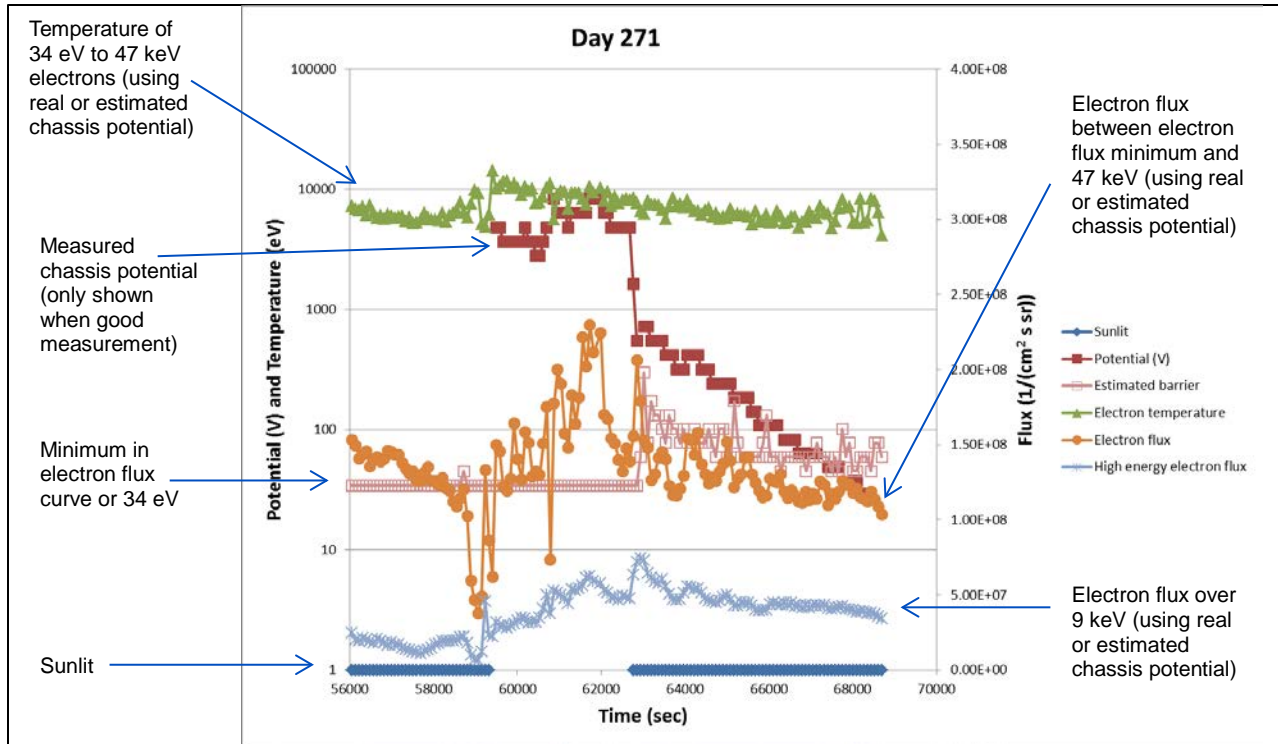


Figure 60. Time dependence of various parameters for day 271 of 2001, including explanatory annotations.

In all of the figures, the integral electron flux over 9 keV (High energy electron flux) has a shape very much like the integral electron flux above the greater of 34 V and the barrier (Electron flux). On day 271, during the eclipse period, the potential increases while the temperature is drifting downward and the flux is rising. In the sunlit, post-eclipse period, it takes about an hour and a half for the chassis to discharge. During this period, the temperature is a bit below 10 keV, at first decreasing slightly and then increasing. The fluxes slightly decrease, with the total flux about $1.2 \times 10^8 / (\text{cm}^2 \text{ s sr})$ and the high-energy flux about $5 \times 10^7 / (\text{cm}^2 \text{ s sr})$. The chassis potential decreases on a shorter timescale than the barrier estimate.

On day 266 (Figure 61), there is a sudden drop in the electron flux while the temperature is approximately constant near 67,000 s. The estimated barrier shows a drop at the same time, and the chassis potential drops for one measurement and is then unavailable.

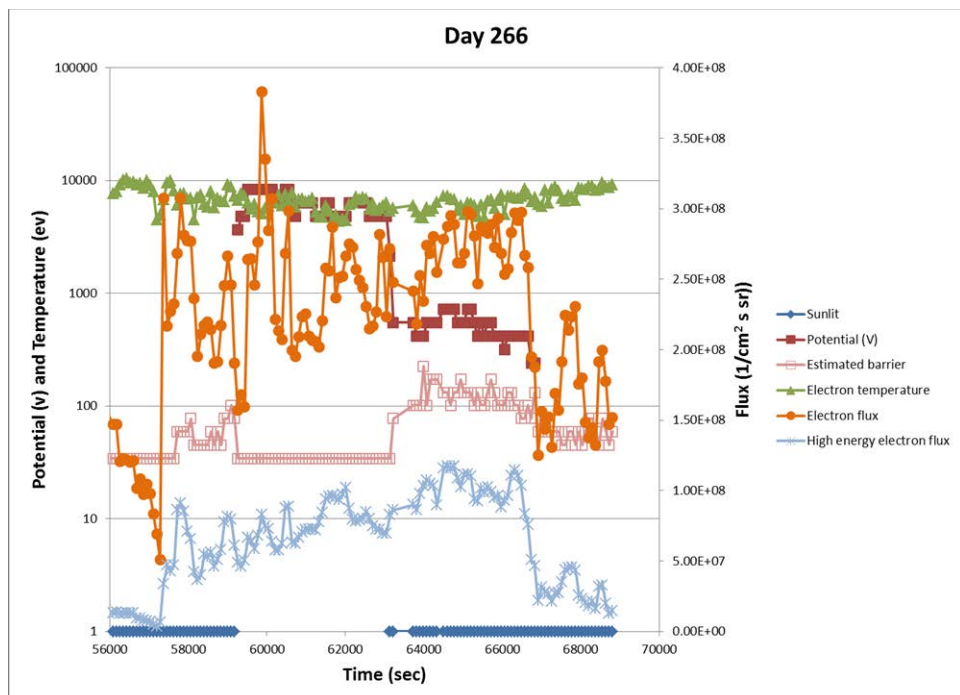


Figure 61. Time dependence of various parameters for day 266 of 2001.

On day 272 (Figure 62) there is an increase in the temperature and flux coincident with eclipse exit. The chassis potential is not available for a period after eclipse exit. When it becomes available again near 64,000 s, the spacecraft is charged. When the flux drops shortly after 64,000 s, the chassis potential and the estimated barrier both drop on the same timescale as the flux changes.

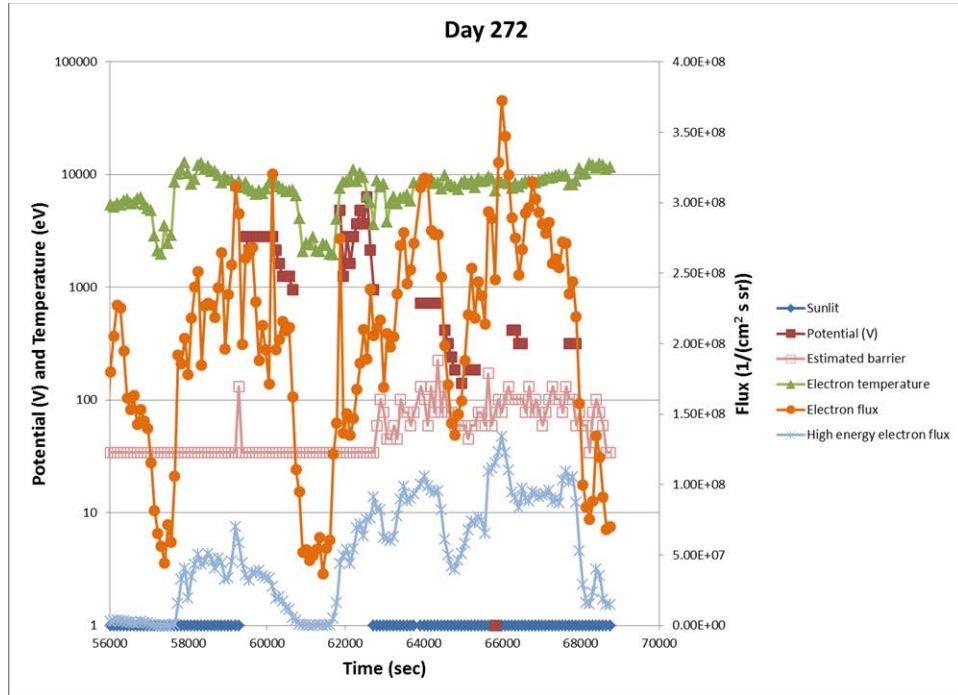


Figure 62. Time dependence of various parameters for day 272 of 2001.

On day 245 (Figure 63) after eclipse exit, the chassis potential and barrier estimate both decrease while the total flux increases, the high-energy flux is constant and the temperature decreases. The reverse trend is seen the next day (Figure 64). At 65500 s, the flux spikes and a barrier forms, while the temperature is close to constant. And the minimum in the flux near 67500 s is reflected in the chassis potential and the barrier estimate.

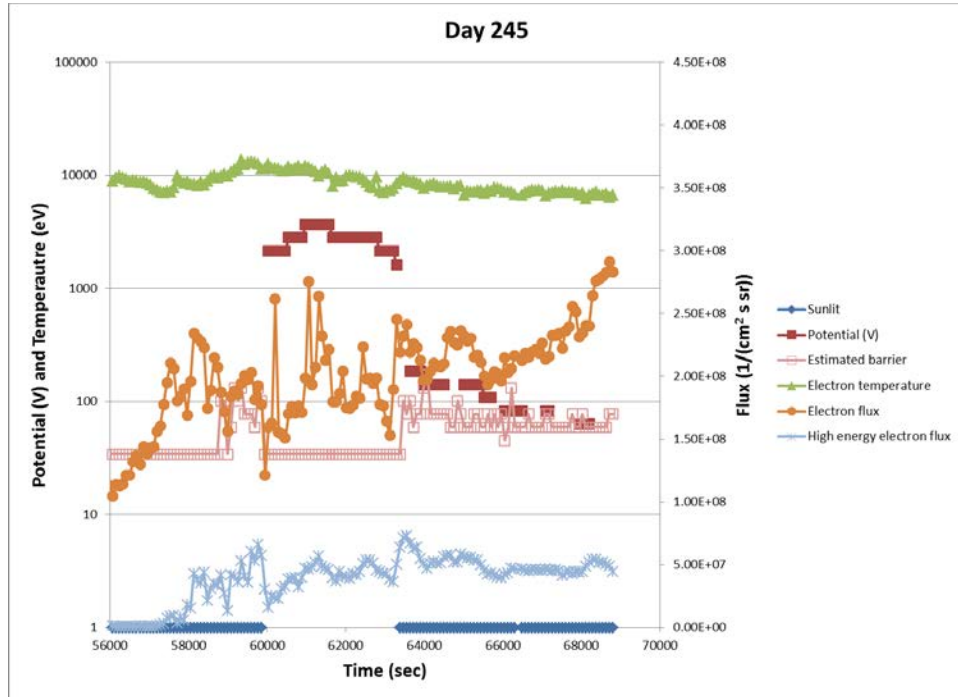


Figure 63. Time dependence of various parameters for day 245 of 2001.

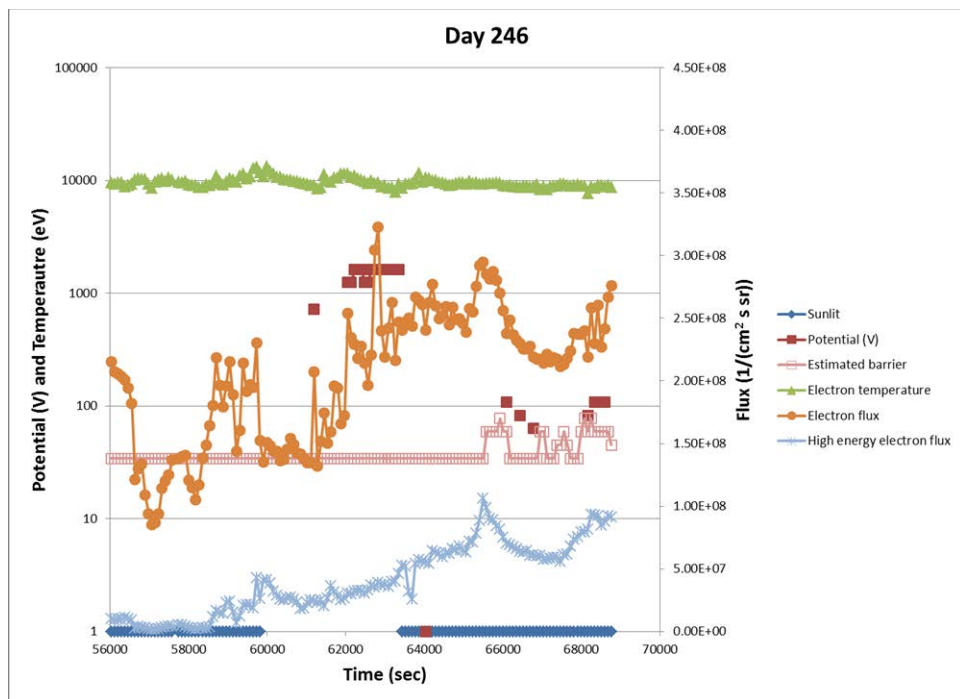


Figure 64. Time dependence of various parameters for day 246 of 2001.

On day 248 (Figure 65) all the tracked quantities trend downward during the post eclipse period. On day 253 (Figure 66) the estimated barrier increases above its floor value of 34 eV while the flux is strongly decreasing and the temperature is very slowly increasing. On day 258 (Figure 67) there is a increase in the estimated barrier coincident with an increase in the high energy flux, while the total flux and temperature are stable at eclipse exit. On day 259 (Figure 68) the chassis potential and maybe the estimated barrier follow the temperature while the high energy electron flux is slightly downward and the total flux is nearly constant. And on day 273 (Figure 69) the chassis potential and the estimated barrier follow the fluxes.

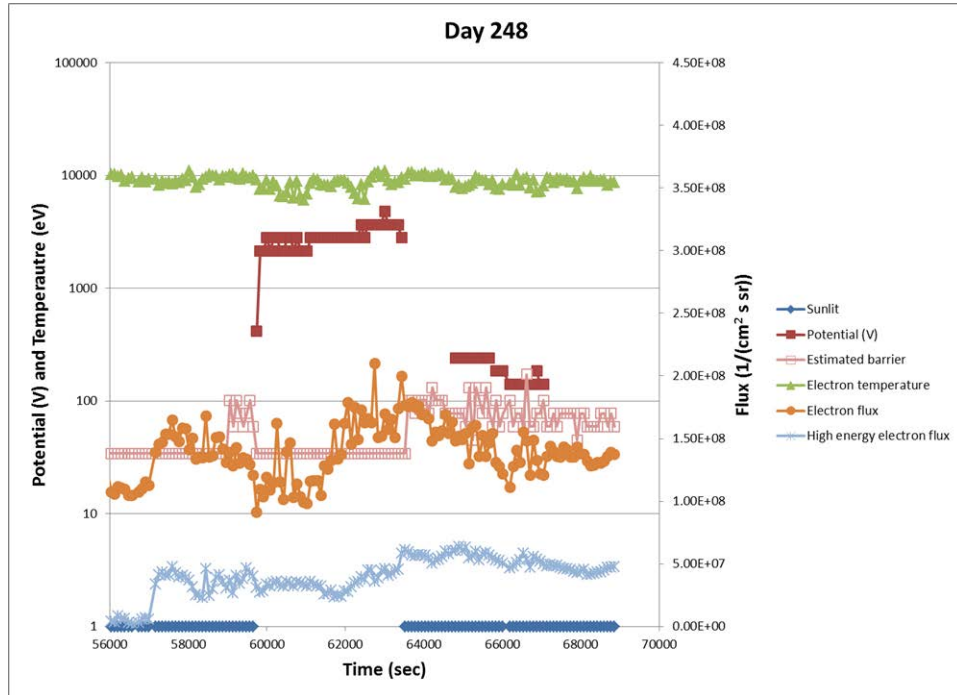


Figure 65. Time dependence of various parameters for day 248 of 2001.

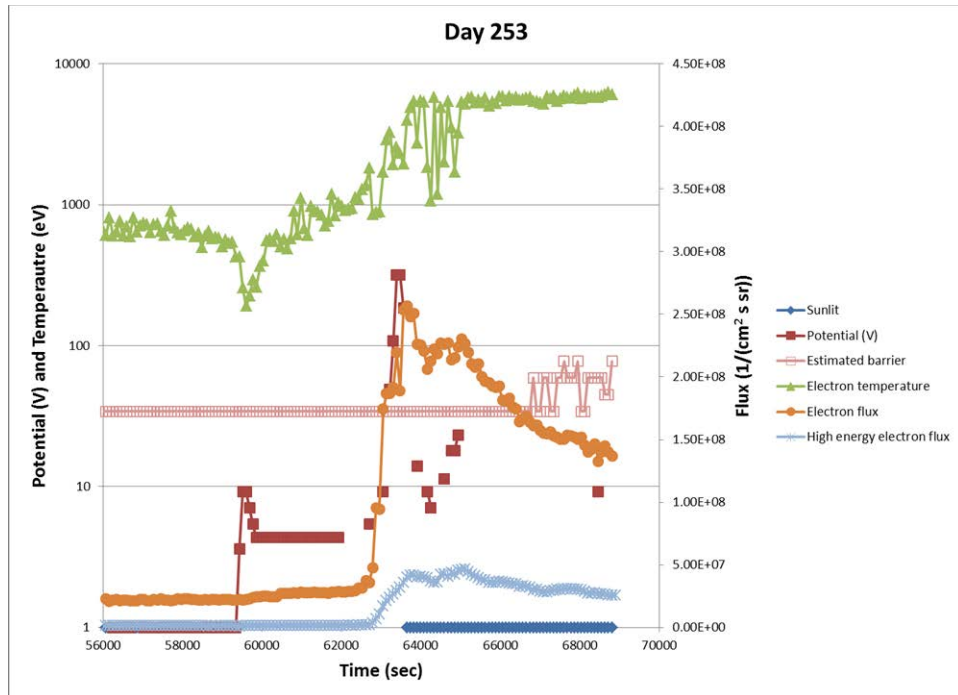


Figure 66. Time dependence of various parameters for day 253 of 2001.

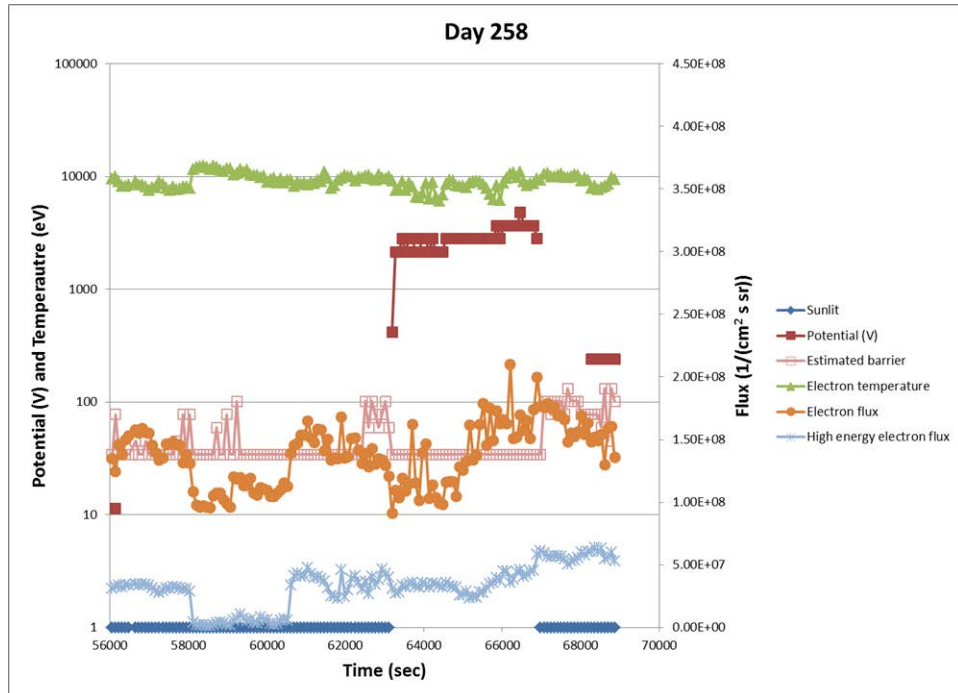


Figure 67. Time dependence of various parameters for day 258 of 2001.

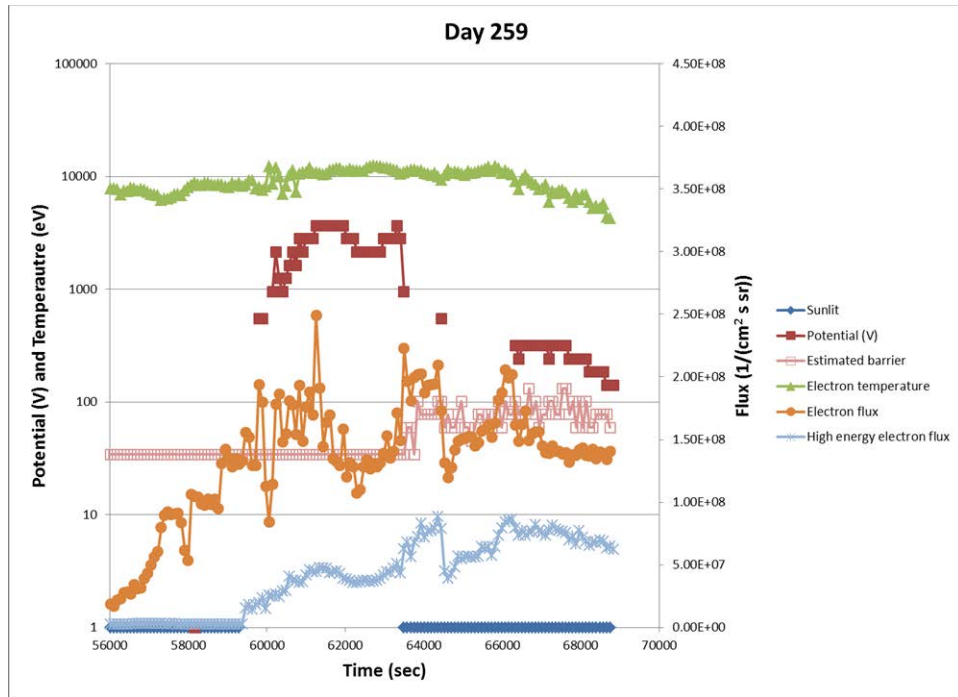


Figure 68. Time dependence of various parameters for day 259 of 2001.

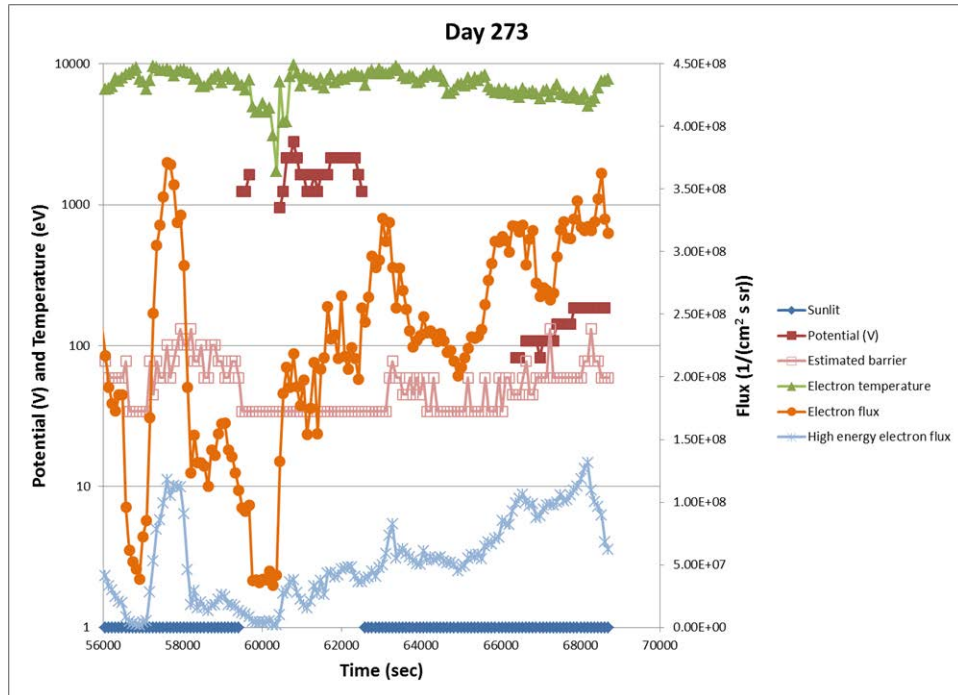


Figure 69. Time dependence of various parameters for day 273 of 2001.

From these figures we can conclude that the timescale of the response of the estimated barrier to the plasma is the same as the timescale of the variation of the plasma. The plasma varies both on the 86 s timescale of the measurements and on the several minute and hour-long timescales.

The electron flux, particularly the high-energy flux, and the temperature are measures of the plasma that correlate with the charging—both chassis potential and estimated barrier. When both measures increase, the charging generally increases. When both measures decrease, the charging generally decays. When one goes up and one goes down, either can occur.

7.8. Conclusions

From this review of the 2002 study and the data used in that study, we can draw several conclusions pertinent to the search for a charging index.

- Both the electron temperature and the electron flux, in particular the high-energy flux, are correlated with the resulting chassis potential and barrier estimate. The average temperature as defined by M. Thomsen provides a very good prediction of the chassis potential in eclipse. (Figure 36)
- Zero-dimensional current balance provides a reasonably good prediction of the chassis potential in eclipse (Figure 35), and does less well in sunlight (Figure 39).
- Chassis potentials in excess of 30 V are only seen if the total flux is over a minimum value. From these data, the minimum value in eclipse is about $3 \times 10^7 \text{ cm}^{-2} \text{ s}^{-2} \text{ sr}^{-1}$ (Figure 47) and no more than $1 \times 10^8 \text{ cm}^{-2} \text{ s}^{-2} \text{ sr}^{-1}$ in sunlight (Figure 48).
- Chassis potentials in excess of 30 V are only seen if the high-energy ($> 9 \text{ keV}$) flux exceeds a minimum value. From these data, the minimum values are about $3 \times 10^6 \text{ cm}^{-2} \text{ s}^{-2} \text{ sr}^{-1}$ in eclipse and no more than $3 \times 10^7 \text{ cm}^{-2} \text{ s}^{-2} \text{ sr}^{-1}$ in sunlight (Figure 49).
- The timescale of the response of the estimated barrier to the plasma is several minutes (Figure 60 through Figure 69).
- Temperature moments, those published by LANL and related ones, do not correspond to the temperature of a Maxwellian fit to the measured spectrum (Figure 43 and Figure 44). Thus there is no justification to their use in *Nascap-2k* as the plasma temperature of a Maxwellian plasma.

References

1. V. A. Davis and M. J. Mandell, *Spacecraft Charging Modeling – Nascap-2k*, Science Applications International Corporation, San Diego, CA, AFRL-RV-PS-TR-2012-0209, 2012.
2. V. A. Davis, M. J. Mandell, D. L. Cooke, A. T. Wheelock, C. J. Roth, *Nascap-2k Self-consistent Simulations of a VLF Plasma Antenna*, IEEE Trans Plasma Science, 40, p. 1239, 2012.
3. R. R. Hofer, D. M. Goebel, J. S. Snyder, I. Sandler, *BPT-4000 Hall Thruster Extended Power Throttling Range Characterization for NASA Science Missions*, IEPC-2009-085, 31st International Electric Propulsion Conference, University of Michigan, Ann Arbor, MI, September 20-24, 2009.
4. V. A. Davis, M. J. Mandell, M. F. Thomsen, *Characterization of Magnetospheric Spacecraft Charging Environments Using the LANL Magnetospheric Plasma Analyzer Data Set*, NASA/CR—2003–212745.
5. V.A. Davis, M. J. Mandell, M. F. Thomsen, *Representation of the Measured Geosynchronous Plasma Environment in Spacecraft Charging Calculations*, J. Geophys. Res., 113, A10204, doi:10.1029/2008JA013116.
6. M. F. Thomsen, E. Noveroske, J. E. Borovsky, D. J. McComas, *Calculation of Moments from Measurements by the Los Alamos Magnetospheric Plasma Analyzer*, LA-13566-MS, 1999.
7. M. F. Thomsen, M. G. Henderson, V. K. Jordanova, *Statistical properties of the surface-charging environment at geosynchronous orbit*, Space Weather, 2013, Reprinted in Space Weather Quarterly, 10, issue 2, 2013.

DISTRIBUTION LIST

DTIC/OCP
8725 John J. Kingman Rd, Suite 0944
Ft Belvoir, VA 22060-6218 1 cy

AFRL/RVIL
Kirtland AFB, NM 87117-5776 2 cys

Official Record Copy AFRL/
RVBXR/Adrian T. Wheelock 1 cy